AN ABSTRACT OF THE THESIS OF

Sean Peter. Kopczynski for the degree of Master of Science in Mechanical Engineering, presented on November 7,1991.

Title: Hydrodynamic Signatures of a 2-D Gas-Solid Fluidized Bed.

Redacted for Privacy

Abstract approved: _____ James R. Welty

Experimental observations of fluidized-bed hydrodynamics were recorded by using two optically-sensing probes in a two-dimensional bed measuring 1.25 by 27 inches. Ambient air was used as the gas while large silica-alumina particles of Geldart classification D were used as the bed solids. The average particle sizes along with their corresponding experimental velocity settings were d_p = 1.85 mm, U_o/u_{mf} = 1.2, 1.4, 1.6; d_p = 2.18 mm, U_o/u_{mf} = 1.4, 1.6, 1.8; and d_p = 2.85, U_o/u_{mf} = 1.2, 1.3, 1.5.

By recording and correlating the pulse-width data from the optical probes at discrete locations across the bed, the effects of superficial velocity, particle size, and presence of immersed surfaces on four bubble properties -- bubble frequency, inter-arrival time, rise velocity, and pierced length -- were used to establish trends or hydrodynamic signatures. The following hydrodynamic signatures were observed:

(1) Bubble frequency is an increasing function of the superficial velocity while inter-arrival time is a decreasing function of the superficial

velocity.

(2) A single characteristic bubble rise velocity and pierced length exist at the probe height used with this two-dimensional fluidized-bed apparatus.

(3) Bubble frequency remains relatively constant with changes in particle size.

(4) The frequency of bubble occurrence drops to near zero at probe locations nearest a single cylinder immersed in a fluidized bed and rises to high values on either side.

(5) As two immersed surfaces are moved farther apart bubble properties for the region between the surfaces approach those recorded with an empty bed.

Hydrodynamic Signatures of a 2-D Gas-Solid Fluidized Bed

by

Sean Peter Kopczynski

A THESIS

submitted to

Oregon State University

in partial fulfillment of
the requirements for the
degree of

Master of Science

Completed November 7, 1991

Commencement June 1992

APPROVED:

Redacted for Privacy

Professor of Mechanical Engineering in charge of major

Redacted for Privacy

Head of Department of Mechanical Engineering

Redacted for Privacy

Dean of Graduate School

Date thesis is presented November 7, 1991

Typed by Sean Kopczynski for Sean Kopczynski

ACKNOWLEDGEMENT

I would like to express my heart-felt appreciation to my major professor, Dr. James R Welty, for providing support, encouragements and guidance over the course of this research.

In addition, I want to thank my partner Lisa N. Freeman for assisting in the construction of and improvements to the experimental apparatus.

Last but not least, I enjoy thanking Dr. Alan George of Montana State University for contributing the optical probes used in this research.

TABLE OF CONTENTS

LIST OF FIGURES

LIST OF TABLES

LIST OF APPENDIX FIGURES

NOMENCLATURE

Symbol	Description	Units
A_d	area of duct	ft^2
A_o	area of orifice	ft^2
b	temporary variable used in flow calculations	--
C	discharge coefficient	--
d_p	particle diameter	mm,μm
D	internal surface diameter	inch
D_d	diameter of duct	feet,inch
D_o	diameter of orifice	feet,inch
E	velocity of approach	--
f_b	bubble frequency	bubbles/s
g	acceleration due to gravity	ft/s^2
g_c	English unit conversion constant	$lbm\text{-}ft/lbf\text{-}s^2$
k	ratio of specific heats	--
K	flow coefficient	--
K_o	intermediate flow coefficient variable	--
l_b	bubble pierced length	inch
L	distance between centers of internal surfaces	inch
L_f	expanded bed height	inch
L_m	packed bed height	inch
L_{mf}	bed height minimum fluidization	inch
N_b	number of bubbles	--
$Q_{m\,actual}$	actual mass flow rate	lbm/s
$Q_{m\,ideal}$	ideal mass flow rate	lbm/s
P_{atmos}	absolute pressure of atmospheric air	lbm/ft^2
P_1	absolute pressure of upstream air	lbm/ft^2
P_2	absolute pressure of downstream air	lbm/ft^2
R	ideal gas constant	ft-lbf/lbm-R
Re_{Do}	Reynolds number based on D_o	--

Re_p	Reynolds number based on d_p	--
T	ambient air temperature	°F
U_b	bubble rise velocity	ft/s
u_{mf}	minimum fluidization velocity	ft/s
U_o	superficial gas velocity	ft/s
V_{cutoff}	level discriminator cutoff voltage	volts
V(t)	optical probe output voltage	volts
V'(t)	level discriminator output voltage	volts
w_i	discrete uncertainty	--
W_f	overall uncertainty	--
Y	expansion factor	--

Greek Symbols

β	diameter ratio	--
ΔL	distance between probes	inch
ΔP	pressure drop	in H2O
Δt	time shift between probe signals	second
$\Delta\tau_b$	pulse width of bubble	second
ε_{mf}	bed voidage	--
μ_{atmos} , μ	dynamic viscosity of ambient air	lbm/ft-s
ρ_{atmos}	density of atmospheric air	lbm/ft^3
ρ_{up}	density of upstream air	lbm/ft^3
$(\tau_b)_i$	time of bubble i	second
τ_{ia}	inter-arrival time	second
τ_{sp}	sampling period	second

1. INTRODUCTION

The current and projected availability of petroleum in the world has forced many countries to seek alternative energy sources. In the United States one of the most attractive and abundant energy supplies is coal. However, environmental and political concerns have prevented the wide usage of this energy source.

Environmental concerns arise from several factors. First, during the combustion of coal, SO_x (SO_2, SO_3) and NO_x (NO_2,NO_3) compounds are formed. These compounds are the main source of the air pollution and acid rain caused by coal burning power plants. Second, mining or extraction of coal causes environmental degradation. Third, since coal does not burn completely large amounts of solid waste in the form of ash are left behind. Finally, if scrubbers are used to help reduce emissions, the coal produces a sludge waste that makes disposal difficult [12].

The majority of the political concerns emanate from power plant locations. Coal is largely used as a source of energy in the northern latitudes of the United States since that is where it is found in abundant quantities. Consequently, due to weather patterns and power plant locations some of the pollutants from these plants drift northward into our neighboring country of Canada causing unwanted pollution and environmental damage.

Application of the fluidized bed to the coal-fired power plant industry will

help in overcoming these concerns as described below.

Firstly, due to the dynamic behavior of fluidized beds the heat transfer rates between the hot bed and immersed surfaces, such as pipes carrying the water-steam working fluid of a power plant, allow the desired energy transfer to occur at lower-than-normal temperatures. At a lower operating temperature, less NO_x is formed from the burning coal. [4] An additional benefit of lower boiler operating temperature is that the coal ash does not melt and cause corrosion problems [12].

Secondly, limestone or dolomite has the ability to adsorb SO_x compounds. The sulfur in the coal combines chemically with the calcium in the particles to form a calcium sulfate. Thus, if limestone or dolomite is used as the bed particle, SO_x emissions can be reduced to more acceptable levels by the sulfur compounds reacting with the limestone to form dry solid wastes [12].

Finally, with the increase of heat transfer rates between hot bed and internal surfaces, the size of the required combustion chamber can be reduced saving valuable space and materials [12].

Conversely, the presence of a fluidized bed produces new problems such as production of solid wastes and erosion of internal surfaces and combustion chamber walls. Clearly, the environmental and efficiency benefits outweigh these disadvantages [8].

However, before fluidized beds can be successfully applied to industry, their nature must be more clearly defined. That is, the heat and mass transfer effects need to be predicted with better accuracy to insure proper design and maximum performance of combustors.

Understanding the hydrodynamic characteristics (general bubble or gas void behavior) of a cold gas-solid fluidized bed will provide insight into the nature of fluidized beds. The characterization of fluidized bed hydrodynamic behavior is the first step in understanding and prediction of convective heat transfer performance.

The research described in this thesis was accomplished using an optical probe for recording or observing bubbles at discrete locations in a cold two-dimensional gas-solid fluidized bed to attain a general view of bubble behavior under a variety of conditions.

1.1 Fundamentals of Fluidization

The term *fluidization* refers to the act of giving fluidlike properties or characteristics to solid particles through their interaction with a moving gas.

1.1.1 General Description of a Gas-Solid Fluidized Bed

A gas-solid fluidized bed is composed of a chamber or container, normally cylindrical in shape, that is partially filled with solid particles. The solid particles or bed of particles rest on a distributor plate located at the bottom of the chamber. A gas, pumped under pressure, is introduced to the particle bed at the distributor plate. The distributor plate forces a pressure drop in the flowing gas so that the gas may be uniformly supplied to the particle bed. The bed normally has some type of immersed surfaces. For example, in a coal-fired power plant the immersed surfaces would be tubes carrying water-steam working fluid as seen Figure 1-1. A schematic representation of a gas-solid fluidized bed is shown in Figure 1-2.

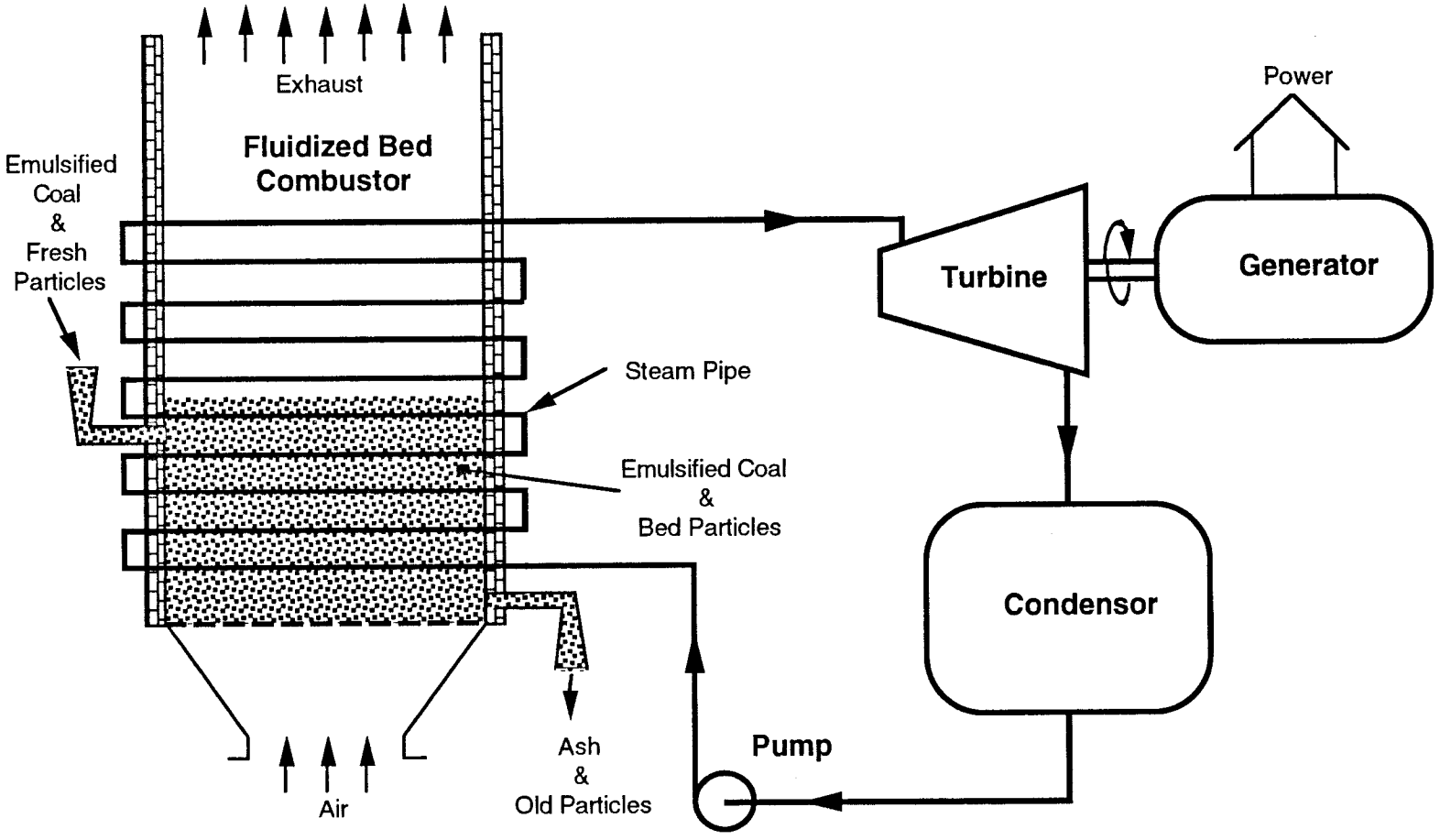

Figure 1-1: Schematic Illustration of a Coal Fired Power Plant with Fluidized Bed.

1.1.2 Fluidized Beds Flow Regimes

A flow regime refers to a bed condition that is distinguishable over a range of flow rates. Hence, when a gas is introduced to a bed of particles different distinguishable conditions will occur depending on the rate of flow. These conditions can be best illustrated by examining the pressure drop across a bed of particles as a function of the fluid flow rate (see Figure 1-3). For an experimental plot of the pressure drop across the particle bed used in this research as a function of the fluid flow rate see Appendix B.

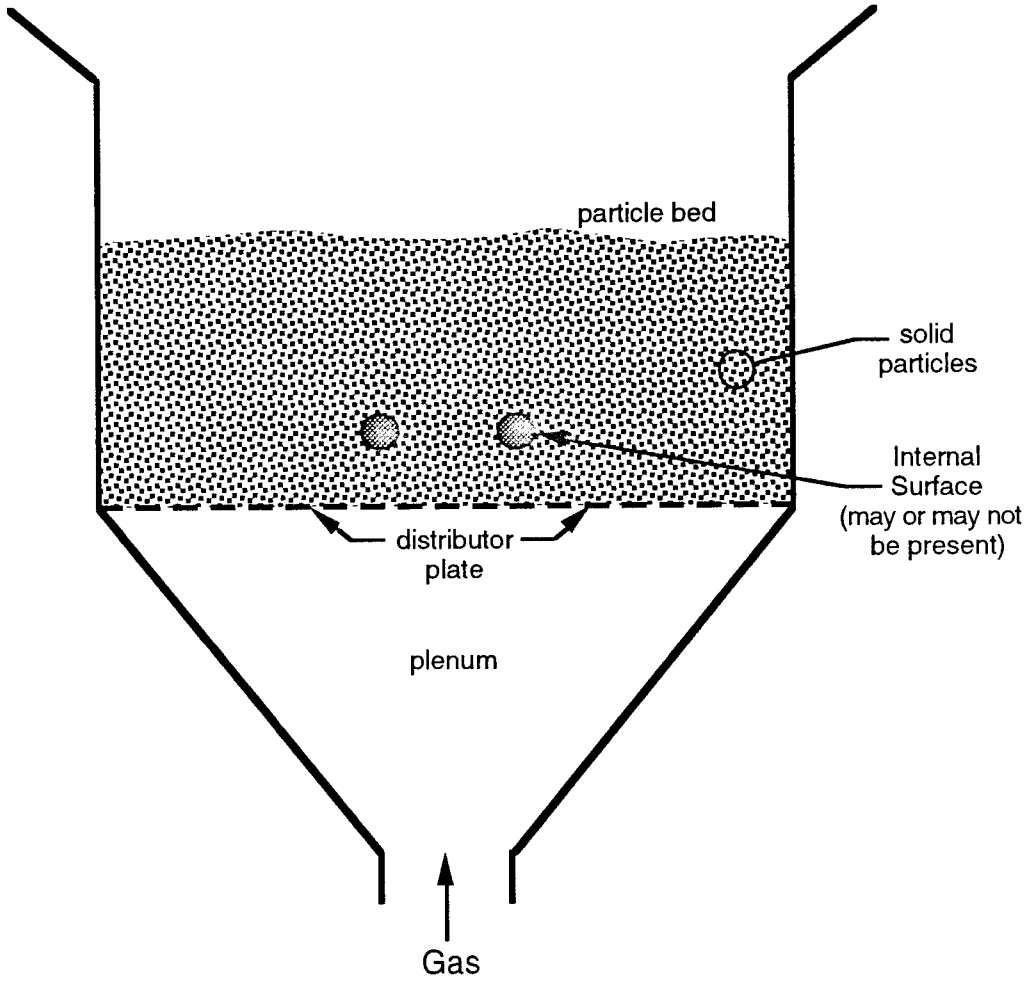

Figure 1-2: Schematic Representation of a Gas-Solid Fluidized Bed.

At low flow rates the bed acts as a porous medium. That is, the particles remain locked in place, forcing the gas to flow around them, and the pressure drop across the bed of particles increases linearly with the fluid flow rate. This bed condition is referred to as a *fixed bed* or *packed bed.*

If the fluid flow rate is steadily increased to the point where the pressure drop across the particle bed approaches its weight, two notable changes occur. First, the particles unlock and become suspended in the flowing gas. At this point the particles are said to be fluidized. Second, the top of the bed levels out with the horizontal. At this fluid flow rate the bed is said to be in a condition of *incipient fluidization* or *minimum fluidization.*

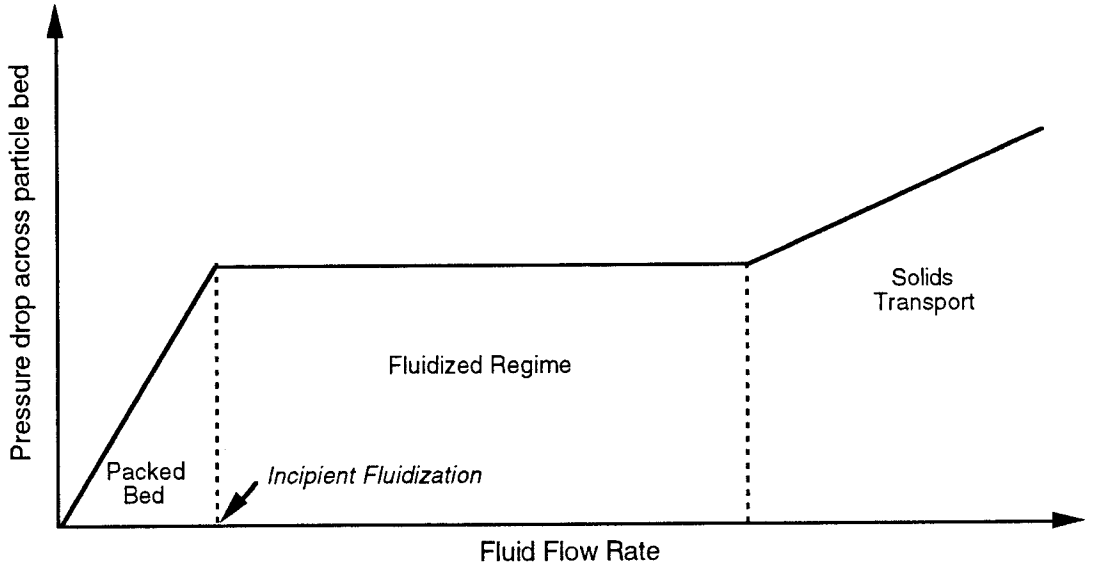

Figure 1-3: Pressure Drop Across Bed as a Function of the Fluid Flow Rate.

When the fluid flow rate is at or increased beyond the point of minimum fluidization the force exerted on the particles by the gas remains constant since the solids are "unlocked" and free to move in the rising gas. Thus, the

pressure drop across the bed remains relatively unchanged with escalating fluid flow rates. On the other hand, as shown in Figure 1-4, the height of the bed does increase gradually with the flow rate or superficial velocity.

When the flow rate surpasses the point of minimum fluidization the particle bed can no longer sustain gas flow around and in between particles. Therefore, the excess flow is passed through the bed in the form of gas voids or "bubbles." The term bubbles emanates from the similarity that the gas voids share with that of a boiling liquid. At this set of flow rates the bed is referred to as a *bubbling fluidized bed* or *boiling bed.* The corresponding flow regime is called the *bubbling regime.* However, for some particle beds bubbling does not immediately follow minimum fluidization. A fluidized bed is in the *quiescent state* if the flow rate is above incipient fluidization and below the onset of bubbling.

As the flow rate is increased even further, the size of the bubbles begin to approach the size of the chamber. These very large bubbles are called

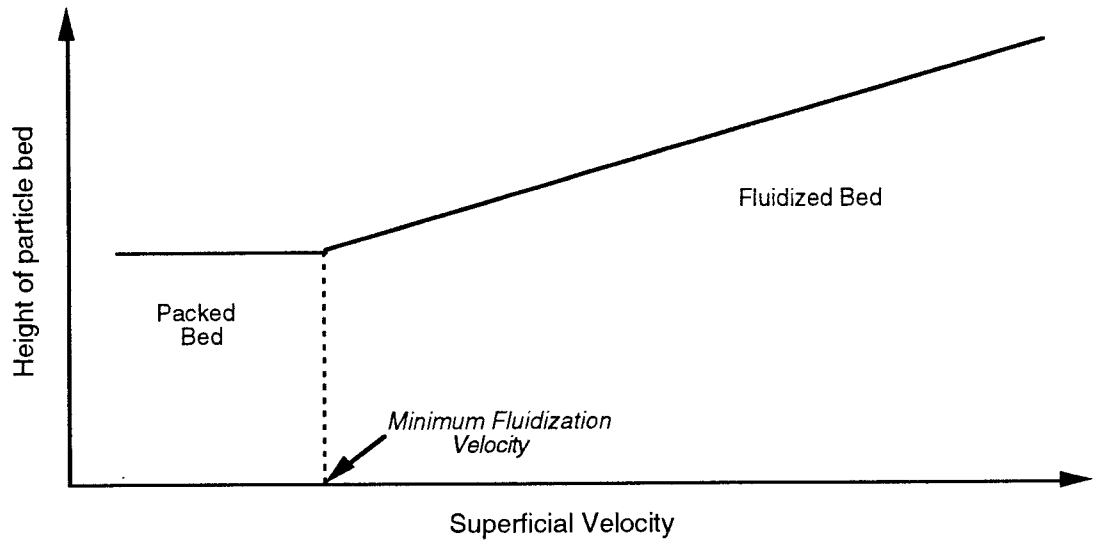

Figure 1-4: Variation of Bed Height with Superficial Velocity.

"slugs", and a bed passing slugs is designated as a *slugging fluidized bed.*

If the fluid flow rate supplied to the fluidized bed exceeds the terminal velocity of the particles, these solids will begin to be carried out of the chamber with the gas. This bed condition is referred to as *solids transport* or *pneumatic transport.* The corresponding flow regime is termed *fast fluidization.*

The various forms of fluidization just discussed are illustrated in Figure 1-5.

1.1.3 Liquidlike Behavior of Fluidized Beds

A particle bed begins to behave much like a fluid at the point of incipient fluidization. At this point the gas-solid combination appear to take on properties similar to that of a normal fluid. The observed liquidlike properties or characteristics can be described as follows: [10]

a) the particle bed takes on the shape of its container;

b) large, light objects float on the surface;

c) the surface of the fluidized bed remains level with the horizontal;

d) particles will flood or pour forth from openings in the container;

e) if two beds of different levels are connected, the two bed heights will equalize;

f) the pressure difference between any two points in a bed is approximately equal to the static head between the points; and

g) a bubbling bed resembles a boiling liquid.

Some of the characteristics described above are illustrated in Figure 1-6.

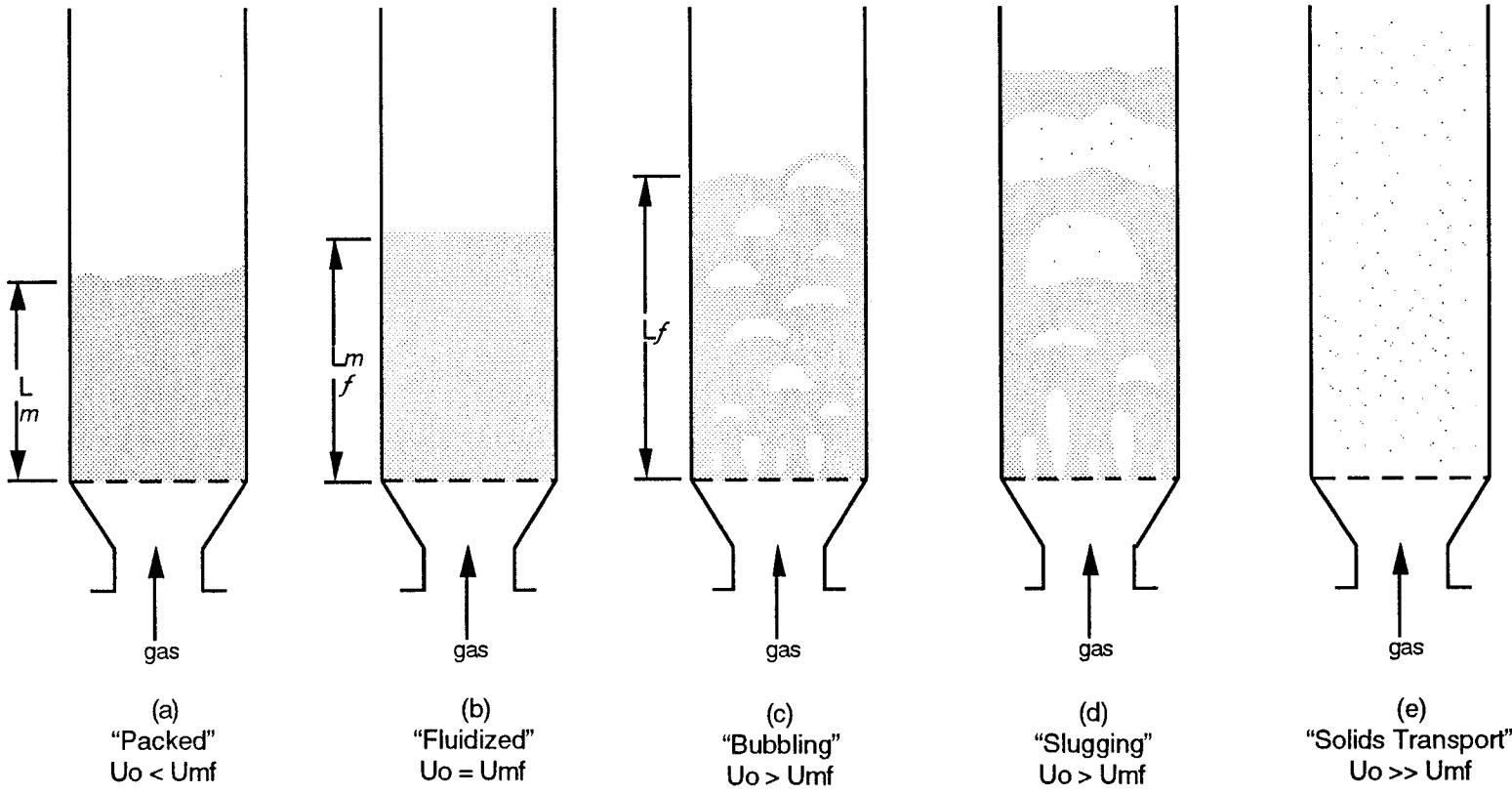

Figure 1-5: Various Stages of Fluidization. Adapted from Kunii and Levenspiel [10].

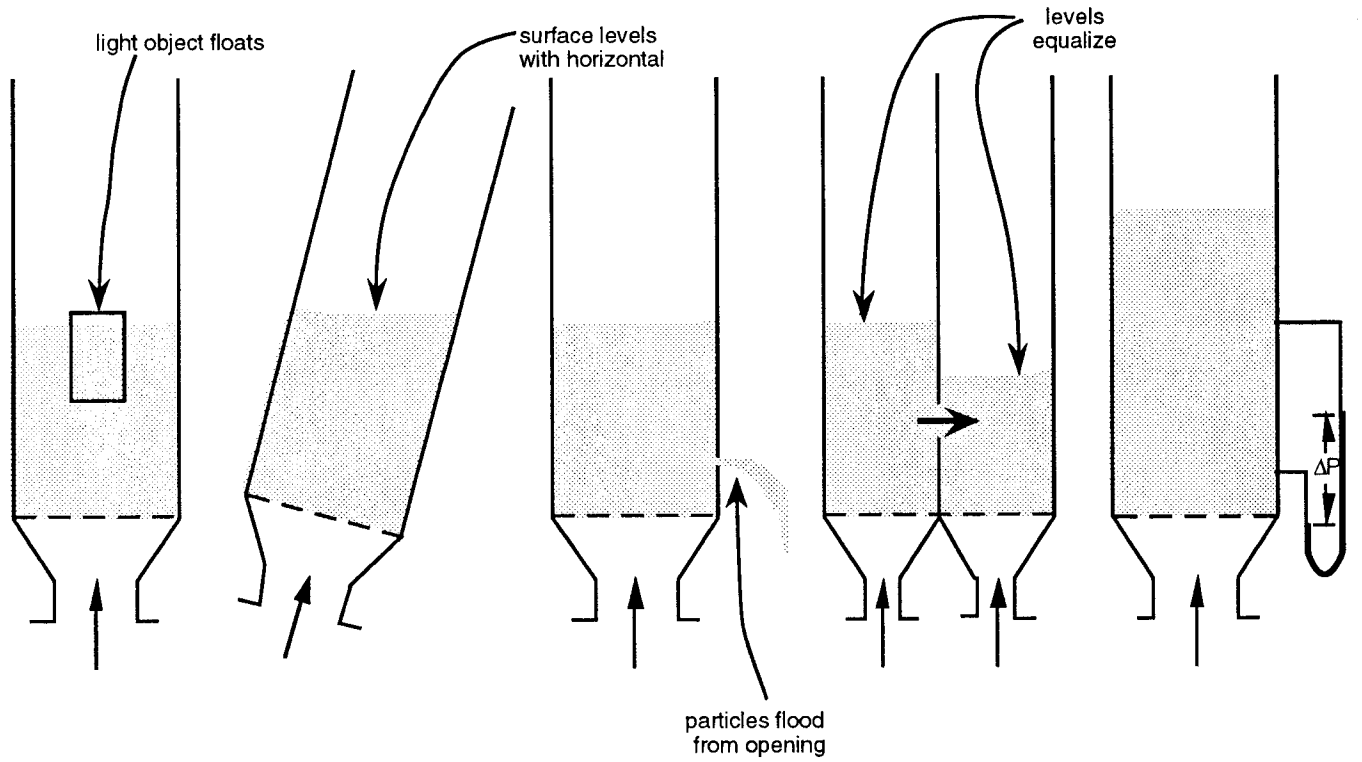

Figure 1-6: Liquidlike Behavior of Gas-Solid Fluidized Beds. Adapted from Kunii and Levenspiel [10].

1.1.4 Quality of Fluidization

The overall goal of fluidized beds used as combustion zones in power plants is to enhance the heat transfer while decreasing NO_x and SO_x concentrations in the exhaust gas. Enhanced heat transfer is accomplished by the fluidized bed's ability to provide overall temperature uniformity, good particle mixing and good particle contacting with immersed surfaces. However, when a fluidized bed is in the bubbling regime, the quality of fluidization can be very dependent on the system fluidizing the bed. Theoretically, bubbles will randomly form across the bed. Once a bubble is formed at one location another bubble will form elsewhere. This type of bubbling action provides a high-quality fluidization due to the uniformity of the bubble distribution. Unfortunately, some adverse bubbling flow patterns can occur due to system inadequacies such as poor distributor design or incorrect pump sizing.

A common adverse flow pattern is *channelling*. This type of bubbling pattern is characterized by an area or areas in the particle bed where the bubbles have an abnormally high frequency of occurrence. That is, the fluidizing gas follows one or two particular paths through the bed. Since most of the gas supplied to the fluidized bed is rising through the bed at the areas of channelling, the remainder of the bed experiences few bubbles, if any. A channel also creates entrainment of solid particles known as circulation cells. A circulation cell causes particles to move in circular patterns within the bed.

A channelling fluidized bed is depicted schematically in Figure 1-7.

1.2 Gas-Solid Motion in Fluidized Beds

Gas-solid motion in fluidized beds involves the interaction of the gas and solid phases, for instance, how bubbles form, rise, coalesce or break-up.

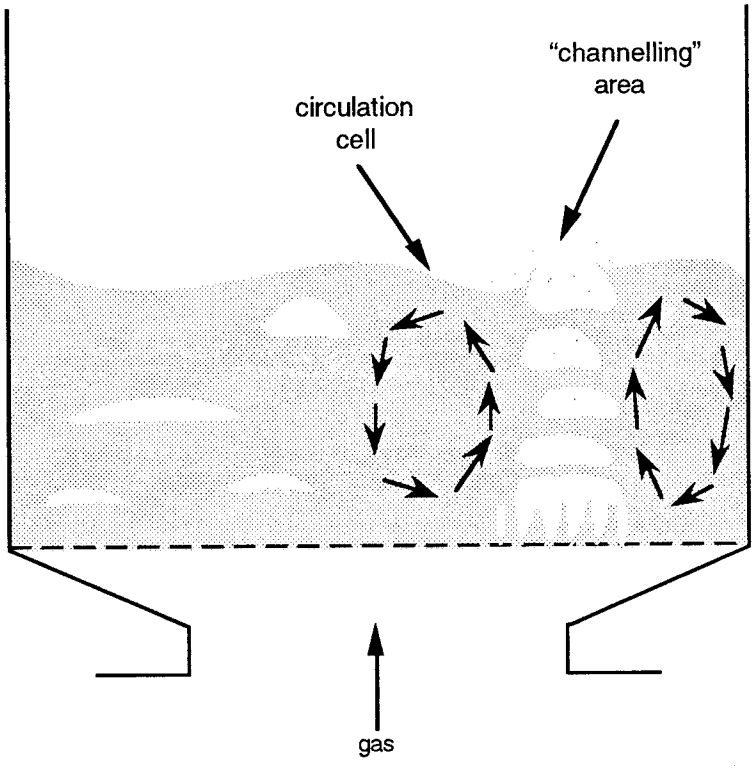

Figure 1-7: Illustration of a Channelling Fluidized Bed.

1.2.1 Bubble Formation

Bubble formation occurs just above the distributor plate for flow rates in the bubbling regime as described by the following sequence. First, a jet of gas begins to form at an opening in the multi-orifice distributor plate since the aerodynamic drag force of the gas on the particles exceeds the particles' weight. Consequently, the jet of gas forces the particles aside. Second, the

spout will continue to grow in size until the gas velocity at the boundary approaches the minimum fluidization velocity [3]. Third, the aerodynamic drag force will equalize with the particle weight, and the jet will close up forming a bubble. Finally, after the bubble is formed, it will rise through the bed due to the force of buoyancy.

These stages of bubble formation at a distributor orifice are portrayed in Figure 1-8.

1.2.2 Rising Bubbles

Three factors concerning rising bubbles (shape, size and coalescence, and particle motion around) were considered in the following paragraphs.

The shape of the rising bubble is acknowledged throughout the literature as being spherical with an indented base (i.e. spherical bubble cap). The spherical cap shape was observed by Rowe [15] using X-ray photography. Davidson and Harrison [5] also observed a spherical bubble cap when they photographed bubbles erupting from the surface of a fluidized bed. Furthermore, since a fluidized bed behaves similarly to a liquid, as discussed earlier, a comparison would indicate a spherical shape. In other words, gas bubbles rising through a fluidized bed would be similar to gas bubbles rising in a liquid, and bubbles rising in liquids are spherical in shape due to hydrostatic pressure. The spherical bubble cap shape is illustrated in Figure 1-9.

According to Yasui and Johanson [17] gas bubbles increase in size with gas velocity, height in bed, and particle size. The reasons for increased

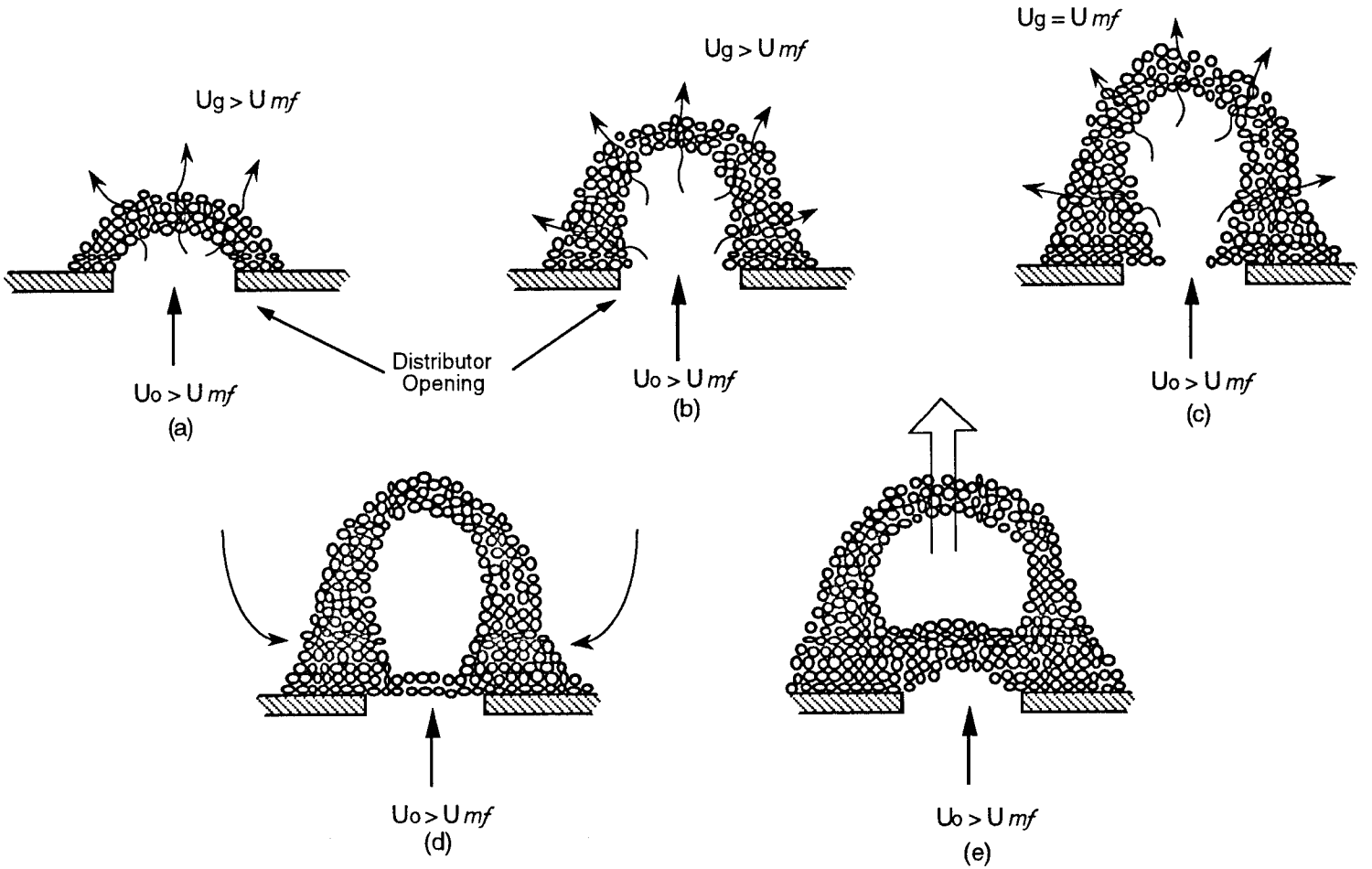

Figure 1-8: Various Degrees of Bubble Formation at the Distributor Plate
Adapted from Cheremisinoff [3].

bubble size due to position within the bed are not readily apparent, and there are at least three explanations for this size increase [5]:

a) the effective hydrostatic pressures acting on the bubbles decreases as they rise;

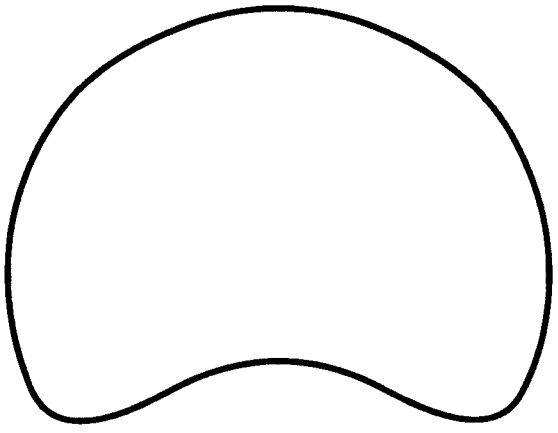

Figure 1-9: General Bubble Shape -- Spherical Cap with Indented Base.

b) bubbles may catch up with one another and coalesce or combine; and

c) neighboring bubbles in a common horizontal plane may merge when they are close to each other.

A drawing of one possible type of bubble coalescence is shown in Figure 1-10.

Particles move laterally around the upper bubble surface as it rises through a fluidized bed instead of compressing the surface [5]. The particles tend to move out of the way of the rising bubble and flow around the bubble in a streamwise fashion [15]. A portion of the particles, however, flow into a wake region as shown in Figure 1-11.

1.2.3 Gas-Solid Motion with Internal Surfaces

The gas-solid motion within a fluidized bed is greatly affected by the presence of immersed surfaces such as horizontal tubes.

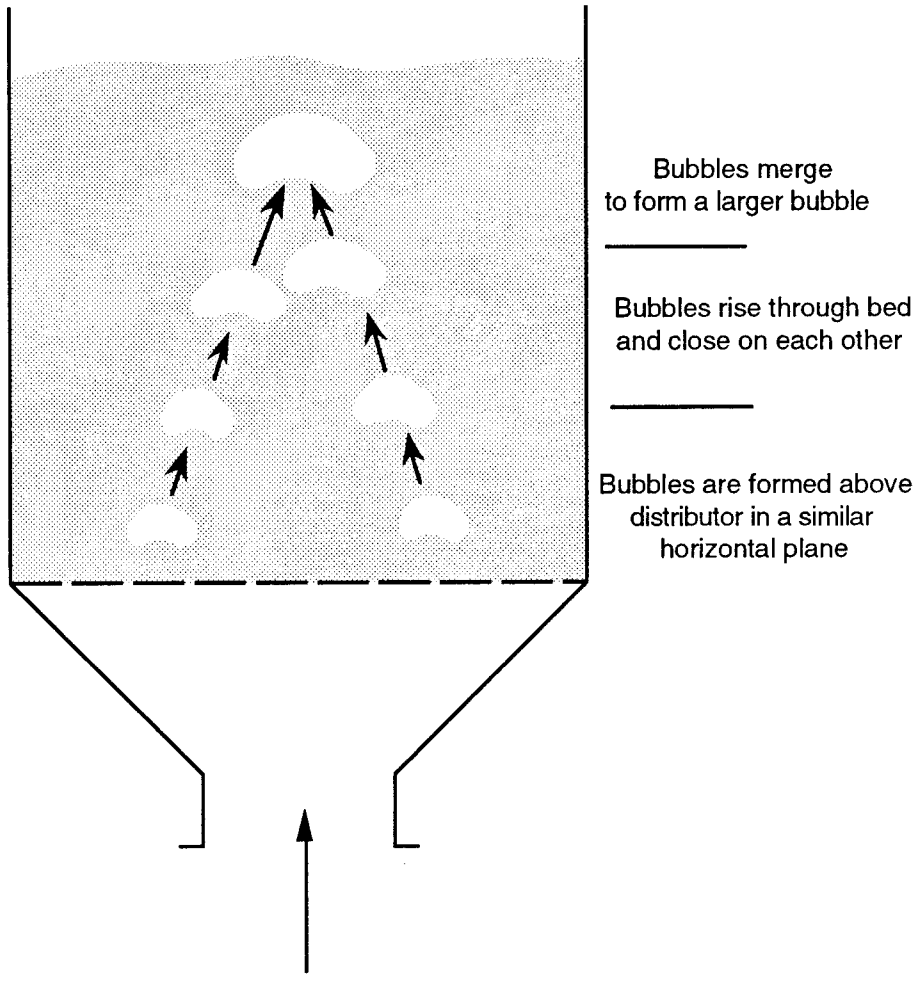

Figure 1-10: An Example of Bubble Coalescence -- Two Bubbles in a Similar Horizontal Plane Close on Each Other and Combine.

If a single tube is placed in a fluidized bed the following features are evident [8]:

a) an area of defluidized particles, known as a lee stack, forms on the downstream or leeward side of the tube as portrayed in Figure 1-12;

b) a bubble or thin film of gas is present at the upstream surface of the tube; and

c) bubbles nucleate at the surface tangent to flow due to the local acceleration of the gas.

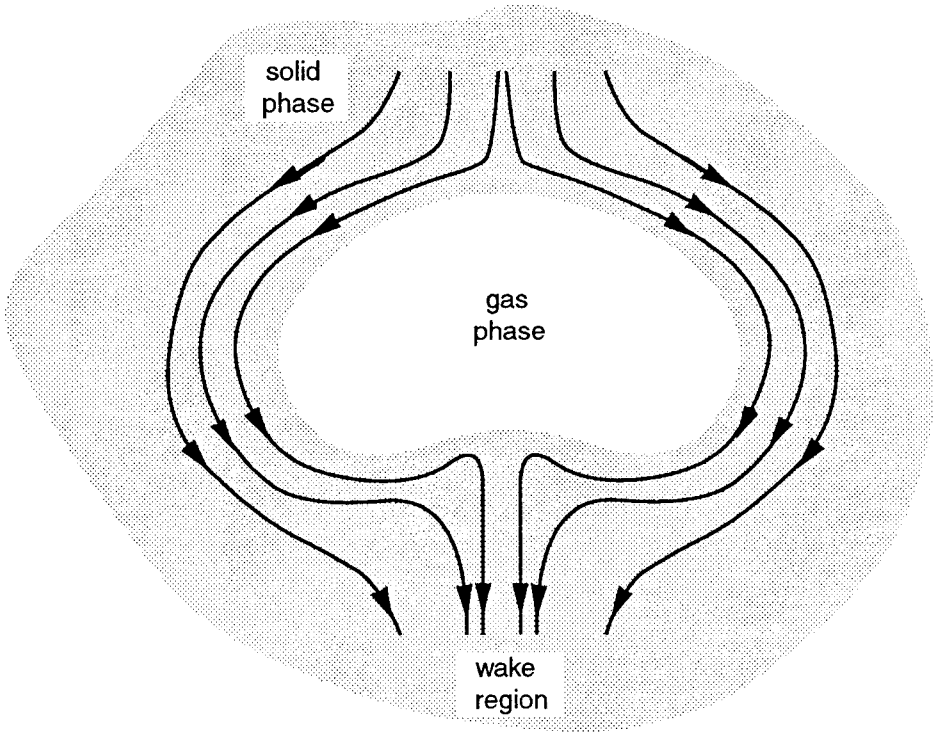

Figure 1-11: Particle Flow Around a Rising Bubble.

These features depend on bed conditions such as particle size, gas velocity, and geometry of the bed. For example, the same sized tube will sustain a larger lee stack in a two-dimensional bed geometry than in a three-dimensional case [13].

The presence of immersed surfaces can produce a variety of bubble patterns and size distributions which are dependent on the configuration of

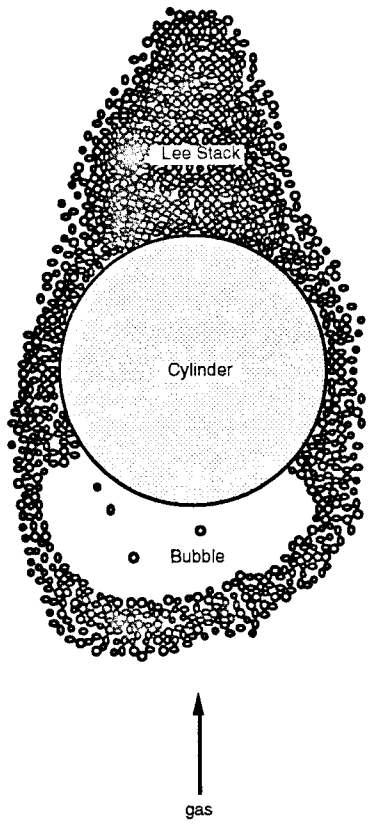

Figure 1-12: Illustration of an Immersed Horizontal Cylinder in a Bubbling Bed. Adapted from Goshayeshi [8].

the surfaces. Four possibilities are listed below:

a) at close spacing a particle bridge may form between neighboring surfaces impeding bubble flow;

b) rising bubbles may encounter the surfaces and break-up causing a smaller size distribution of bubbles;

c) rising bubbles may encounter the surfaces forcing the bubble to move laterally and coalesce with other bubbles forming a larger size distribution of bubbles; and

d) rising bubbles may interact with a surface forcing the bubbles to

move laterally and disrupt neighboring surfaces' defluidized caps.

1.3 Fluidized Bed Particles

As previously mentioned, the solids used as bed particles affect the hydrodynamics of a fluidized bed. Therefore, a brief discussion of particle properties, classification, and minimum fluidization velocity will be presented in the following sections.

1.3.1 Particle Properties -- Size and Shape

A popular and convenient approach to measuring the size of non-spherical solids used as bed materials is filtering them through a series of screens or sieves [10]. The result provides a distribution of particles sizes that lie between the screen sizes. For example, particles passing through a 2.00 mm aperture of a screen but not a 1.70 mm aperture produce a particle distribution between 1.70-2.00 mm. This type of analysis, screen analysis, assumes that the aperture approaches the diameter of the sphere of volume equal to that of the particle. Therefore, the shape of the particles is important.

One method of describing the shape of the particles is to compare it to a sphere of equal volume.

$$\phi_s \equiv \left(\frac{\text{surface of sphere}}{\text{surface of particle}}\right)_{\text{of same volume}} \tag{1.1}$$

Where ϕ_s is called the *sphericity*. Thus, a sphere has $\phi_s = 1$ and all other shapes have $0 < \phi_s < 1$ [10]. Sphericities of selected particles are provided in Table 1-1.

Table 1-1: Example Particle Sphericities [10].

Type of Particle	Sphericity
Sphere	1.00
Cube	0.81
Glass, crushed, jagged	0.65
Sand	
round	0.86
sharp	0.66
old beach	as high as 0.86
young river	as low as 0.53

1.3.2 Particle Classification

A commonly used scheme for the classification of particles was developed by Geldart [10]. The Geldart classification scheme was presented graphically in Figure 1-13 and as follows beginning with the smallest size and finishing with the largest. [6,7]:

- *Group C:* All powders with a mean size -- $\overline{d_p} < 30$ μm. The powders are cohesive and very fine causing high interparticle forces. Consequently, fluidization is difficult to achieve due to slugging effects. An example of this type of particle is flour.

- *Group A:* Particles of small mean size and/or low density (≈87 lb/ft^3). Due to the low density these particles are often porous. Group A particles are easily fluidized.

- *Group B:* Sandlike particles of size range 40 μm ≤ $\overline{d_p}$ ≤ 500 μm and density range 87 lb/ft^3 ≤ ρ_s ≤ 250 lb/ft^3. These types of particles fluidize well providing vigorous bubbling and large growing bubbles.

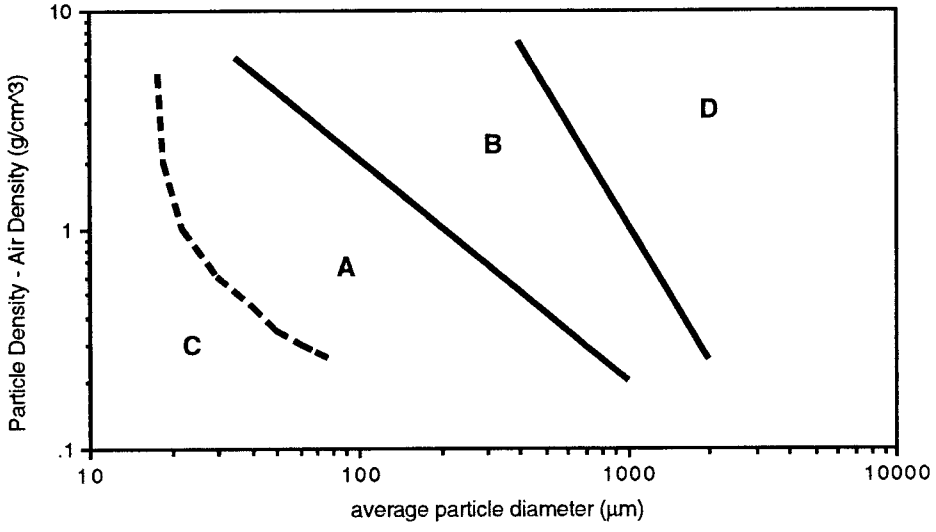

Figure 1-13: Geldart Particle Classification for Air at Ambient Conditions [7].

- *Group D:* Large and dense solids of mean size -- $\overline{d_p} \geq 500$ μm.

Particles can be difficult to fluidize with large bed heights. These particles cause adverse fluidization characteristics such as channelling.

Groups A and B are mostly used in fluidized bed catalytic crackers employed in the petroleum and petrochemical industries. However, group D is the most commonly used bed material in power plant combustion zones because the larger particles may be used with high gas velocities which limits the required equipment size. Also, the larger the particle size the easier it is to handle. The experiments conducted in this thesis used only group D particles.

1.3.3 Minimum Fluidization Velocity

The minimum fluidization velocity is dependent on the particle size. As previously noted, minimum fluidization of the bed particles occurs when

(drag force by upward moving gas) = (weight of particles)

or

$$\begin{pmatrix}\text{pressure drop}\\ \text{across bed}\end{pmatrix}\begin{pmatrix}\text{cross-sectional}\\ \text{area}\end{pmatrix} = \begin{pmatrix}\text{volume}\\ \text{of bed}\end{pmatrix}\begin{pmatrix}\text{fraction}\\ \text{consisting}\\ \text{of solids}\end{pmatrix}\begin{pmatrix}\text{specific}\\ \text{weight}\\ \text{of solids}\end{pmatrix} \quad (1.2),$$

and as shown by Kunii and Levenspiel [10] a general quadratic formula can be derived for the minimum fluidization velocity by equating the frictional pressure drop to the weight of the bed.

$$\frac{1.75}{\varepsilon_{mf}^3 \phi_s}\left(\frac{d_p\, u_{mf}\, \rho_g}{\mu}\right)^2 + \frac{150(1-\varepsilon_{mf})}{\varepsilon_{mf}^3 \phi_s^2}\left(\frac{d_p\, u_{mf}\, \rho_g}{\mu}\right) = \frac{d_p^3\, \rho_g (\rho_s - \rho_g)\, g}{\mu^2} \quad (1.3)$$

Where u_{mf} is the minimum fluidization velocity, ε_{mf} represents the void fraction at minimum fluidization, d_p is the particle diameter, ρ_g and ρ_s are densities of gas and air respectively, and μ is viscosity. A plot of the minimum fluidization velocity as a function of the particle diameter for the silica alumina particles used in this study is illustrated in Figure 1-14. Note that the values for each term of the equation are listed in the upper left hand corner. For a comparison between the analytical and experimental minimum fluidization velocities for the average particle sizes used in this research see Appendix B.

1.4 Bubble Measurement Techniques

Bubble behavior in a fluidized bed is stochastic in nature and consequently difficult to quantify. Understandably, many experimental techniques have been attempted. The experimental methods used up to the present can be classified as being either intrusive or non-intrusive.

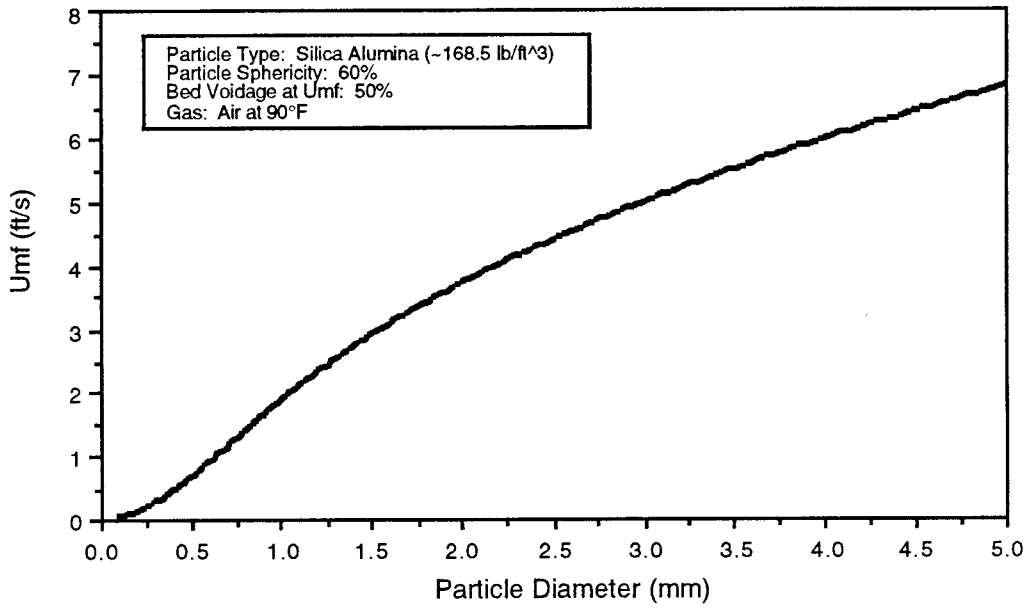

Figure 1-14: Minimum Fluidization Velocity vs. Particle Size.

1.4.1 Intrusive Methods

The flow in a fluidized bed is disrupted when intrusive methods are used since a foreign object, a probe, must be placed in the bed. The degree of disruption depends on the size of the probe being used. As a consequence, the output of the probe should be interpreted accordingly.

Therefore, intrusive probes must be small and compact so that the effects from the physical presence of the probe can be minimized.

The types of probes that fall under intrusive experimental methods are resistivity, capacitance, inductance, and optical probes.

Resistivity probes can only be used with liquids and conductive solids. Hence, they do not operate well in gaseous fluidized beds and those with low conductivity solids.

Capacitance probes are commonly used but have three disadvantages. First, the conductors (capacitance plates or needles) connected to the sensing element must be limited in size to avoid bed disruption thereby limiting their ability to operate effectively in large deep beds. Second, expensive instrumentation is required for the small conductors' high sensitivity needs. Third, calibration is necessary for every solid fluid system and operating condition (especially temperature and pressure).

Inductance probes use a magnetic field; and consequently, the bed materials must have magnetic properties. These probes also need sophisticated instrumentation for sensitivity.

Optical probes do not have any of the disadvantages of the aforementioned probes. Optical probes are simple in design and construction. They are also versatile since they can be used in large or small and hot or cold fluidized beds. However, for small optical probes the components can be difficult to maintain at a specified level because smaller optical components are highly sensitive to alignment.

1.4.2 Non-Intrusive Methods

Non-Intrusive techniques involve flash, video, motion picture, and X-ray photography. All of these methods require a two dimensional fluidized bed. This is a disadvantage since 2-D beds give valuable qualitative information, but extrapolation of information to larger 3-D beds is difficult [14]. Furthermore, all of these types of methods require an abundance of pictures to be taken and analyzed. This effort can be labor intensive whereas signals from probes can be processed by a computer.

2. EXPERIMENTAL APPARATUS

A two-dimensional gas-solid fluidized bed was constructed for visual and experimental observation of bed hydrodynamic behavior. The experimental apparatus consisted of three components:

a) cold-temperature 2-D gas-solid fluidized bed facility;
b) optical probes; and
c) instrumentation, and data acquisition hardware and software.

2.1 Description of Fluidized Bed Facility

The low-temperature fluidized bed facility consists of a gas supply system, orifice flow meter, and test section. A schematic of the fluidized-bed apparatus is illustrated in Figure 2-1.

2.1.1 Gas Supply System

Ambient air, used as the gas or working fluid, was initially passed through a filter to remove unwanted particulate before being drawn into an air pump.

The air pump was made up of a 3 phase induction motor, two silencers or mufflers, and Sutorbilt rotary positive displacement blower. Ideally, the blower should supply the same flow rate regardless of the system pressure requirements. However, the blower had a maximum pressure capacity of about 12 pounds per square inch (psi) at a volumetric flow rate of 85 cubic feet per minute (cfm), or a maximum volumetric flow rate of 100 cfm with

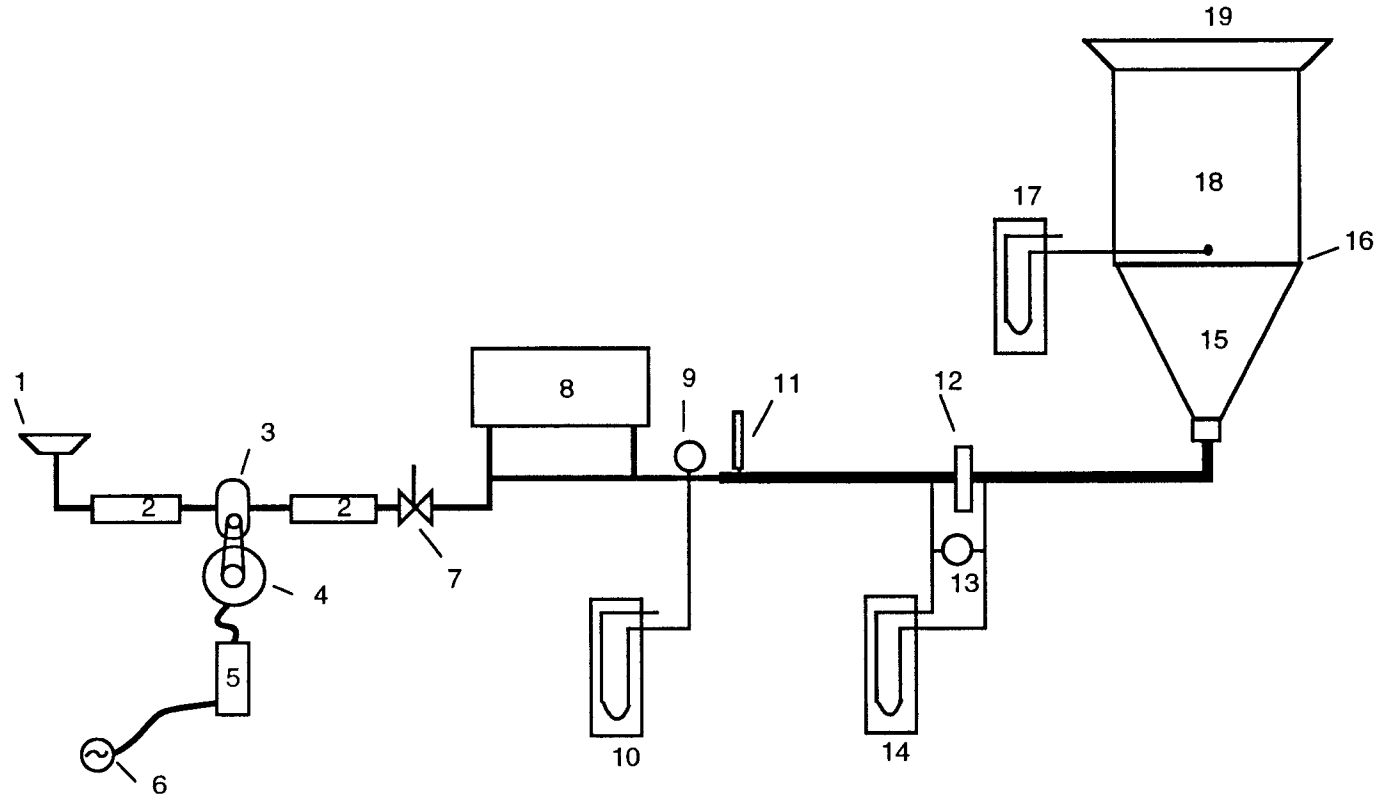

(1) air filter, (2) silencer, (3) Sutorbilt rotary positive blower, (4) GE 5 Hp 3 phase induction motor, (5) SECO 3 phase controller, (6) 3 phase power supply (7) pressure relief valve, (8) surge tank (9) upstream static pressure gage, (10) upstream static manometer, (11) mercury thermometer, (12) orifice plate, (13) differential pressure gage, (14) differential manometer, (15) plenum/transition, (16) distributor plate, (17) test section static manometer, (18) test section, (19) exhaust.

high pressure tubing — 1.5" steel piping — 3.25" PVC piping

Figure 2-1: Schematic Illustration of the Oregon State University Cold-Temperature Gas-Solid Fluidized-Bed Facility.

pressure capacity of 7 psi or less. The fluidized bed facility required a system pressure of 2 psi or less. Due to the noise produced by the rotating impellers, a muffler or silencer was placed in line on each side of the air blower.

The rate of air supplied to the test section was dependent on the speed of the blower. Therefore, by adjusting the motor speed, the superficial velocity of the fluidized bed could be regulated. The motor speed was adjusted by a SECO A.C. inverter. The SECO inverter established the motor speed by controlling the frequency and voltage of the 3 phase 220 Volt AC power supply. The frequency limits set on the SECO controller were 10 to 60 Hertz (Hz) which corresponded to the motor ratings recommended by the manufacturer.

A pressure relief valve was installed after the second muffler to prevent excessive pressures from damaging the blower. According to the manufacturer any pressure greater than 12 psi was considered excessive, but the relief valve was adjustable and could be set to any value below the maximum rated 12 psi. For the fluidized bed facility the relief valve was set to open at any pressure greater than 3 psi to prevent a loss of system integrity or manometer overflow.

Due to the nature of the rotating blower impellers an oscillation in the air flow was generated. In order to dampen out this oscillation and produce a constant volumetric flow rate effectively, a 1.9 cubic foot tank was placed in parallel with the piping following the pressure relief valve.

All components mentioned above were connected by 1.5-inch diameter steel piping. After the surge tank the steel pipe was expanded to 3.25-inch

diameter PVC piping to accommodate the orifice flow meter which was downstream of the surge tank. The orifice flow meter will be discussed in a later section.

The air passed through a plenum/transition following the orifice flow meter. The transition expanded the air flow from the 3.25-inch diameter pipe to a 4 by 30 inch rectangular cross-section at which point the air passed through a distributor plate into the test section.

Finally, the air was vented back to the ambient after flowing through the test section.

2.1.2 Orifice Flow Meter

An orifice flow meter was incorporated into the apparatus to measure the superficial velocity. The flow meter was designed in accordance with ASME standards [1]. The equations and flow chart of the program used to make the flow calculations are included in Appendix C.

The flow meter was located at the 1.5-inch steel to 3.25-inch PVC pipe transition with a fluid-filled manometer, pressure gage, and mercury-filled thermometer. The manometer was used to measure the upstream static pressure accurately, while the pressure gage was used for checking the manometer. The thermometer was placed in direct contact with the issuing air so that its temperature could be quickly measured (i.e. no time lags from thermometer wells). The upstream pressure tap was followed by a calming section of more than ten pipe diameters. A flange and orifice plate were located at the end of the calming section. The orifice plate pressure drop was measured by taps located one pipe diameter upstream and one-half

pipe diameter downstream. A differential fluid-filled manometer and gage were used to read the pressure drop. Once again the manometer was used for accurate measurement while the gage was used as a check. The orifice plate was followed by another calming section of more than ten pipe diameters. The last component of the flow meter was the test section static fluid-filled manometer. This manometer was used to calculate the air density in the test section so that the superficial bed velocity could be calculated from the mass flow rate.

2.1.3 Test Section

The test section was designed and constructed to allow observation by both intrusive and non-intrusive methods (i.e. optical probes and video camera respectively). The test section was rectangular in shape with a frontal area of 1.25 inches deep by 27 inches wide, and a height of 18 inches. The test section was mounted inside a rigid steel support frame or superstructure. The superstructure was 6 inches deep, 30 inches wide and 18 inches tall, and it was bolted to the plenum/transition with a 0.25-inch thick steel plate placed in between. The distributor plate and test section were mounted on the 0.25 inch steel plate, and it had a 1.25 by 27-inch slot that allowed air from the plenum to reach the test section via the distributor plate. The slot was surrounded by a 0.125 inch inset or lip that accepted the front, back, and sides of the test section. The front of the test section was a 0.125-inch-thick scratch-resistant plexiglass which was used because it allowed application of high clamping forces. The back was a 0.125-inch-thick aluminum sheet, and the sides were 1.25 inch square Aluminum tubing. The

plexiglass was placed up against the inside front of the steel superstructure. The side tubing was seated at each end behind the plexiglass front. Finally, the back sheet fit in snugly behind the tubing. All interfaces had rubber-cork gasket material to prevent leaks. The interfaces with the plexiglass and support structure also had neoprene foam for improved sealing. On each end of the superstructure's back side, three clamps were used to apply horizontal pressure to the test section to provide a seal. In addition, on each end of the superstructure at the top, a clamp was used to apply vertical pressure to the back and sides of the test section to facilitate sealing. The bottom interface between the aluminum backing and the steel plate was sealed with duct tape to stop any leaks that the rubber-cork gasket did not prevent.

The distributor plate, located on the bottom side of the 0.25-inch steel plate, provided sufficient flow resistance or pressure drop that forced the incoming air to be uniformly distributed across the bed. The distributor plate was designed to force a 12 inch of water pressure drop at the most commonly used flow rates of 70 to 80 cfm. A graph of the distributor plate pressure drop versus the flow rate is portrayed in Figure 2-2. The distributor plate was a 0.125-inch-thick aluminum sheet with 165 evenly spaced holes. The holes were arranged in 3 rows of 55 and were 0.09375 inches in diameter. The holes were evenly spaced over the 1.25 by 27-inch area at one-half-inch between centers. The free flow area of the plate was about 1.14 square inches. The distributor plate and a fine mesh screen were screwed to the bottom side of the 0.25-inch steel plate. The screen was installed to prevent small particles from falling through the distributor plate.

Likewise, at the top of the test section a coarse screen was mounted to prevent particle spillage.

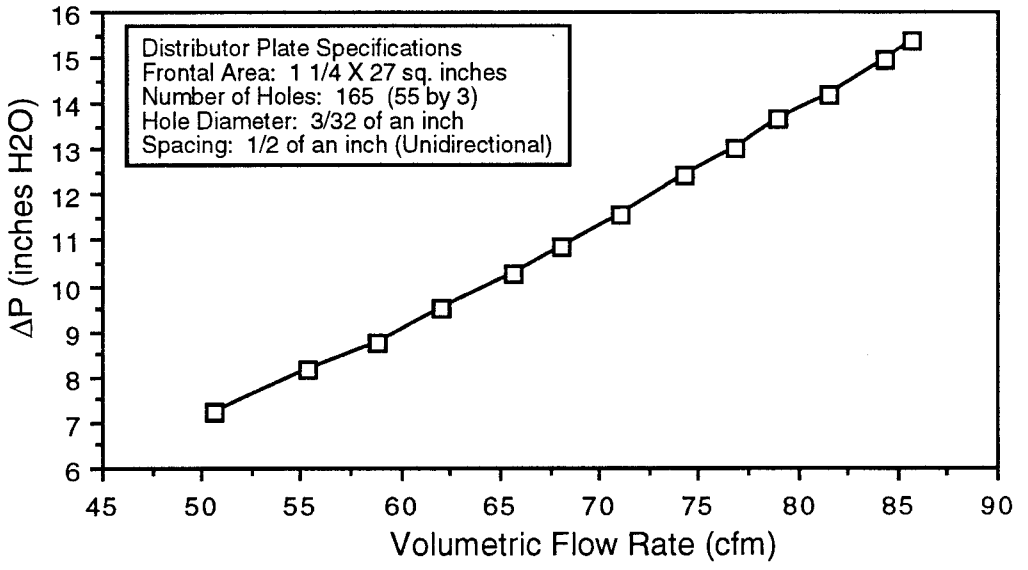

Figure 2-2: Pressure Drop Across Distributor Plate vs. Volumetric Flow Rate

The presence of immersed surfaces, such as arrays of tubes carrying water-steam working fluid in a power plant, have an affect on the fluidized bed hydrodynamics. Therefore, the test section was designed to accommodate an arrangement of internal surfaces to study their effects on the bubbling behavior of the 2-D bed. The internal surfaces used were immersed 2-inch-diameter horizontal tubes. The test section could either be set-up for one or two horizontal tubes at a height of 4 inches above the distributor plate or for no horizontal tubes. A single tube could be placed in the horizontal center of the test section or two tubes could be placed at a center-to-center distance of 3, 4, or 5 inches. The tubes were mounted by using a bolt that passed from the front of the bed to the rear with o-rings to

prevent air leaks. The holes were taped off when not in use. The test section is depicted in Figures 2-3a and 2-3b with a single horizontal tube in the center. For an illustration of the possible horizontal tube arrangements see Figure 2-4.

The optical probe tips were mounted horizontally through the rear of the test section. The horizontal mounting of the probes was beneficial since only the probe tips were exposed to the fluidized bed. The probes could have been mounted vertically, but they would have caused significant obstruction to the flow as compared to just the probe tips. The horizontal mounts provided the least flow obstruction of the two mounting methods. There were eleven locations for each probe or twenty-two locations in all. The lower probe was located six inches above the distributor plate with a second probe located two inches above the first probe. The probes used o-rings to minimize air leakage. The possible probe locations are portrayed in Figure 2-5.

2.2 Optical Probes

Experimental observations of fluidized bed hydrodynamics were recorded by the use of two optically sensing probes that were constructed by Alan H. George of Montana State University for operation in both hot and cold fluidized beds.

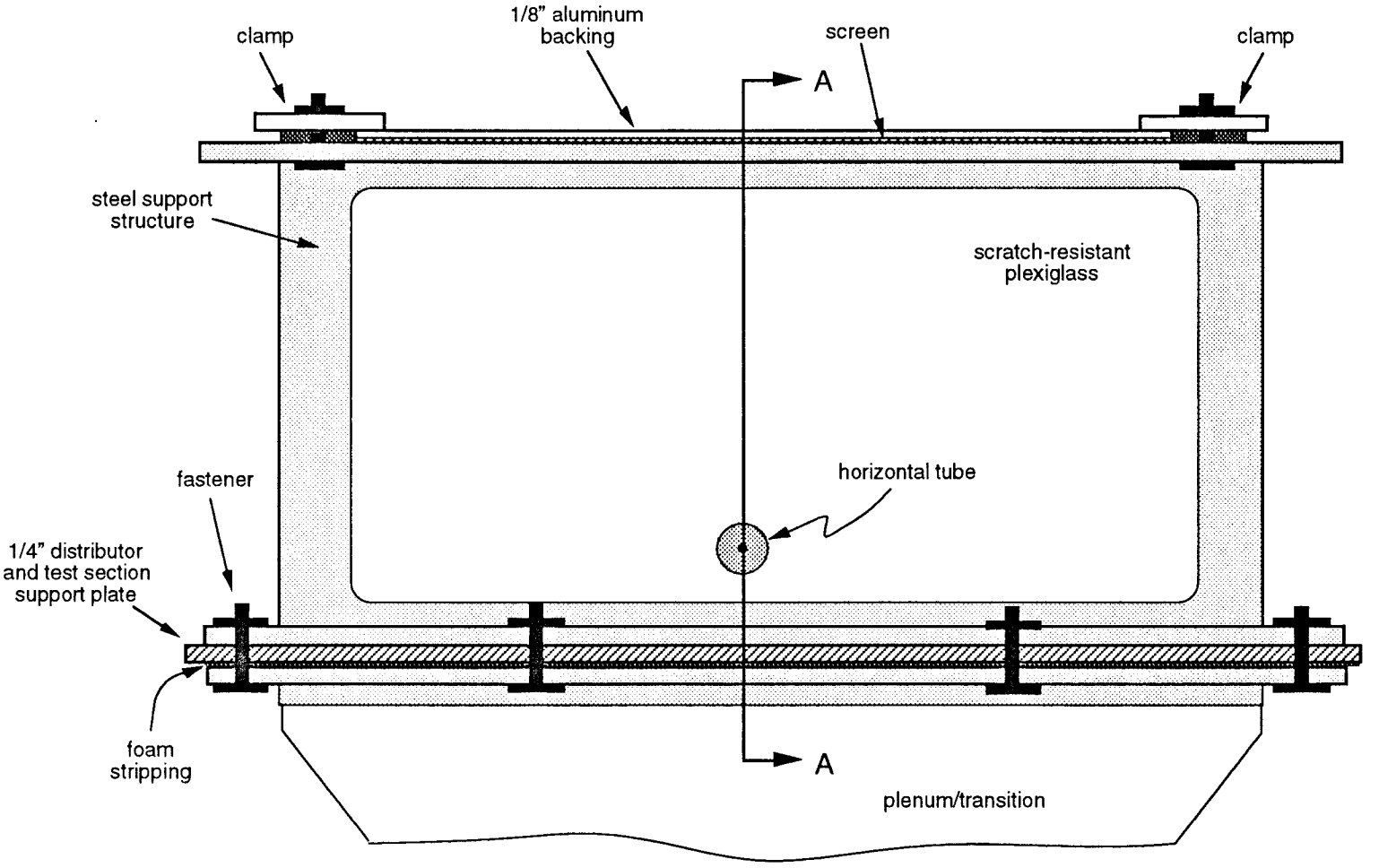

Figure 2-3a: Front View of Test Section. (not to scale)

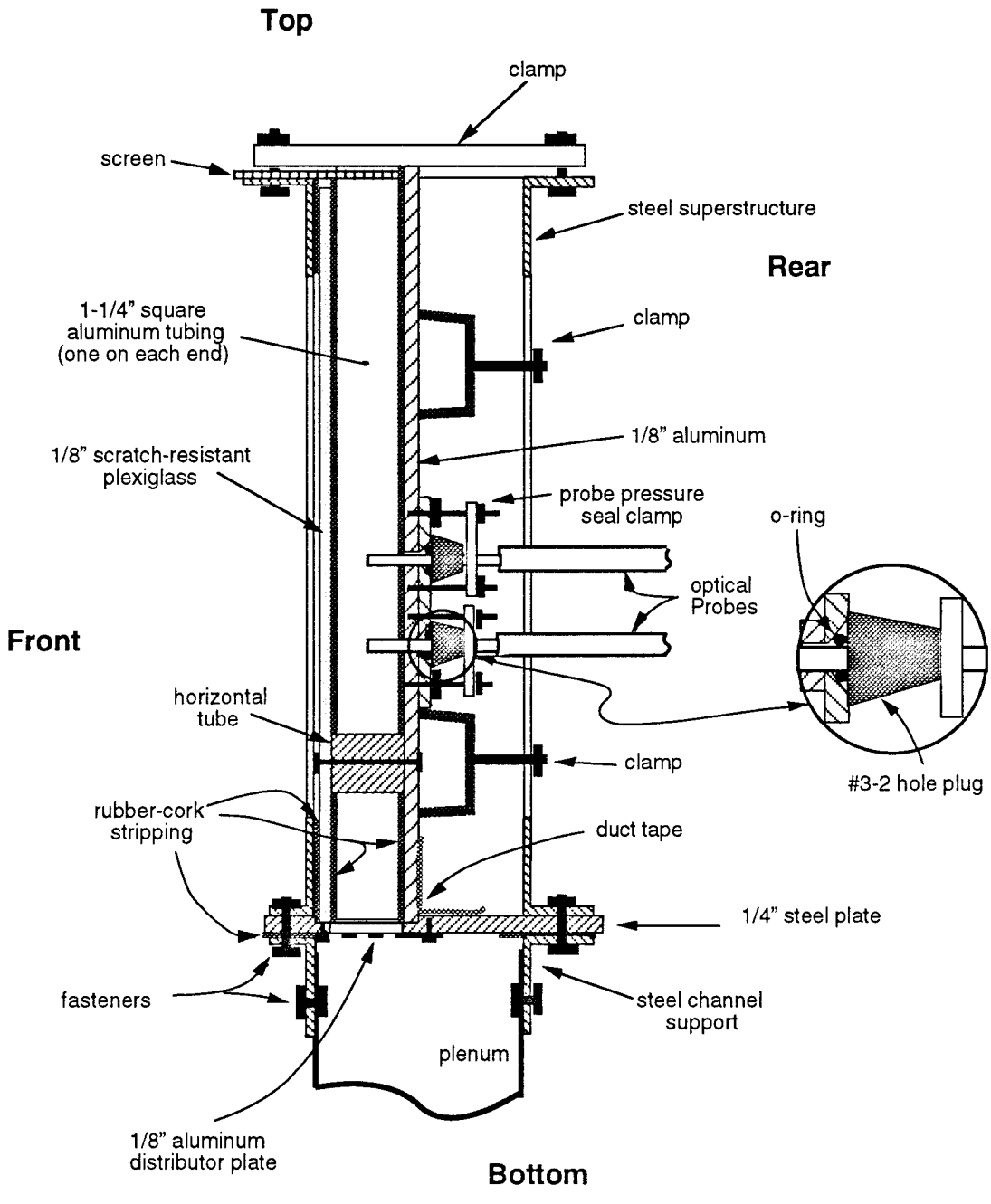

Figure 2-3b: Cross-Sectional View A-A of Test Section.
(not to scale)

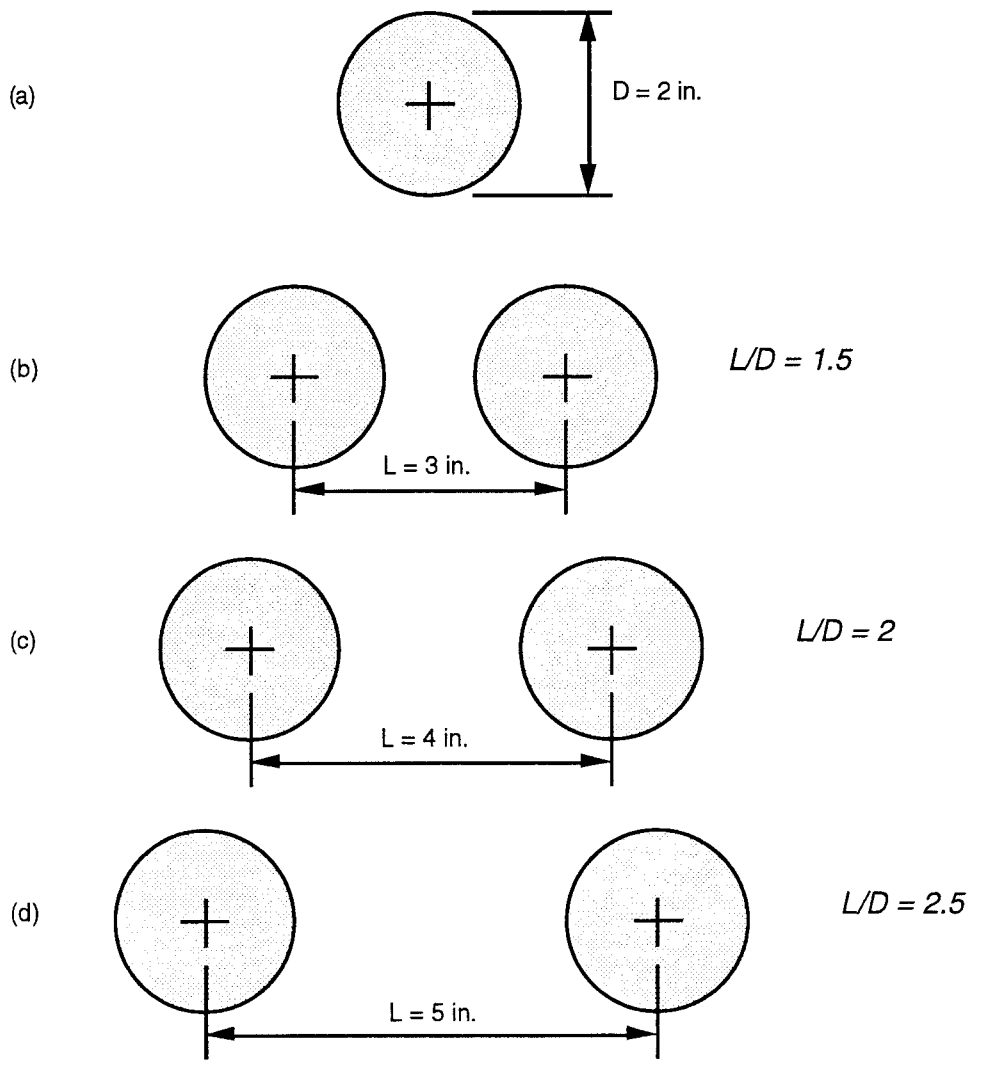

Figure 2-4: Internal Surface Arrangements (1/2 scale).

The optical probes used a high intensity light emitting diode (LED) as a source of light. The LED emitted infrared radiation at a spectral peak of 880 nm. A silicon infrared phototransistor was used to detect the emitted light via an optical arrangement of fused quartz rods. The LED was located at a flat end of a 0.079 inch (2 mm) fused quartz rod, and the emitted light was transmitted down the rod. At the end of the rod was a 45°-angled-surface

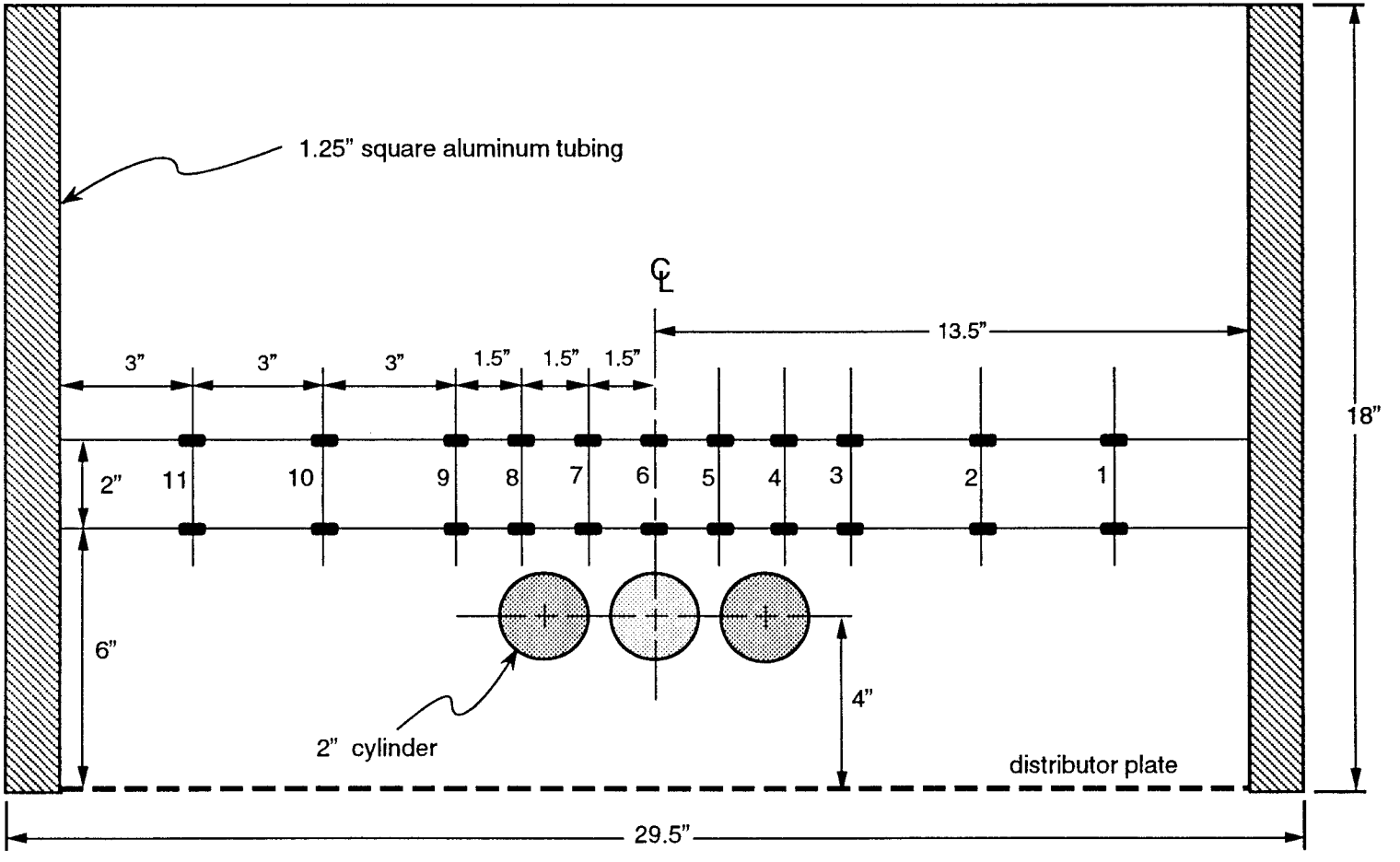

Figure 2-5: Location of Optical Probes and Horizontal Cylinders.
(Note: only 2 of the 4 possible cylinder arrangements was shown here.)

that deflected the light 90° onto a flat surface that allowed the light to leave the rod. Across a gap of 0.375 inch was a second 2 mm quartz rod that also had a flat surface followed by a 45°-angled-surface. The light would strike the flat surface and pass into the rod and then deflect up it at the 45°-angled-surface. At the top of the second rod was the light detector or phototransistor. The light path through the optical probes is portrayed in Figure 2-6. All surfaces were carefully ground and then polished in a hot flame to produce maximum transmittance at the flat surface and maximum reflectance at the angled surfaces. Both probe rods were encased in a stainless steel tube that could act as a coolant channel, while each quartz rod was placed in an Inconel tube for support. A detailed drawing of an optical probe is provided in Figure 2-7.

When opaque particles occupied the gap, no light was transmitted and consequently the signal was at a level of 0 volts. When an air bubble occupied the gap, light was transmitted across the gap producing a signal of approximately 2.5 volts. The output voltage was variable depending on the user's requirements. Typical probe output is shown in Figure 2-8.

2.3 Instrumentation and Data Acquisition

The instrumentation used to monitor, process and record the optical probe signals consisted of the probe signal conditioning unit, level discriminator, and an IBM XT personal computer as shown in Figure 2-9.

2.3.1 Optical Probe Signal Conditioning Unit

An excitation current in the form of a sine wave at approximately 1 kHz

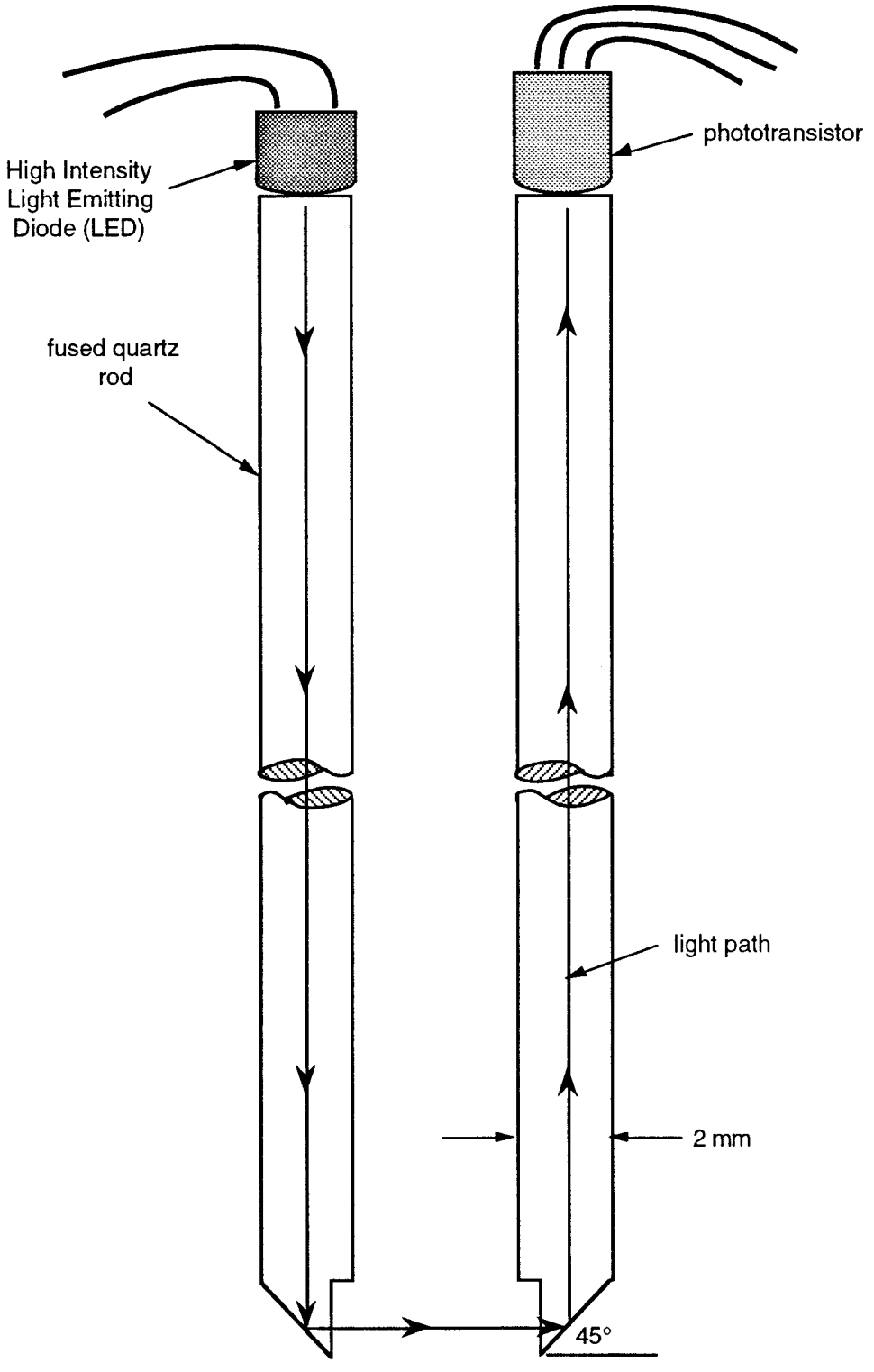

Figure 2-6: Light Path Through Optical Probe.

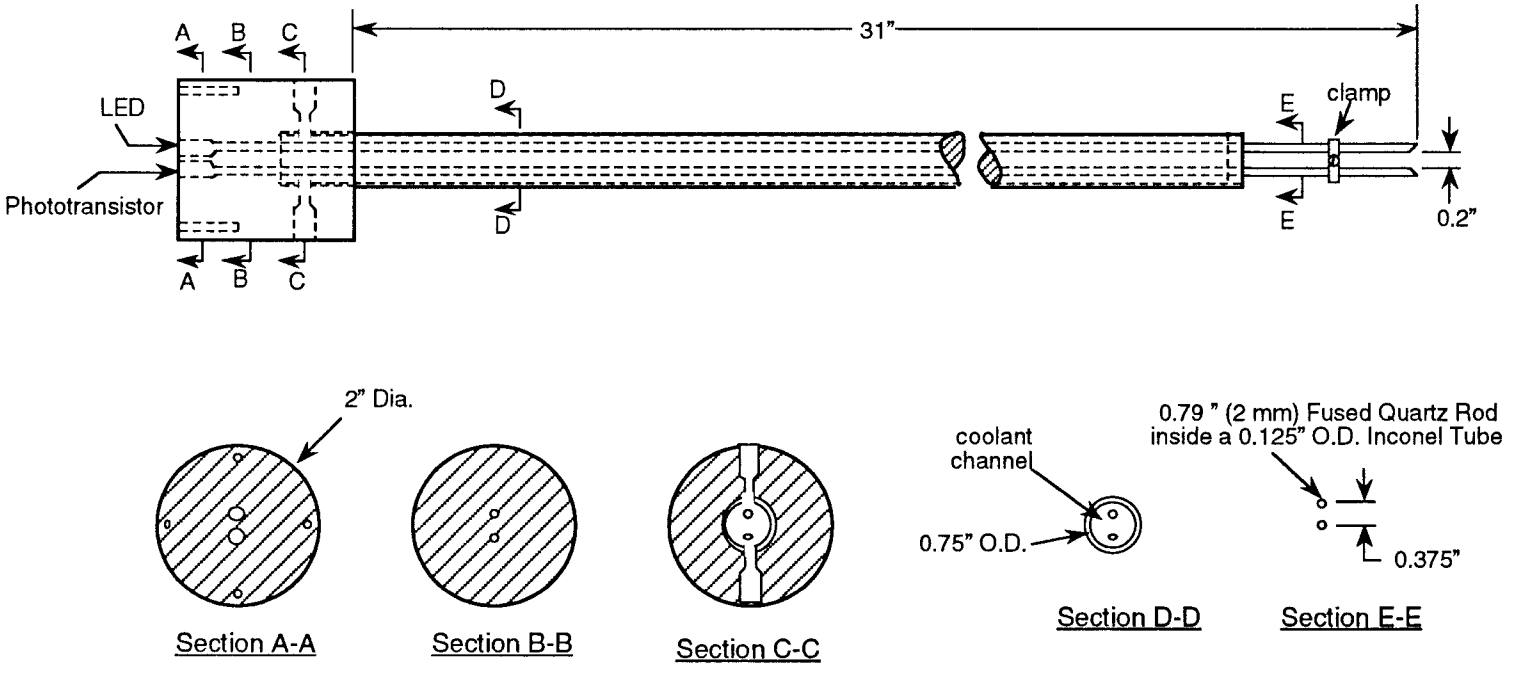

Figure 2-7: Detailed Drawing of Optical Probe (not to scale).

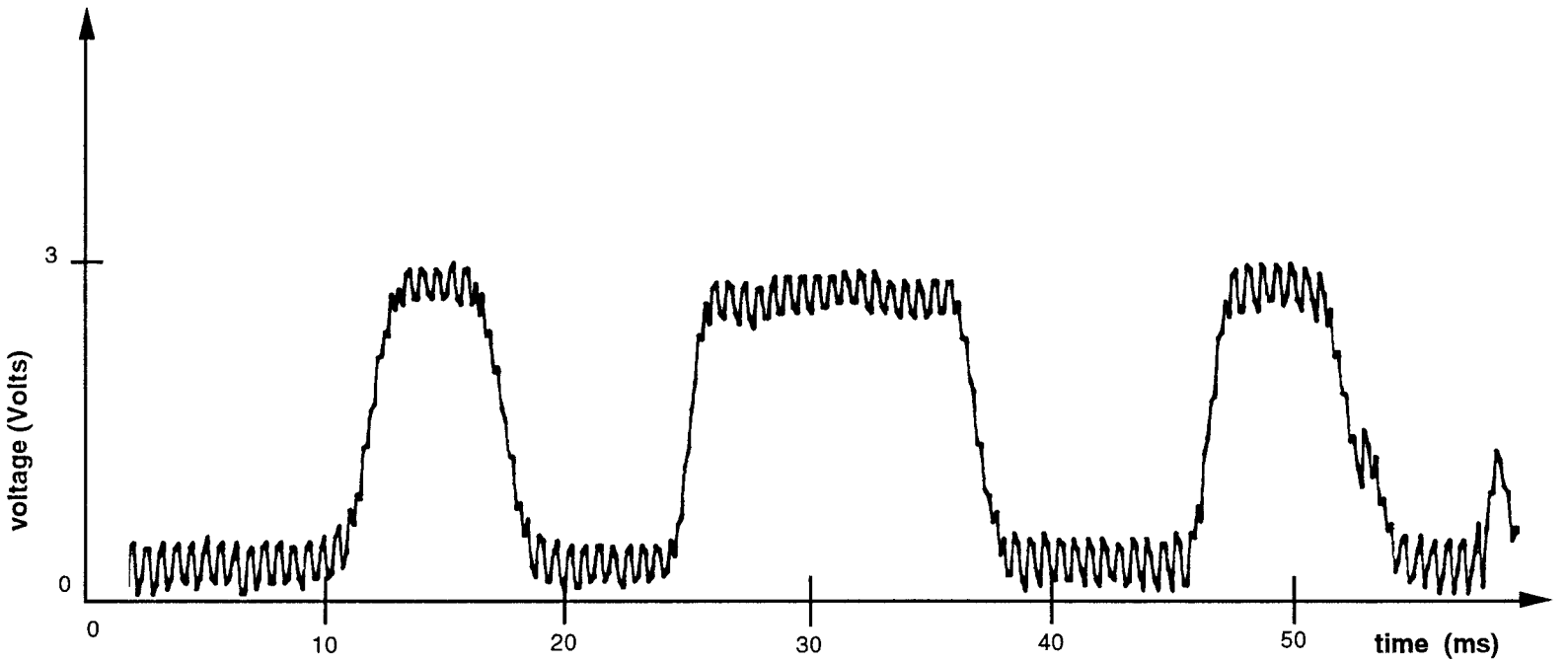

Figure 2-8: Typical Output of Optical Probe when placed in a Bubbling Fluidized Bed.

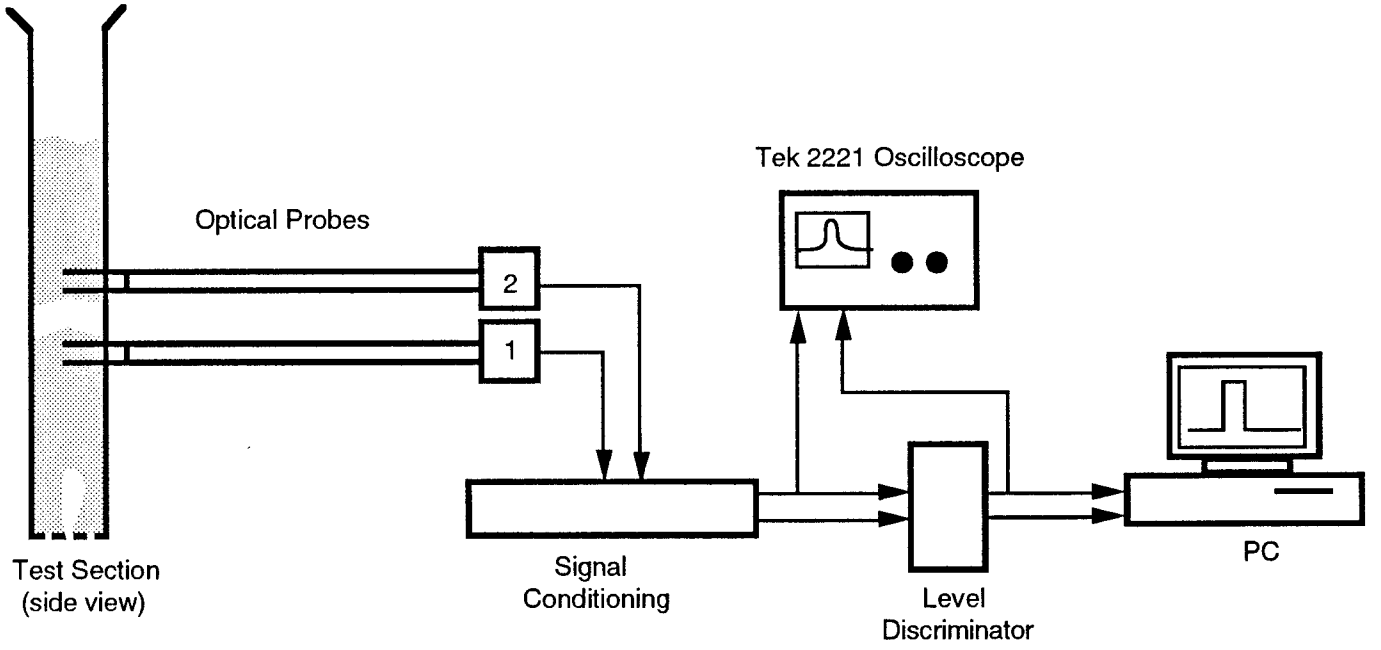

Figure 2-9: Organization of Instumentation.

was supplied to the LED of each optical probe. The nominal value of the current was large enough so that it could not become negative. As a result the light transmitted across the gap to the phototransistor was sinusoidal with some offset. The phototransistor output was sent through a high pass filter to remove all lower frequency components such as slowly fluctuating light emission from a hot radiating bed or any 60 Hz noise from AC power lines and overhead lights. Thus, the signal conditioning unit allowed the transfer of useful information at a carrier frequency of 1 kHz, while unwanted lower frequencies were filtered out. The remaining sinusoidal signal was amplified to about 2.5 volts. The signal was also offset such that when the light was attenuated the signal would read zero. The output of the signal conditioning unit was effectively a square wave that represented the bubble phenomena.

2.3.2 Level Discriminator

The level discriminator read the input voltage and compared it with a reference voltage. If the input voltage was greater or nearly equal to the reference voltage then the discriminator produced a logical one as an output. However, if the voltage was lower than the reference voltage, then the output was a logical zero. The logical one or zero depend on the digital computer being used. For the IBM unit used in this experiment, a logical one was approximately 3.5 volts and a logical zero was about 0.5 volts. Thus, with an analog input the level discriminator produced a digital output while still retaining the important pulse-width information.

A Tektronix 2221 oscilloscope was used to monitor the input and output of a single channel of the discriminator to insure proper operation and

reference voltages. The dual-channel level discriminator is schematically illustrated in Figure 2-10a and 2-10b and actual input/output is shown in Figure 2-11. For a circuit diagram of the level discriminator see Appendix D.

2.3.3 IBM XT Personal Computer

By using An IBM XT personal computer data collection was made simple and expedient. The computer was used to sample the output of the level discriminator at a rate of 500 samples/sec over a time of 5 seconds using a PC Lab digital input/output board with compiled optimized BASIC code. By using the digital I/O board, faster and more efficient data sampling was possible. For example, data could be sampled at 1500 samples/sec for 5 seconds, or data could be sampled at 500 samples/sec for 15 seconds. However, by trial and error the 500 samples/sec proved to be sufficient sampling frequency. This sampling frequency was also well above the recommended value of 10 times over sampling of measured phenomenon since bubble frequency was well below 50 bubbles/second and bubble pierced lengths were well above the 0.002 seconds/sample.

The wiring at the I/O port was such that only four numbers could be recorded. If neither probe was giving a signal above the reference voltage, a zero was recorded. If only probe 1 (the lower probe) was producing a signal, one hundred and twenty-eight was recorded. Likewise, if only probe 2 was producing a signal, sixty-four was recorded. Finally, if both probes were providing signals, one hundred and ninety-two was recorded. From this information the numbers were separated into probe 1 and probe 2 data and recorded on disk along with the sampling period and sampling frequency..

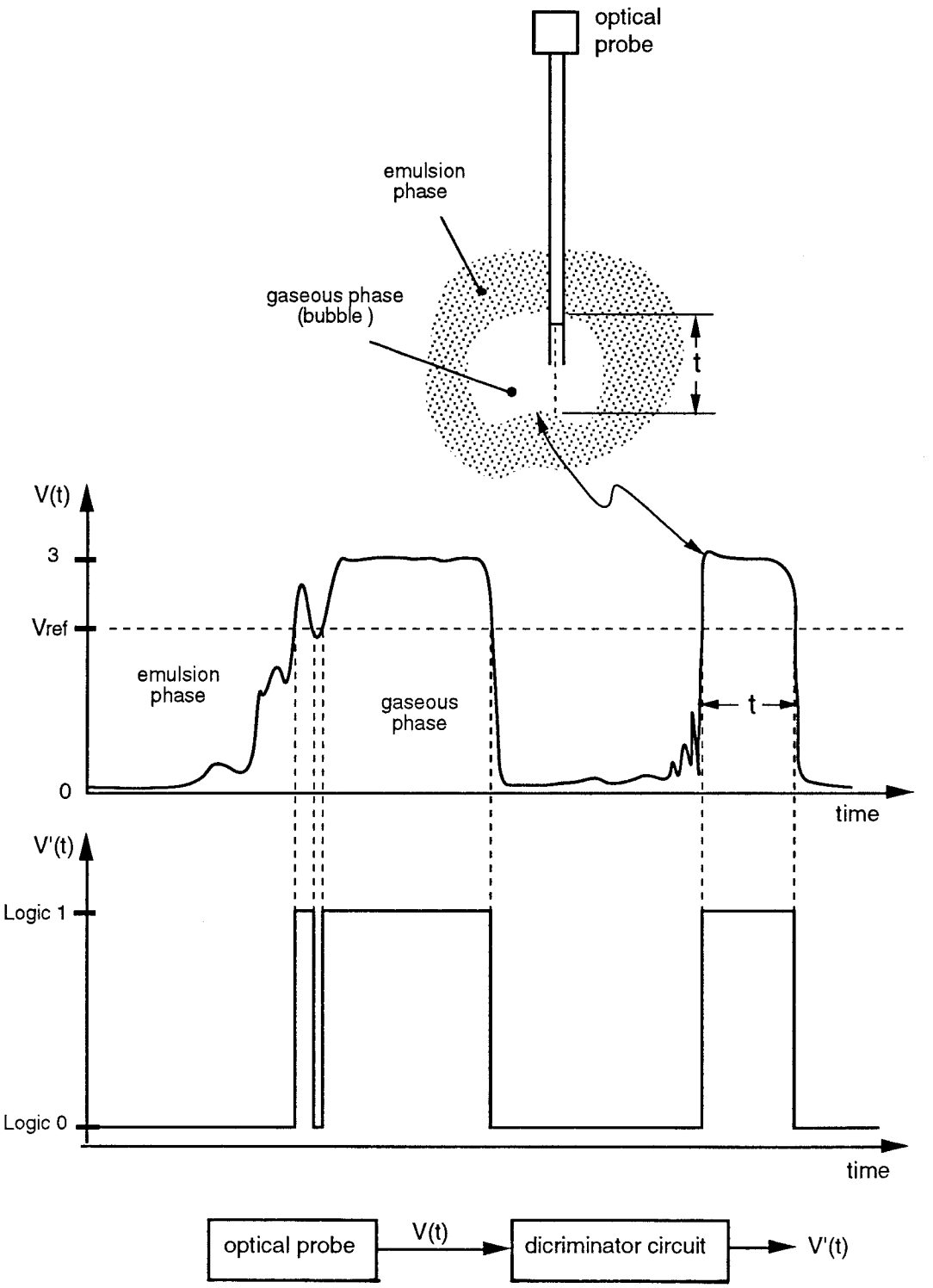

Figure 2-10a: Processing of Probe Signal.

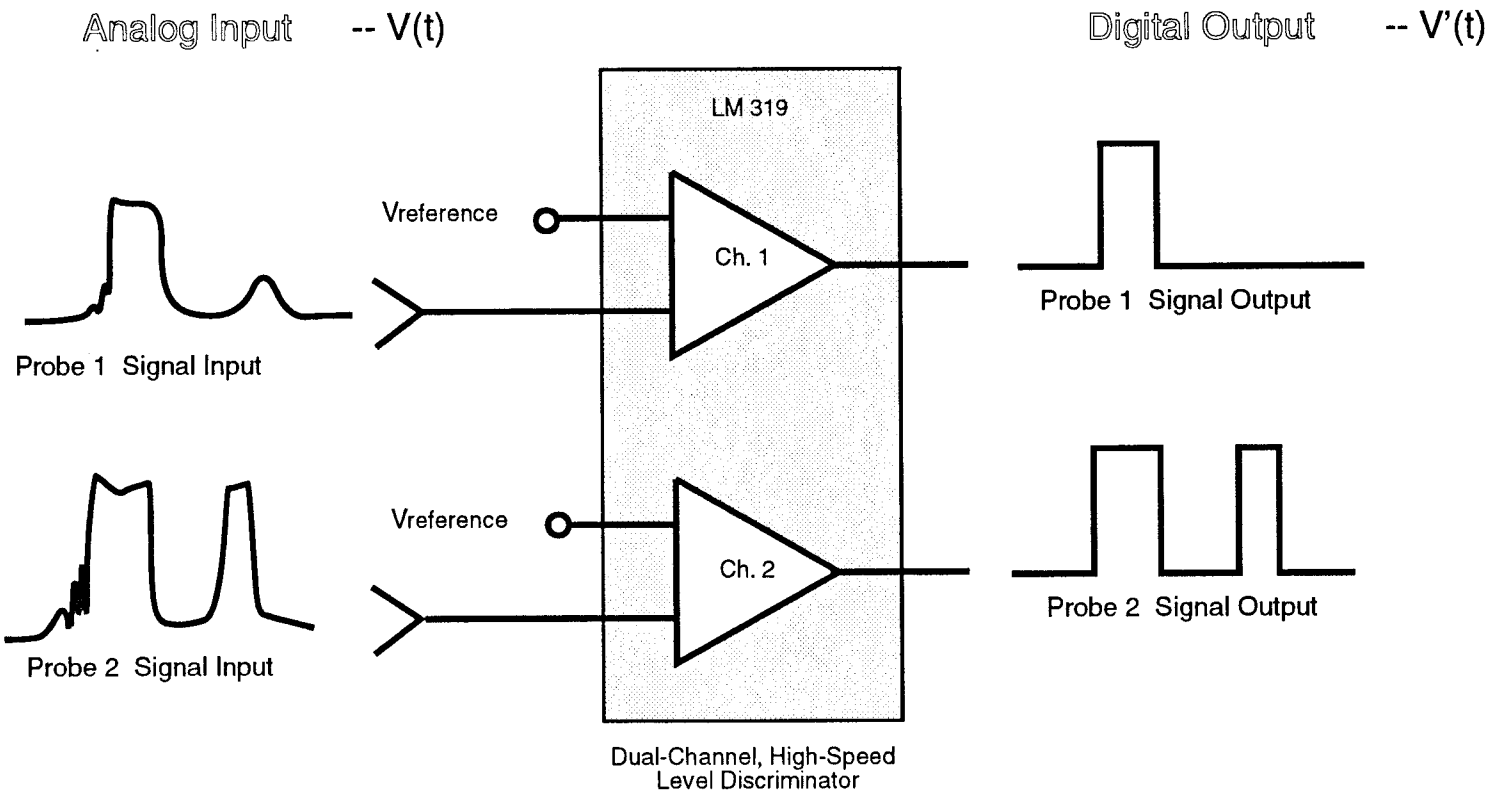

Figure 2-10b: Input/Output of Level Discriminator.

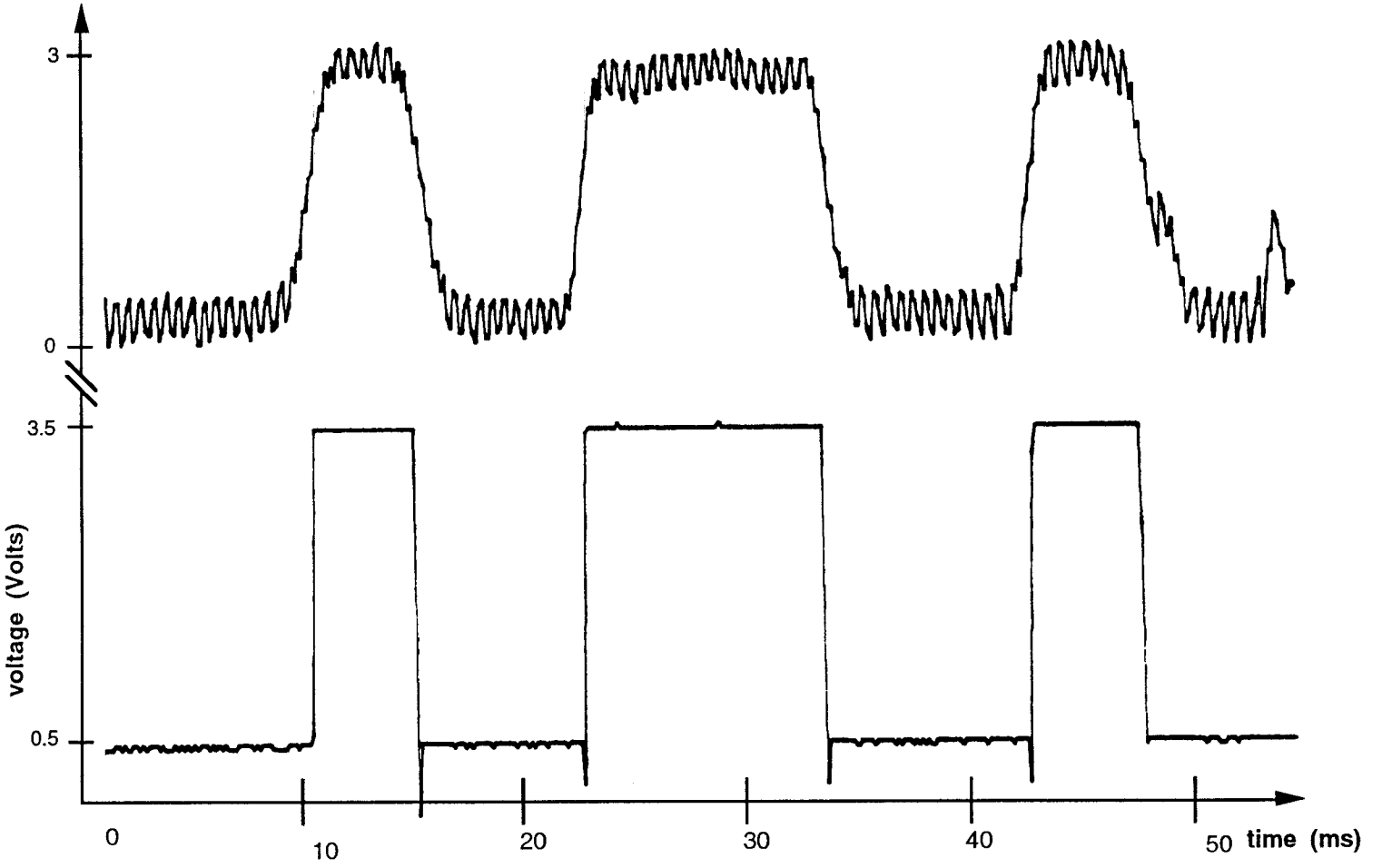

Figure 2-11: Typical Input and Output of Level Discriminator.

Also, the user inputted the necessary flow parameters such as temperature, pressure drops, static pressures so that the data reduction program could accurately calculate the flow conditions at which the data was taken.

3. EXPERIMENTS

The overall goal of this research is to characterize fluidized bed hydrodynamics under a variety of conditions. The bubble phase is the area of concentration; it can be described by properties such as bubble frequency, inter-arrival time, rise velocity, and pierced length. A measure of these variables was accomplished by recording and correlating pulse-width data from the optical probes at discrete locations across the fluidized bed. From these measurements, hydrodynamic signatures or characteristics of the 2-D fluidized bed were obtained.

3.1 Bubble Properties

As discussed above, the bubble behavior was derived from the signals of two optical probes. The first or bottom probe was used as the primary source for this objective. The second probe was necessary to help determine the bubble rise velocity. In other words, the first probe was used to calculate bubble frequencies, inter-arrival times, pierced lengths, and -- with the signal from the second probe -- bubble rise velocities (see Figure 3-1). The aforementioned bubble properties are described and discussed as follows:

a) Frequency: The number of bubbles passing a fixed location per unit time

$$\text{bubble frequency} \equiv f_b = \frac{\text{Number of Bubbles}}{\text{Sampling Period}} = \frac{N_b}{\tau_{sp}} \qquad (3.1)$$

The frequency of bubble occurrence across a fluidized bed contributes to the hydrodynamic description of a fluidized bed by providing a measure of

bubble uniformity. If the frequency of bubble occurrence is nearly constant across the bed then uniform bubble distribution most likely exists. However, if the frequency is high in one location and low in another then a channelling and circulation condition prevails. The frequency of bubble occurrence is dependent on the distributor plate since that is where the bubble form. If the distributor plate is well designed the bubble formation should be even across the bed.

b) Inter-Arrival Time: The time lapse between two successive bubbles.

$$\text{inter-arrival time} \equiv \tau_{ia} = (\text{time of bubble})_{i+1} - (\text{time of bubble})_i = (\tau_b)_{i+1} - (\tau_b)_i \quad (3.2)$$

The delay times between successive bubbles can provide a second

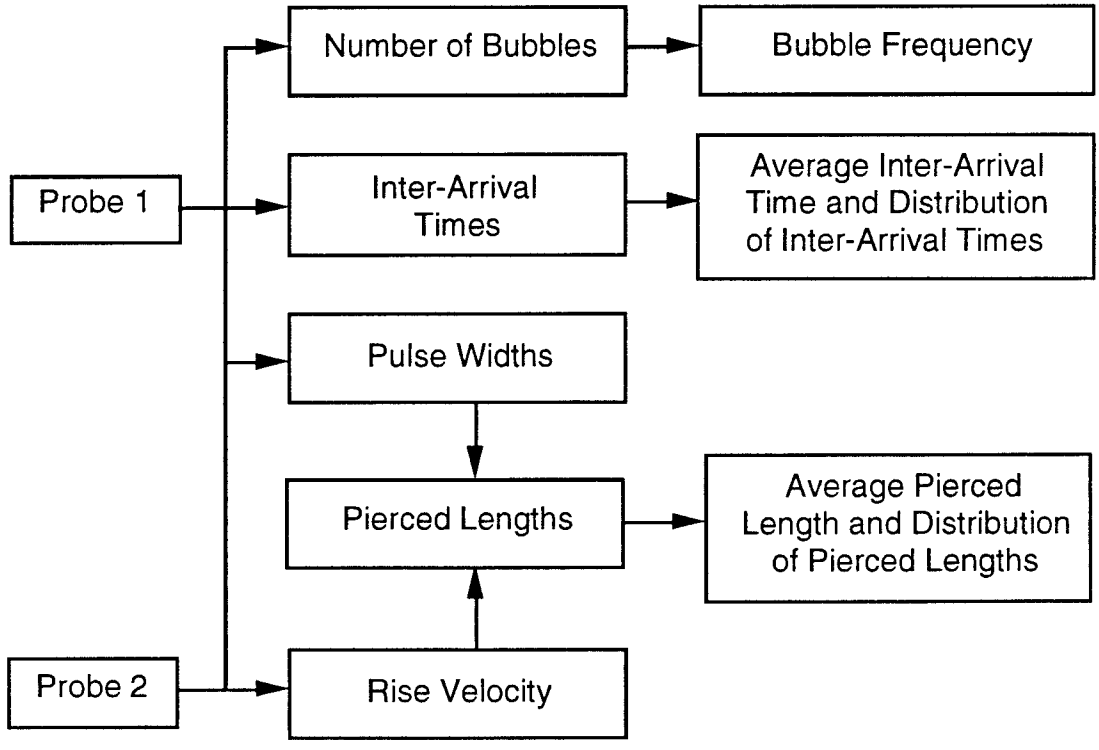

Figure 3-1: Flowchart of Determined Bubble Properties.

representation of fluidization quality just as the bubble frequency. That is, the inter-arrival times indicate how uniformly the bubbles are distributed spatially across a fluidized bed. If the inter-arrival times are approximately equal across a bubbling bed then the bubbling is approximately even and uniform. But if the inter-arrival times are relatively short in one location as compared to other locations, an adverse flow pattern such as channelling most likely exits. Thus, the inter-arrival times contribute to fluidized bed hydrodynamics much like the bubbling frequency as a measure of overall bubbling uniformity.

c) Rise Velocity: The speed of a bubble rising through the bed. Figure 3-2 illustrates the use of two optical probes for calculating the rise velocity of bubbles.

$$\text{bubble rise velocity} \equiv U_b = \frac{\text{distance between probes}}{\text{time shift between probe signals}} = \frac{\Delta L}{\Delta t} \qquad (3.3)$$

The bubble rise velocity contributes to fluidized bed hydrodynamic as a measure of bubble residence time within the bed. Generally, the more rapid the bubble development the shorter the residence time and vice versa [15]. The bubble rise velocity is also used for calculating the pierced lengths of bubbles. The rise velocity can be difficult to measure due to factors such as bubble coalescence and break-up.

d) Pierced Length: The bubble chord length where it passed through the probe is determined as follows:

$$\text{pierced length} \equiv l_b = (\text{bubble rise velocity})(\text{bubble pulse width}) = (U_b)(\Delta\tau_b) \qquad (3.4)$$

Bubble size is an important factor for determination of fluidized bed

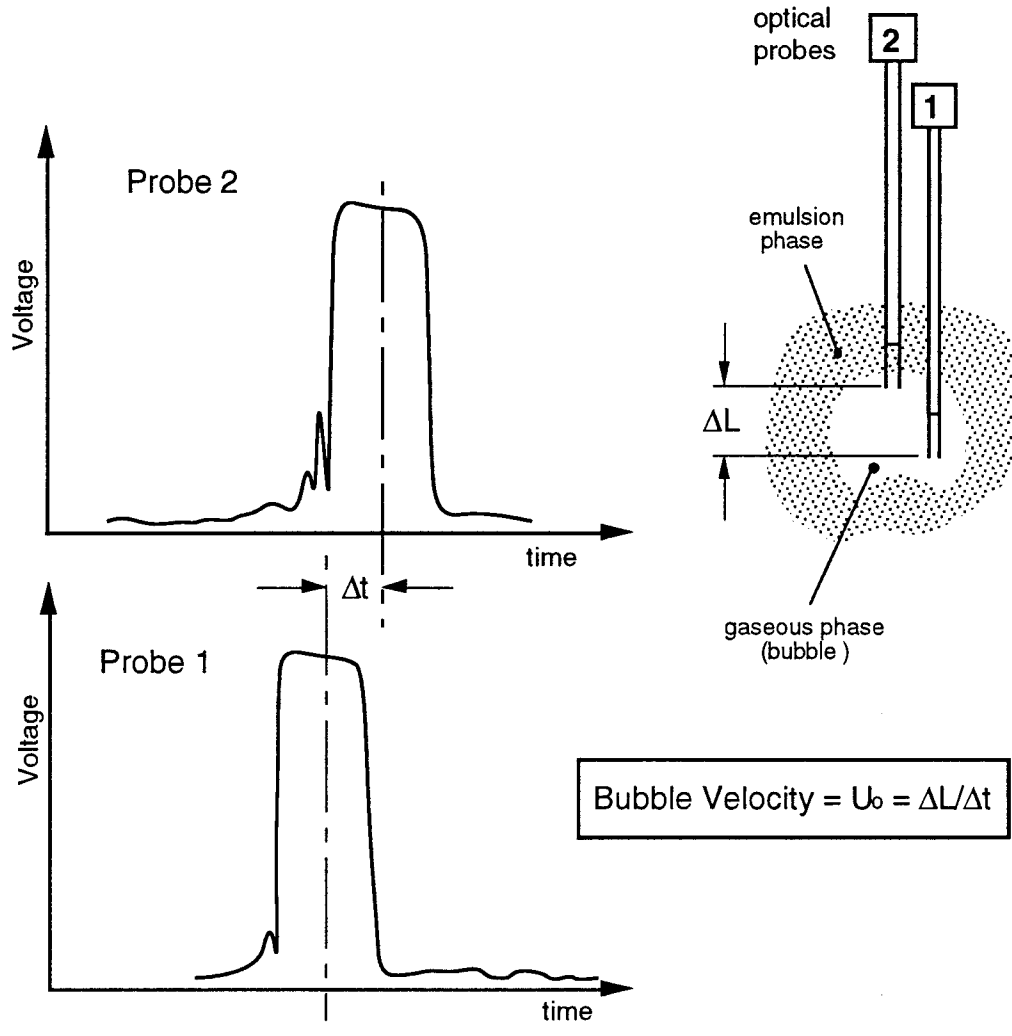

Figure 3-2: Use of Multiple Probes to Measure Bubble Rise Velocity

performance since the size of bubbles controls particle mixing and particle contacting of immersed surfaces, which are the main mechanisms of heat transfer from the hot bed to the working fluid. Bubble size also controls bubble rise velocity and the amount of particle elutriation from the top of the fluidized bed [8,6].

The inter-arrival times and pierced lengths can be presented as averages or distributions since there is generally more than one bubble

passing through the probe over its five-second sampling period at each probe location. However, there is only one value of the bubble frequency and bubble rise velocity for each probe location.

3.2 Experimental Cases

The hydrodynamics of a fluidized bed is dependent on factors such as particle size, superficial velocity, and the presence and arrangement of internal surfaces. The experiments carried out in this thesis examined the effect of each of these factors on the bed hydrodynamics. A brief description of the experimental cases is provided in Figure 3-3 and discussed below.

1) *Superficial Velocity:* Five values of superficial velocity were used in this study, 4.25, 5, 5.75, 6.4, 7.2 ft/s respectively. The packed bed height was 12 inches above the distributor, and three particles sizes were used. See Table 3-1 for a more complete description of the particles.

Table 3-1: Description of Particles Used in Experiments.

	1	2	3
Particle Material: Silica - Alumina			
Size Range (mm):	1.70 - 2.00	2.00 - 2.36	2.36 - 3.35
Mean Diameter (mm):	1.85	2.18	2.85
Density (lb/ft3):	168.5	168.5	168.5
Geldart Group:	D	D	D

2) *Particle Size:* The effects of three different particle sizes -- $1.70 \leq d_p \leq 2.00$ mm, $2.00 \leq d_p \leq 2.36$ mm, and $2.36 \leq d_p \leq 3.35$ mm -- were examined.

The superficial velocity was maintained at 5.75 ft/s, and the packed bed height was 12 inches. Also note that comparisons between particle sizes at different superficial velocities was possible.

3) *Internal Surfaces:* Four internal surface arrangements were used. The four geometries included a single cylinder at the horizontal bed center and 2 cylinders located at center to center distances of 3, 4, and 5 inches as shown in Figure 2-4. The superficial velocity was set to 5 ft/s, and the packed bed height used was 12 inches above the distributor. Particles were in the size range $1.70 \leq d_p \leq 2.00$ mm.

1) variation of superficial velocity

2) variation of particle size

Uo ≈ 4.25 ft/s Lm ≈ 12 inches 1.70 ≤ dp ≤ 2.00 mm no internal surfaces	***U o ≈ 5 ft/s*** Lm ≈ 12 inches 1.70 ≤ dp ≤ 2.00 mm no internal surfaces	***U o ≈ 5.75 ft/s*** Lm ≈ 12 inches **1.70 ≤ dp ≤ 2.00 mm** no internal surfaces
Uo ≈ 5.75 ft/s Lm ≈ 12 inches **2.00 ≤ dp ≤ 2.36 mm** no internal surfaces	***U o ≈ 6.4 ft/s*** Lm ≈ 12 inches 2.00 ≤ dp ≤ 2.36 mm no internal surfaces	***U o ≈ 7.2 ft/s*** Lm ≈ 12 inches 2.00 ≤ dp ≤ 2.36 mm no internal surfaces
Uo ≈ 5.75 ft/s Lm ≈ 12 inches **2.36 ≤ dp ≤ 3.35 mm** no internal surfaces	***U o ≈ 6.4 ft/s*** Lm ≈ 12 inches 2.36 ≤ dp ≤ 3.35 mm no internal surfaces	***U o ≈ 7.2 ft/s*** Lm ≈ 12 inches 2.36 ≤ dp ≤ 3.35 mm no internal surfaces

3) variation of internal surfaces

Uo ≈ 5 ft/s Lm ≈ 12 inches 1.70 ≤ dp ≤ 2.00 mm **1 cylinder**	Uo ≈ 5 ft/s Lm ≈ 12 inches 1.70 ≤ dp ≤ 2.00 mm **2 cylinders : L/D = 1.5**	Uo ≈ 5 ft/s Lm ≈ 12 inches 1.70 ≤ dp ≤ 2.00 mm **2 cylinders : L/D = 2**
	Uo ≈ 5 ft/s Lm ≈ 12 inches 1.70 ≤ dp ≤ 2.00 mm **2 cylinders : L/D = 2.5**	

Figure 3-3: Description of Experimental Cases.

3.3 Testing and Data Collection Procedure

The major steps in the testing procedure were as follows:

1) The optical probes were calibrated to a maximum voltage of 3 volts for the gas phase so that the level discriminator would chop both probe signals at about the same reference voltage.

2) The case type to be tested was selected, and the test section was set-up accordingly. For example, if the case was the particle size study then the proper sized particles were put into the bed to a packed-bed height of 12 inches.

3) The probes were positioned at location one, which was on the right-hand-side of the bed when viewed from the front (refer to Figure 2-5).

4) The air supply system was turned on and allowed to reach a steady-state temperature which normally fell within the range of $110 \leq T \leq 120$ °F.

5) The superficial velocity was set by adjusting the motor speed to a predetermined pressure drop across the orifice corresponding to a certain velocity. For instance, a pressure drop of seven inches of water across the orifice provided a velocity of approximately 5 ft/s.

6) The IBM XT data acquisition program was started so that the board could be set to accept incoming data at the digital I/O port.

7) The flow parameters were entered into the data acquisition program.

8) After all systems were ready, the return key was pressed and 5 seconds of data were taken at 500 samples/second.

9) The probes were then repositioned at position two without touching any of the flow controls. The probe holes were immediately sealed after the removal of the probe to prevent any particle losses.

10) Steps 6 through 8 were repeated until data were obtained at all probe locations.

11) The entire procedure was repeated for each experimental case. For example, in the superficial velocity study the procedure was repeated three times -- once for velocity.

3.4 Data Reduction

A program was specifically designed to process and reduce the data stored by the IBM XT. The program was written in MacFortran for the Macintosh computer. The Macintosh was used because it allowed windows and menus to help in viewing and processing of the probe data. The data reduction FORTRAN code was named "Bubbles."

Bubbles opened the user specified data file that was stored by the IBM XT and translated to Macintosh format. The program immediately graphed, to the screen, the data from both probes at a single probe-location. The user could thus freely examine the waveforms produced by both probes as seen in Figure 3-4a.

The viewing was done for two reasons. First, the graphing along with the interface allowed the user to shift the upper probe signal to match the lower probe signal as seen in Figure 3-4b. The resultant shift or bubble time delay between probes was used to calculate the bubble velocity for that probe-location by dividing the distance between the probes by this shift.

Second, the data had noise in it that had to be removed without loss of important pulse-width information. The noise was of two types -- it was either a narrow attenuation, a drop from a high to a low, or it was a brief rise from a

low to a high. The majority of this noise was caused by the optical probe's LED 1 kHz carrier frequency which would briefly go above and below the discriminator reference voltage as the signal reached that voltage (see Figure 3-5). An additional source of this noise occurred when particles were displaced into the bubble when the bubble hit the probe. If the particles fell between the probe tips, an brief attenuation would result. Also, bubbles could nucleate at the probe tips and cause a brief transmission across the gap thereby producing a narrow spike or pulse-width. The program used provided filtering of a majority of these spikes or drops.

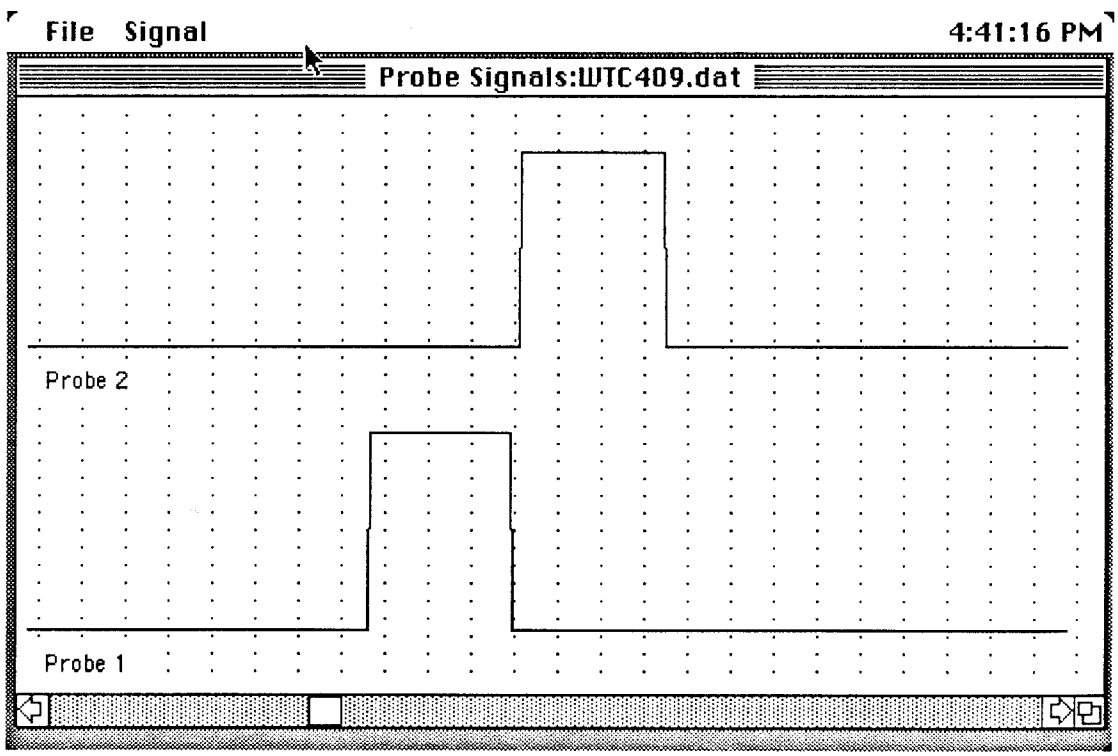

Figure 3-4a: Portion of Probe Signals as Displayed by Data Reduction Program.

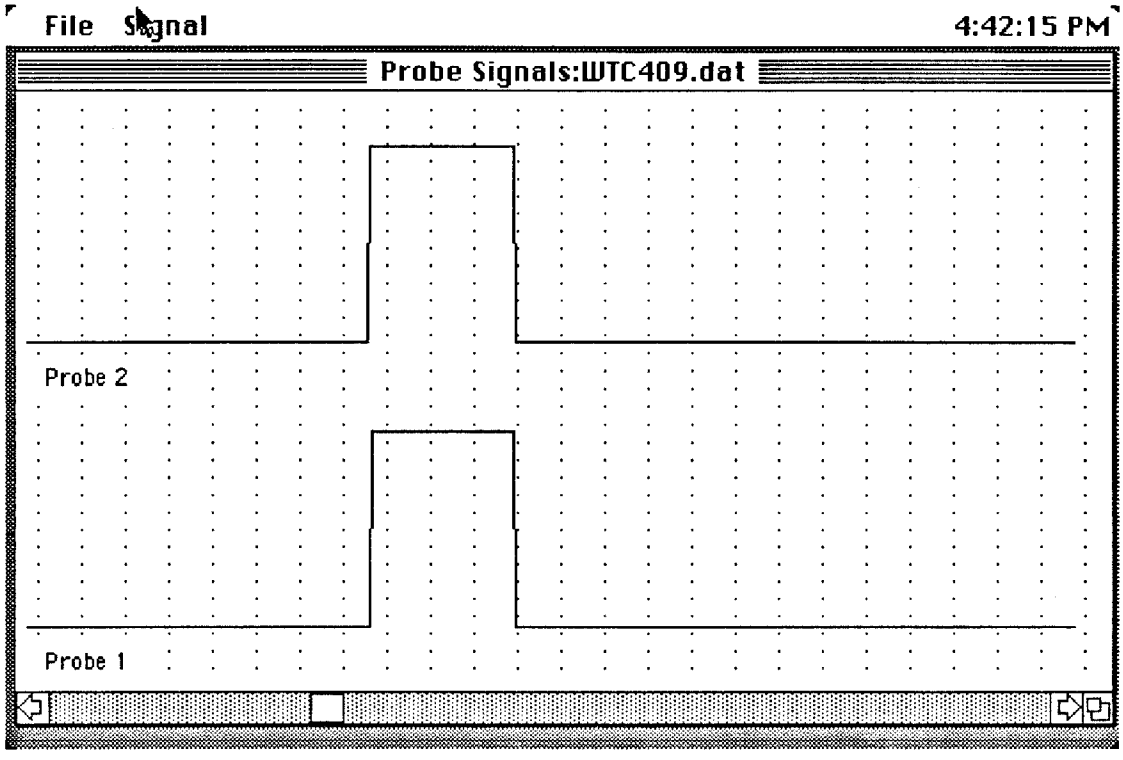

Figure 3-4b: Example of Upper Probe Signal Shifting for Determining the Bubble Time Delay Between Probes.

After the data were shifted and filtered, the program calculated the bubble rise velocity, frequency, inter-arrival time distribution, average inter-arrival time, pierced length distribution, average pierced length, superficial velocity, and minimum fluidization velocity.

For more information on the data reduction program see Appendix E.

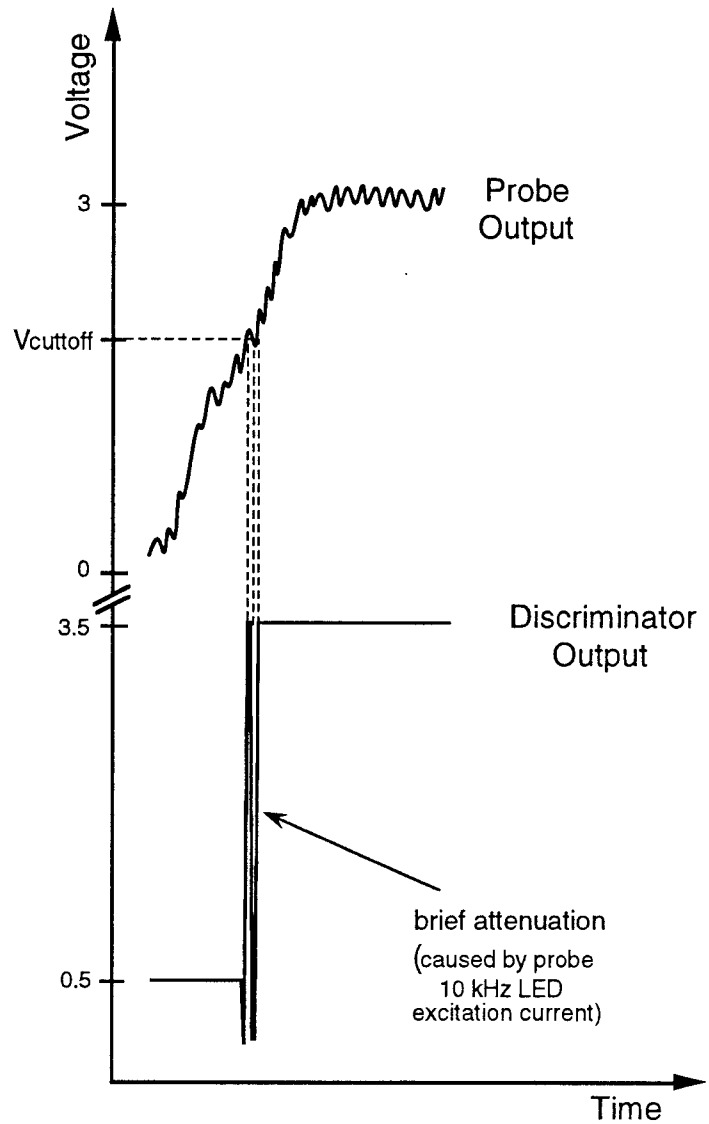

Figure 3-5: Example of Signal Attenuation due to 1 kHz Carrier Frequency.

4. RESULTS AND DISCUSSION

The results of this research involve examining the effects of superficial velocity, particle size, and presence of immersed surfaces on the four bubble properties -- bubble frequency, inter-arrival time, bubble rise velocity, and bubble pierced lengths. The goal of these results is to observe any trends that the bubble properties exhibit with varying fluidized bed conditions, such as superficial velocity, particle size and internal surface geometry, so that fluidized bed signatures may be ascertained. In order to establish trends many of the results are presented with a simple linear regression fit.

In the following sections bubble properties will be discussed individually for each study starting with the bubble frequency followed by the average bubble inter-arrival time, bubble rise velocity, and average bubble pierced length. The averaged terms emanate from the fact that more than one bubble passes through each probe over its five-second sampling period. Therefore, these values are averaged so that a single value represents each probe-location. Also, note that the experimental conditions -- number of immersed surfaces, bed height, particle size and superficial velocity -- are listed in a box with each graph or figure. Sample bubble property data is included in Appendix A.

The results of this research are presented and discussed in the following four sections. The findings of the superficial velocity study are presented in Section 4.1. The study of particle size follows in Section 4.2. Section 4.3 is dedicated to examining a combination of the superficial velocity and the particle size studies. For the plots in Section 4.3 all of the empty bed data

were used. The effects due to the presence of immersed surfaces is presented and discussed in Section 4.4. Finally, an analysis of the uncertainty involved with the results is included in Appendix F.

4.1 Effect of Superficial Velocity

4.1.1 Superficial Velocity and Bubble Frequency

The bubble frequency versus lateral distance across the bed for three different superficial velocities at one particle size is presented in Figure 4-1. The upper plot is included to show that each of the three velocities is represented by a linear regression fit similar to that of this plot. From Figure 4-1 it is apparent that bubble frequency increases with superficial velocity. The slightly increasing slope of the line could be the result of a minor channelling area at the right side of the bed. Figure 4-2 displays the average bubble frequency versus the superficial velocity for all the particle sizes used in this study ($1.70 \leq d_p \leq 2.00$ mm, $2.00 \leq d_p \leq 2.36$ mm, and $2.36 \leq d_p \leq 3.35$ mm). Each point is the average of the bubble frequencies across the bed for that case (i.e. average of all probe-location values). For example, the data in Figure 4-1 represents three points on this graph -- one for each velocity. If further clarity is needed please refer to the description of experimental cases provided in Figure 3-3. From this plot a clear trend is present -- the bubble frequency increases with increasing superficial velocity.

4.1.2 Superficial Velocity and Average Inter-Arrival Time

The average inter-arrival time was calculated by averaging all inter-arrival times as calculated by using equation 3.2 for each probe-location. The

average inter-arrival time versus lateral distance across the bed for three different superficial velocities at one particle size is shown in Figure 4-3. From this graph the average inter-arrival time appears to decrease with superficial velocity. Once again the slightly decreasing slope of the lines

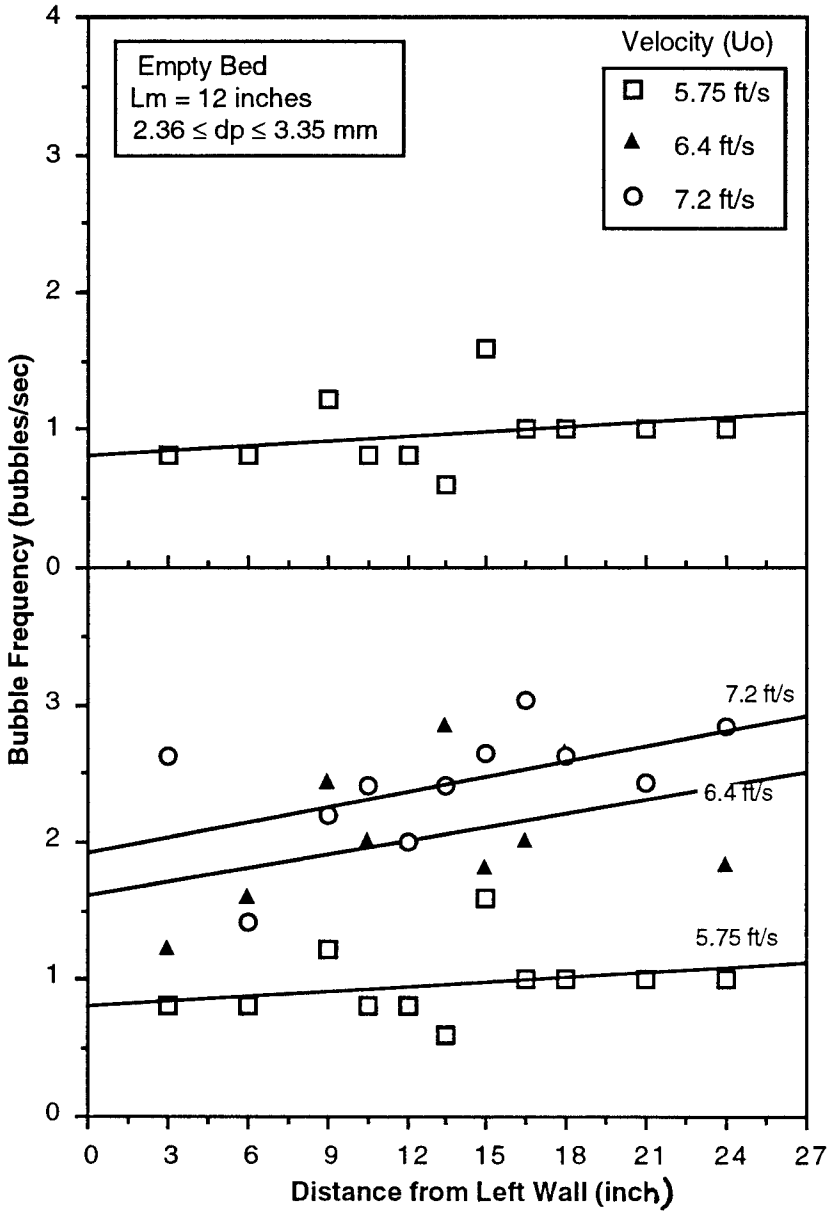

Figure 4-1: Bubble Frequency vs. Lateral Distance Across Bed for Three Superficial Velocities at One Particle Size.

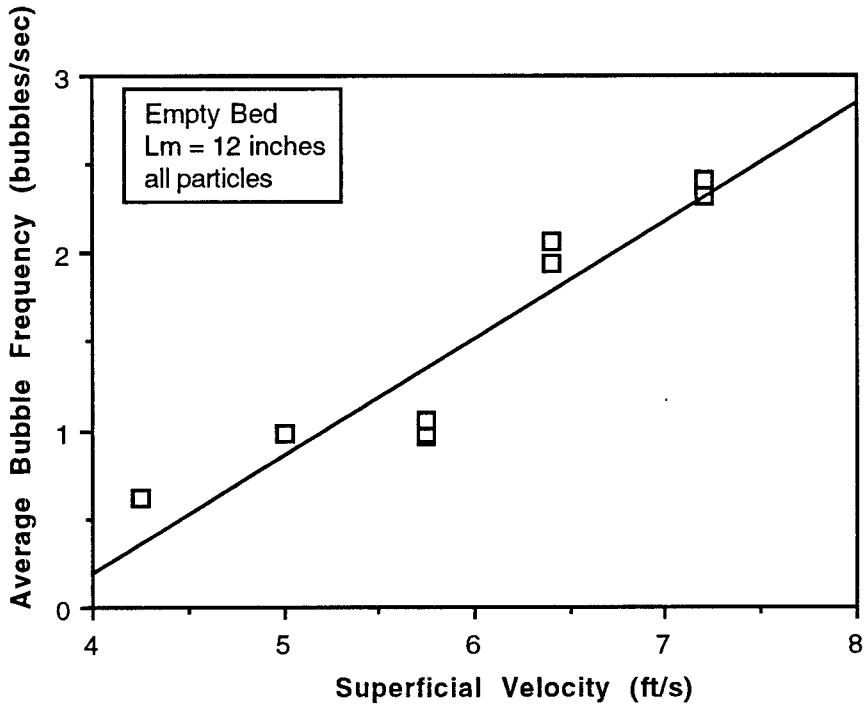

Figure 4-2: Average Bubble Frequency vs. Superficial Velocity.

could be the result of a minor channelling area at the right side. Figure 4-4 displays the averaged inter-arrival times versus the superficial velocity for all the particle sizes used in this study ($1.70 \leq dp \leq 2.00$ mm, $2.00 \leq dp \leq 2.36$ mm, and $2.36 \leq dp \leq 3.35$ mm). From this plot an obvious trend exists -- the average inter-arrival time decreases with increasing superficial velocity. This follows from the bubble frequency trend discussed above. If the frequency of bubble occurrence is increasing then the delay time between successive bubbles should be decreasing.

4.1.3 Superficial Velocity and Bubble Rise Velocity

The bubble rise velocity versus the lateral distance across the bed is

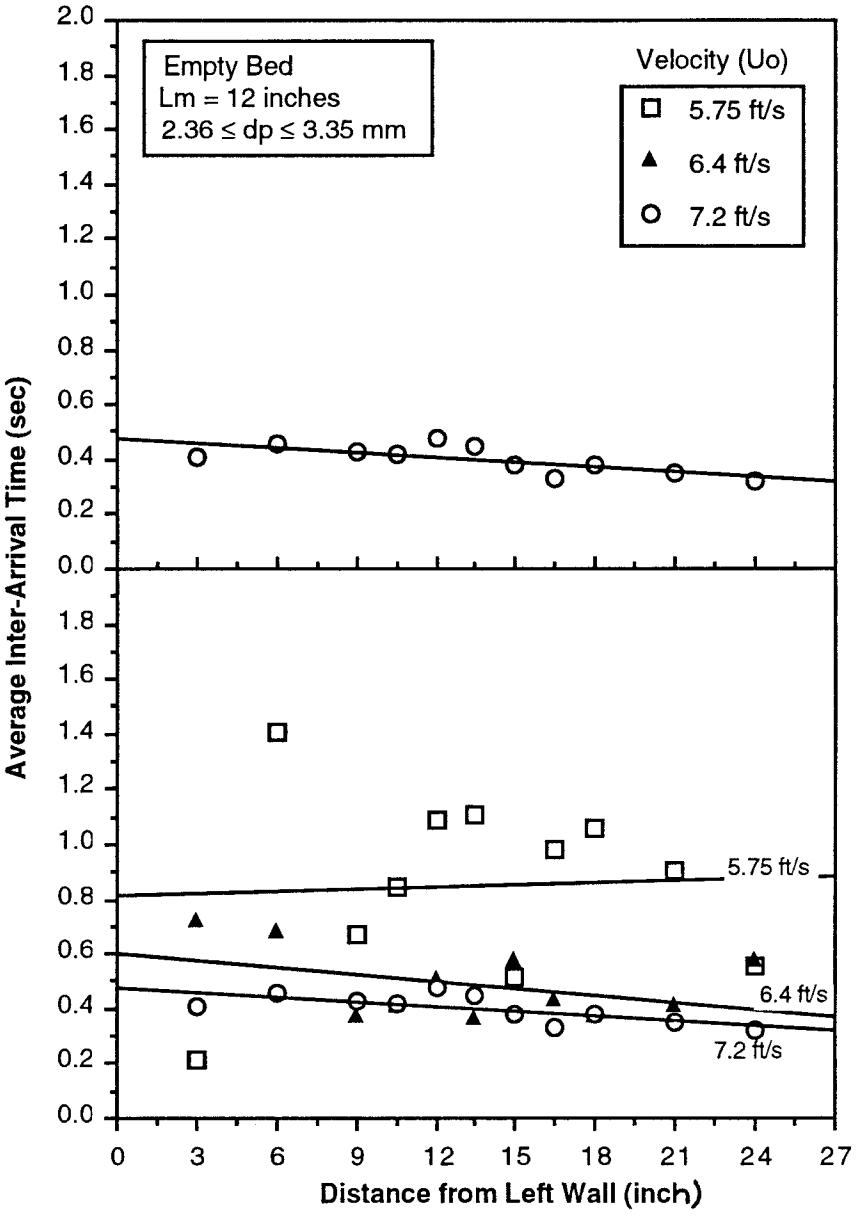

Figure 4-3: Average Inter-Arrival Time vs. Lateral Distance Across Bed for Three Superficial Velocities at One Particle Size.

depicted in Figure 4-5. This plot has only one line since points lie very close to one another and plotting separate lines does not indicate any preferential inclinations. A linear regression of all the points shows that the bubble rise velocity does not change but appears to stay at approximately the same value

across the bed. Perhaps a characteristic value is representative of the bubble rise velocity at this probe height.

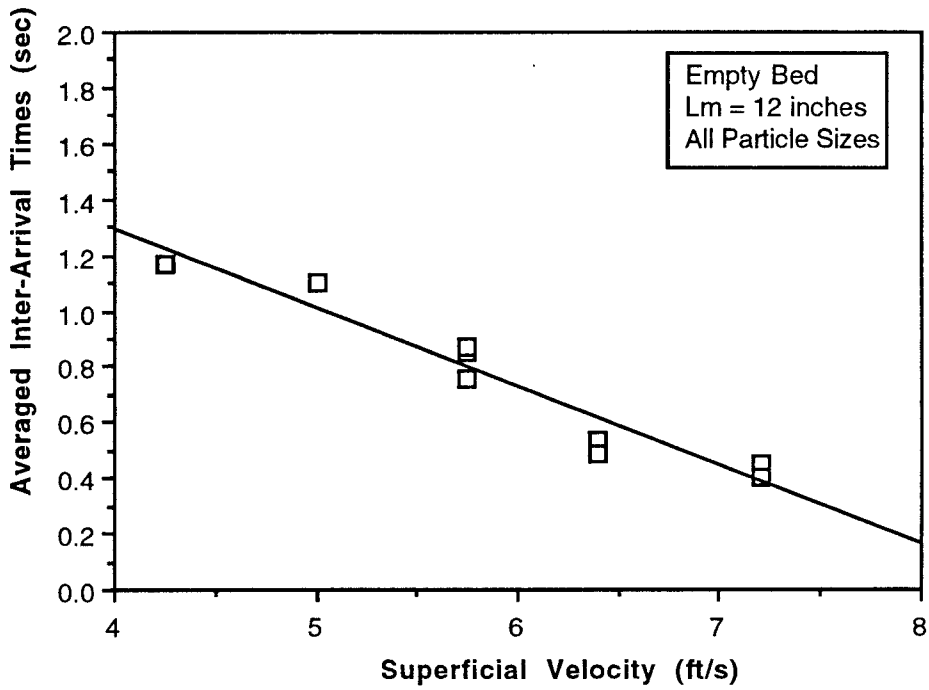

Figure 4-4: Averaged Inter-Arrival Time vs. Superficial Velocity.

4.1.4 Superficial Velocity and Average Pierced Length

The average bubble pierced length versus the lateral distance across the bed is presented in Figure 4-6. Once again, this plot has only one regression fit or all data points since the points lie very close to one another and plotting separate regression lines does not reveal any patterns. The linear regression of all the points shows that the averaged pierced length does not change with superficial velocity but appears to stay at approximately the same value across the bed. Although there is scattering about the linear regression fit, a characteristic value might be representative of the bubble pierced length at

this probe height.

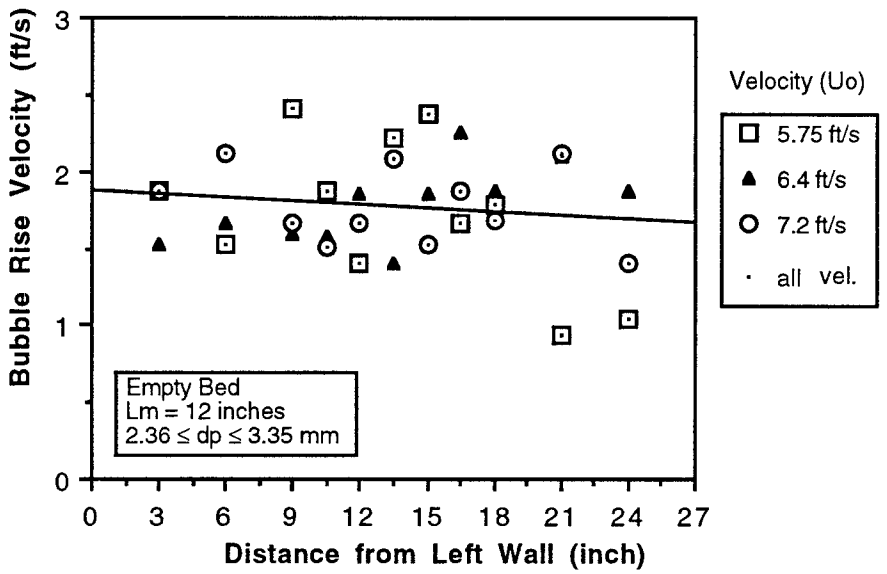

Figure 4-5: Bubble Rise Velocity vs. Lateral Distance Across Bed for Three Superficial Velocities at One Particle Size.

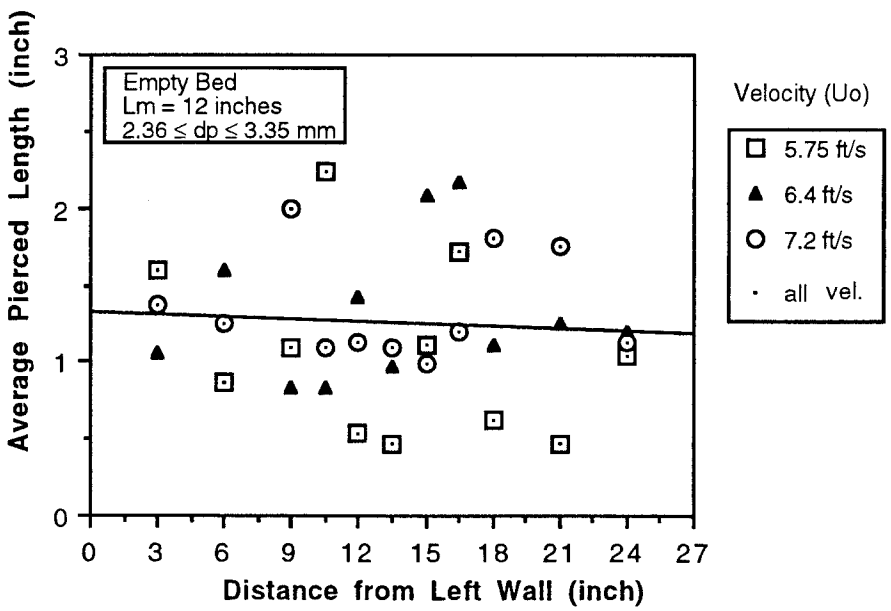

Figure 4-6: Bubble Pierced Length vs. Lateral Distance Across Bed for Three Superficial Velocities at One Particle Size

4.2 Effect of Particle Size

The bubble frequency, average inter-arrival time, bubble rise velocity, and average pierced length versus lateral distance across the bed for three separate particle sizes at one superficial velocity are presented in Figures 4-7, 4-8, 4-9 and 4-10 respectively. These plots contains only one linear regression fit each since no trends of any of the bubble properties with particle size was evident. That is, from this data the bubble frequency, average inter-arrival time, bubble rise velocity, and pierced length do not appear to be functions of the particle size. The four bubble properties appear to be approximately constant at superficial velocity, probe height and other bed conditions, regardless of the particle size.

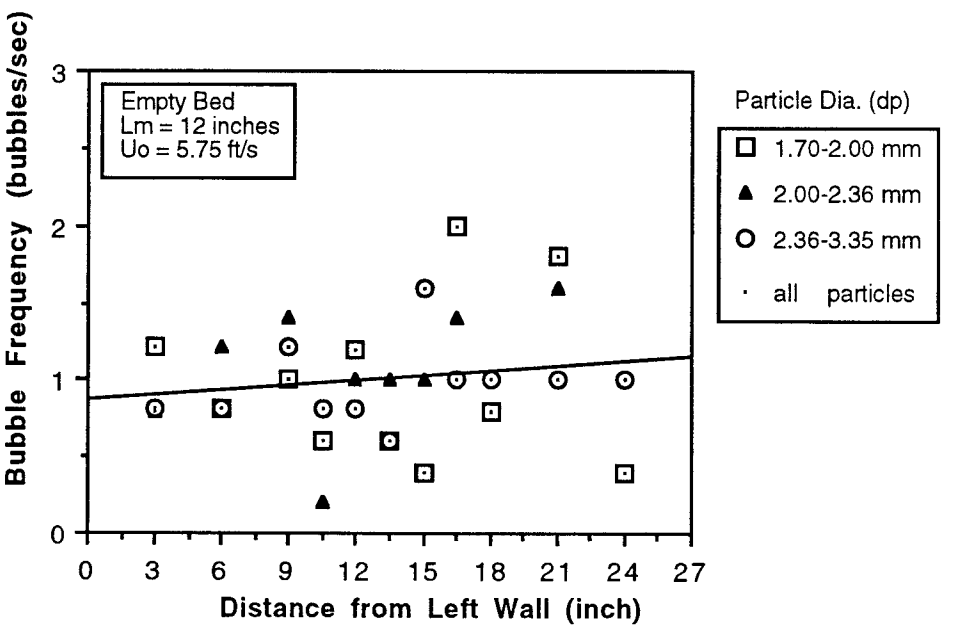

Figure 4-7: Bubble Frequency vs. Lateral Distance Across Bed for Three Particle Sizes at One Superficial Velocity.

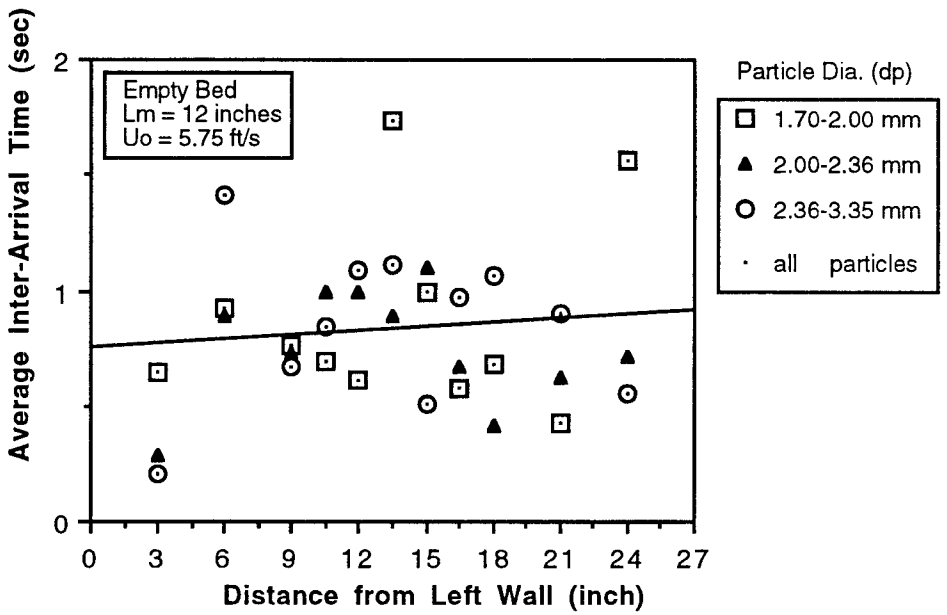

Figure 4-8: Average Inter-Arrival Time vs. Lateral Distance Across Bed for Three Particle Sizes at One Superficial Velocity.

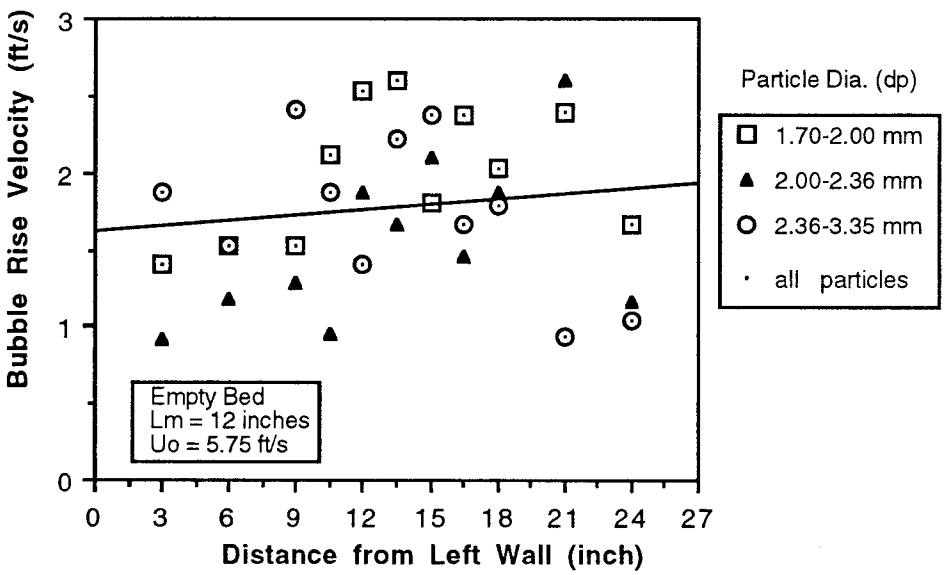

Figure 4-9: Bubble Rise Velocity vs. Lateral Distance Across Bed for Three Particle Sizes at One Superficial Velocity.

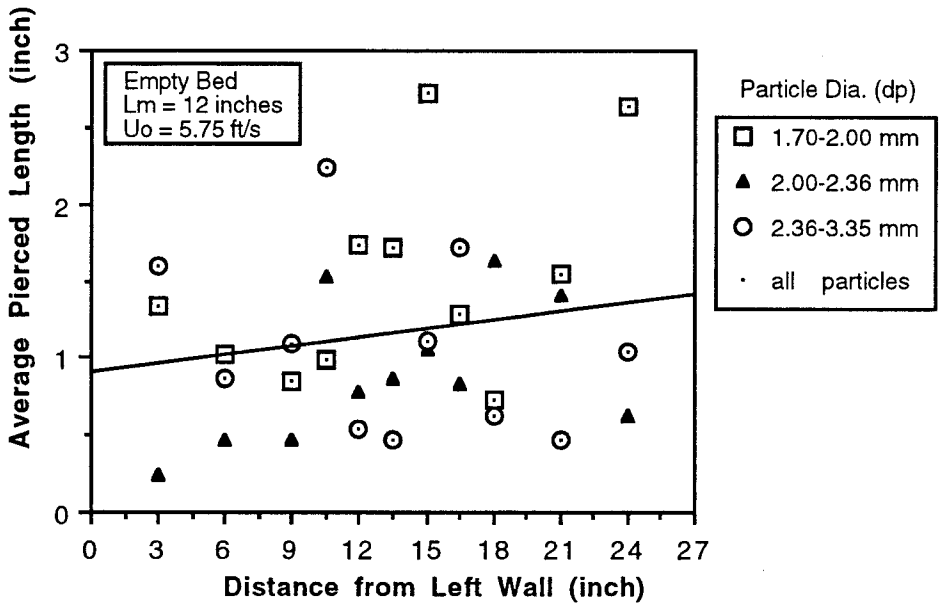

Figure 4-10: Bubble Pierced Length vs. Lateral Distance Across Bed for Three Particle Sizes at One Superficial Velocity.

4.3 Combination of Superficial Velocity and Particle Size

The bubble frequency versus the non-dimensional velocity, defined as the superficial velocity divided by the theoretical minimum fluidization velocity of the particle size used, is shown is Figure 4-11. Note that each point on this graph represents a single probe-location. Also, see Figure B-2 in Appendix B for a comparison between the theoretical and experimentally observed minimum fluidization velocities of the particles used in this research. As found in Section 4.1 an increasing trend exists between bubble frequency and the superficial velocity. As seen in Figure 4-11 the rate of increase of this trend appears to be dependent on particle size. That is, the larger the particle size the steeper the inclination. An explanation of the variation of trend steepness with particle size follows.

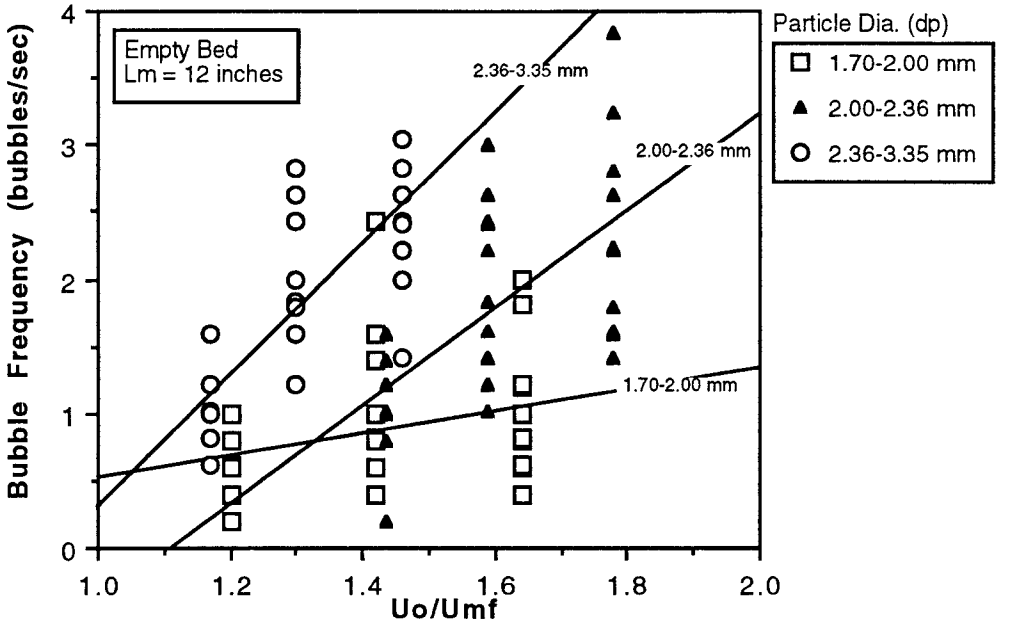

Figure 4-11: Bubble Frequency vs. Non-Dimensional Velocity for Three Particles Sizes.

As discussed previously, the larger the particle size the higher the minimum fluidization velocity (refer to Figures 1-14 or B-2 for reference). It is well known [10] and was experimentally observed in this research that smaller particles progress gradually into the bubbling regime while the larger particles move very quickly into this flow regime after reaching minimum fluidization. The reason is that a fluidized bed must transmit the same amount of gas through the bed regardless of the particle size used. In other words, despite the particle size the bubbling frequency should be approximately equal, assuming a characteristic bubble size, at a set superficial velocity as was concluded in Section 4.2. This can also be verified by examining Figure 4-11. Note that the highest velocity used for the 1.70 - 2.00 mm is 5.75 ft/s, and it is the lowest superficial velocity used for the remaining two particle sizes. From the plot these values lie near the same bubbling frequency. The same is true

for the remaining data at the two larger particle sizes since they were recorded at equal superficial velocities of 6.4 and 7.2 ft/s. Thus, since the larger particles begin bubbling at higher velocities there bubbling frequency is arrived at quicker on the non-dimensional velocity scale than the smaller particles. This accounts for the variation of steepness with the particle size.

The bubble rise velocity versus the nondimensional velocity is presented in Figure 4-12. Although the slope of the regression fit is slightly increasing, no trend of bubble rise velocity with non-dimensional velocity appears to exist from this data due to the large amount of scatter. As discussed earlier, perhaps a characteristic bubble rise velocity exists at this probe height.

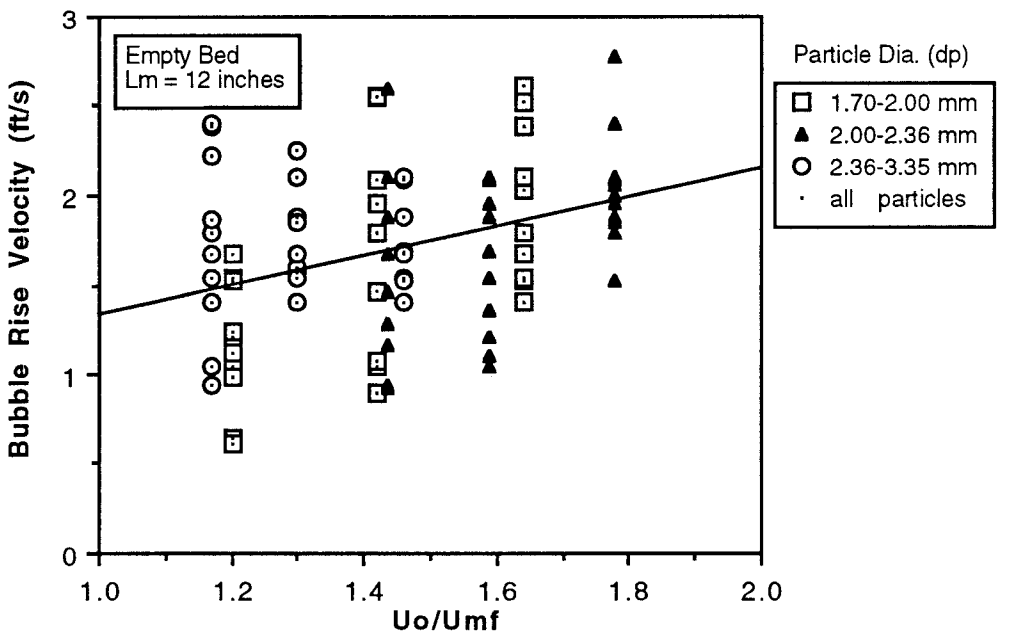

Figure 4-12: Bubble Rise Velocity vs. Non-Dimensional Velocity for Three Particle Sizes.

A representation of the average pierced length versus the non-dimensional velocity is provided in Figure 4-13. Given the amount of

scattering there does not appear to be any distinct trend between the average bubble pierced length and the non-dimensional velocity. As mentioned earlier, a characteristic value of bubble pierced length might be typical at this probe height.

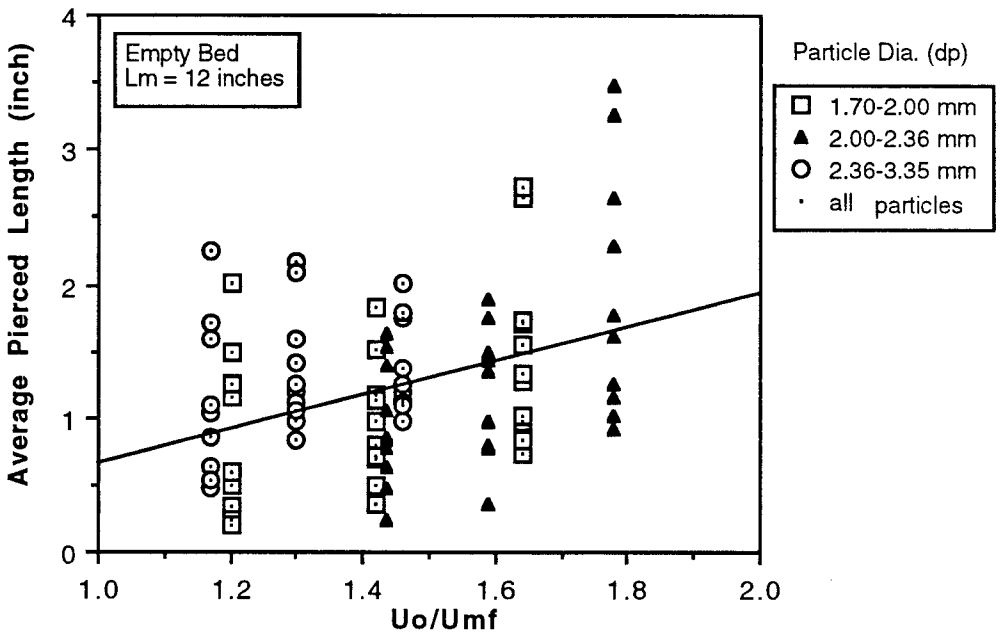

Figure 4-13: Bubble Pierced Length vs. Non-Dimensional Velocity for Three Particle Sizes.

4.4 Effect of Immersed Surfaces

4.4.1 Immersed Surfaces and Bubble Frequency

The bubble frequency versus lateral distance across the bed for four different internal surface arrangements at one particle size and superficial velocity presented in Figure 4-14 and 4-15. Note that, if the cylinders were positioned directly below a probe-location, an interpolating spline was used to connect the values recorded at each location. The points were otherwise left unconnected.

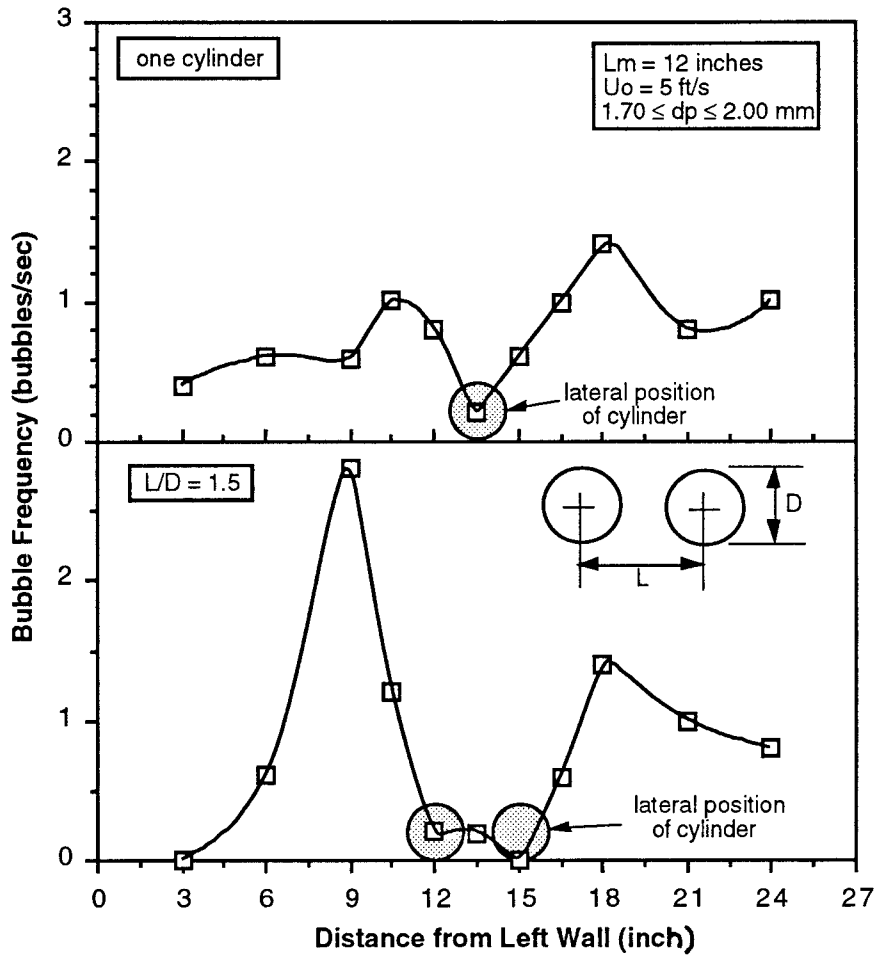

Figure 4-14: Bubble Frequency vs. Lateral Distance Across Bed for Two Internal Surface Arrangements

The effect of a single cylinder on the bubble frequency is readily visible in Figure 4-14. The frequency of bubble occurrence drops nearly to zero at the probe location nearest the cylinder and rises to high values for the probe-locations on either side. The defluidized cap on the cylinder and the physical presence of the cylinder itself are the main reasons no bubbles pass through the bed in the area above the surface.

When two cylinders are placed in the bed at a fairly close spacing (L/D =

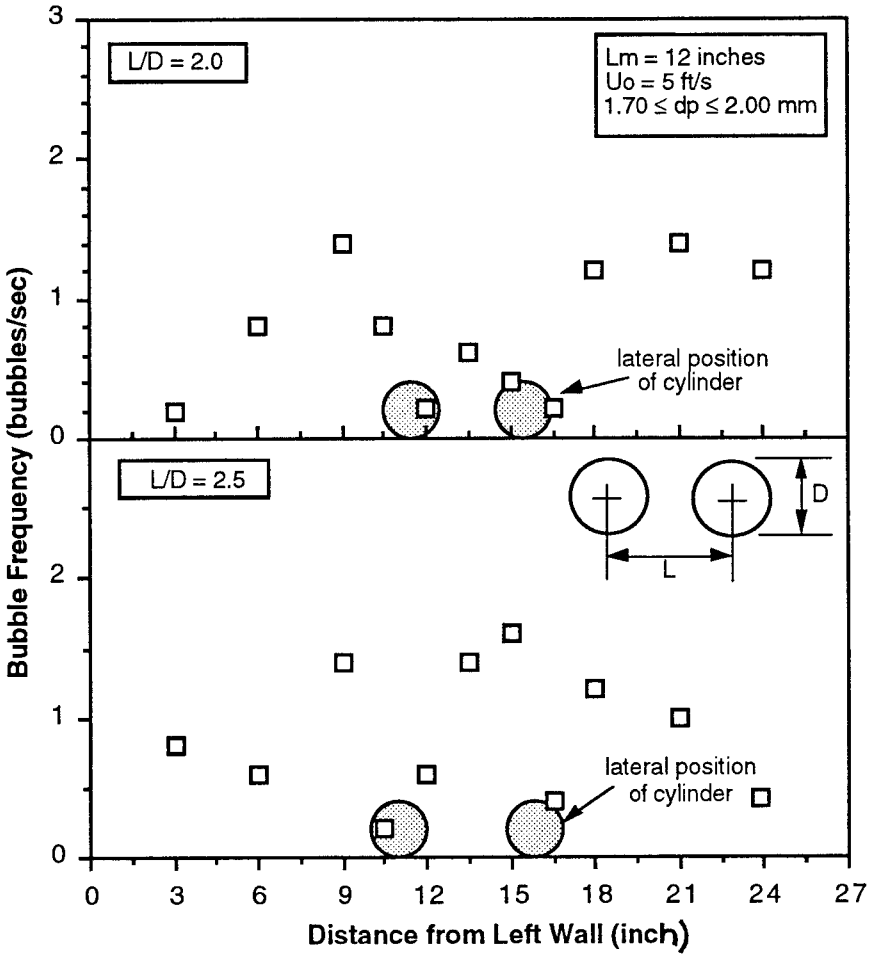

Figure 4-15: Bubble Frequency vs. Lateral Distance Across Bed for Two Internal Surface Arrangements

1.5), the frequency of bubble occurrence drops nearly to zero at the probe-locations between the surfaces. This decrease in bubble frequency is most likely due to a bridge of defluidized particles that build-up between the two tubes. Also apparent from Figure 4-14 is that a channelling area with a circulation cell seem to have developed on the left side of the bed for this geometry. The circulation cell is at the extreme left where the bubble frequency is zero.

As the cylinders are separated to a spacing of L/D = 2, the bridge of

defluidized particles breaks down and bubbles pass between the surfaces more readily than the previous spacing of L/D = 1.5. However, it is apparent from the bubble frequency plot that the flow of bubbles is still restricted, and the channelling and circulation area persist as before.

Lastly, when the surfaces are separated to a spacing of L/D = 2.5, the bubble frequency returns to normal if, not higher-than-normal, value at the probe-locations in between the two tubes. Therefore, at the spacing of L/D = 2.5 the bubble frequency appears to be almost the same as the graph of one immersed cylinder, high bubble frequency on either side with the frequency approaching zero at the cylinder. Furthermore, with this arrangement the channelling area and circulation cell have dispersed.

Figure 4-16 portrays the bubble frequency versus the internal surface arrangements for the probe-location number 6. Note that probe-location 6 is at the lateral center of the bed, and the internal surfaces are symmetrically mounted about this point. This graph implies that as the cylinders are moved apart the bubble frequency between the cylinders (probe-location 6) returns to that of an empty bed.

4.4.2 Immersed Surfaces and Average Inter-Arrival Time

The average inter-arrival time versus the arrangement of internal surfaces at probe-location number 6 is shown in Figure 4-17. This plot suggests that the inter-arrival time for the closer spacings of the surfaces approaches large values. Thus, very few bubbles, if any, are passing in-between the surfaces. On the other hand, as the cylinders are moved farther apart, the inter-arrival time approaches the same value as that of an empty bed.

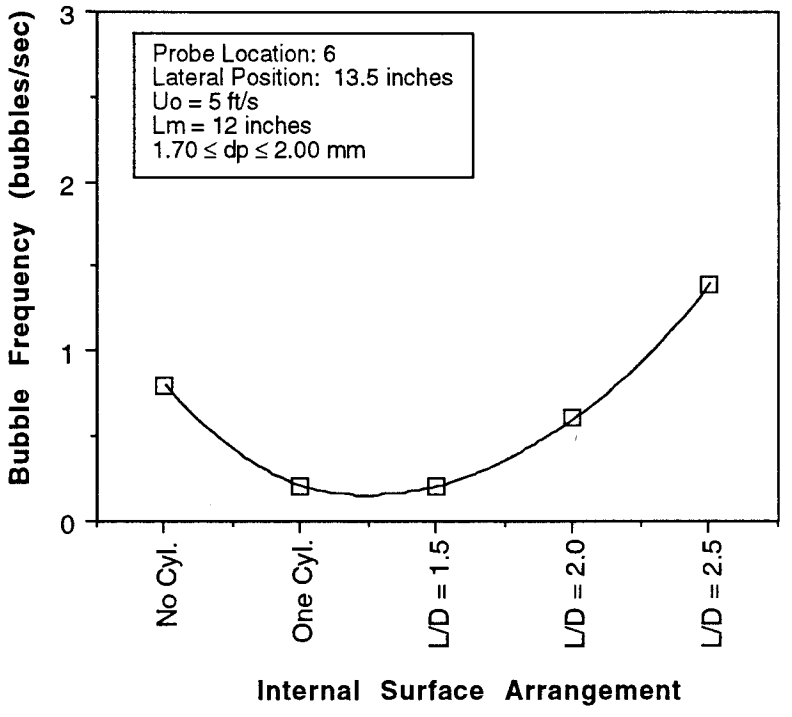

Figure 4-16: Bubble Frequency vs. Bed Geometry.

4.4.3 Immersed Surfaces and Bubble Rise Velocity

Figure 4-18 displays the variation of the bubble rise velocity with the internal surface arrangements. The bubbles that were able to pass through the small gap at the surface arrangement of L/D = 1.5 appear to have had a high rise velocity. This increased rise velocity could have been caused by the bubble having to shrink in size to pass between the tubes causing a squirting effect. When the surfaces were moved to the next spacing, with L/D = 2, the effect diminished. Once again, as the cylinders were separated by larger distances the bubble rise velocity returned to that of any empty bed.

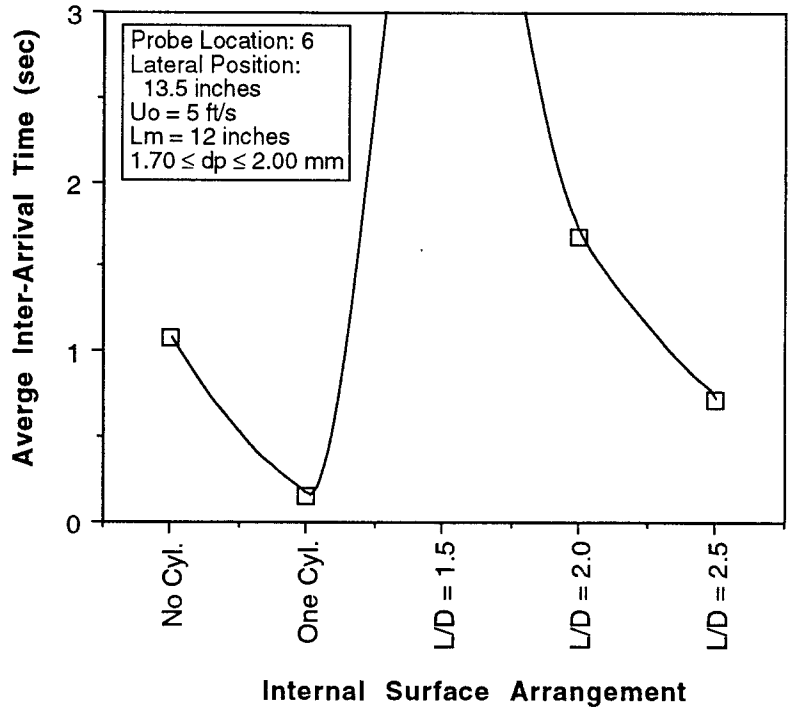

Figure 4-17: Average Inter-Arrival Time vs. Bed Geometry.

4.4.4 Immersed Surfaces and Average Pierced Length

Figure 4-19 portrays the average pierced length as a function of the internal surface arrangement. The pierced length does not appear to be a strong function of internal surface arrangement.

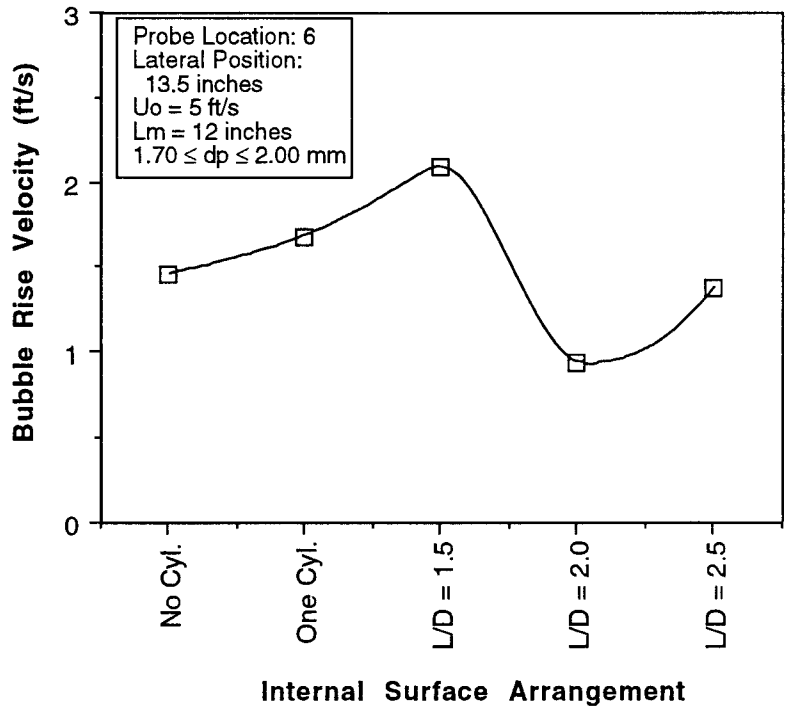

Figure 4-18: Bubble Rise Velocity vs. Bed Geometry.

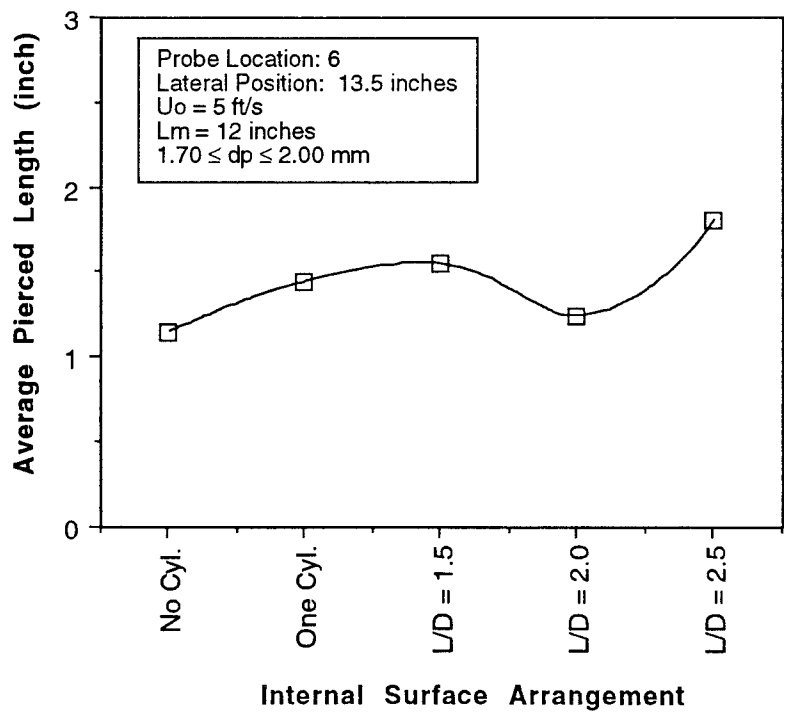

Figure 4-19: Bubble Pierced Length vs. Bed Geometry.

5. CONCLUSIONS AND RECOMMENDATIONS

5.1 Conclusions

1) The bubble frequency is an increasing function of the superficial velocity. This is reasonable since as the flow rate supplied to the bed is increased the extra or added gas is carried through the bed as bubbles. Likewise, the average inter-arrival time decreases with increasing superficial velocity. This follows from the increasing bubble frequency with superficial velocity since as more bubbles pass through the bed the delay time between successive bubbles will decrease.

2) A single characteristic bubble rise velocity and average pierced length appear to exist at the probe height used with this two-dimensional fluidized-bed apparatus.

3) Bubble frequency does not appear to be a function of particle size.

4) The frequency of bubble occurrence drops nearly to zero at the probe location nearest a single cylinder immersed in a fluidized bed and rises to high values on either side.

5) At the spacing, L/D = 2.5, for two immersed cylinders in a fluidized bed the bubble frequency near the tubes behaves similarly to that for a single immersed cylinder -- high bubble frequency on either side with the frequency

approaching zero at the cylinder.

6) As the immersed surfaces are moved farther apart bubble properties approach those recorded with an empty bed.

7) The bed appeared to have a minor channelling area on the right side. This was noticeable in most of the empty bed frequency plots. Furthermore, visual observation of the bed showed that bubbles first formed on the right side which may indicate a preferential flow channel.

5.2 Recommendations

1) The distance between probe tips caused many problems with the bubble rise velocity measurements. This distance needs to be reduced significantly. The distance caused errors in the bubble rise velocity measurements which translated into errors for the pierced lengths. Similar problems were experienced by Matsuura and Fan [11]. The bubble detected by probe 2 may not be the same as that detected by probe 1. For example, the bubble may have been deflected after passing through probe 1. The deflected bubble may pass through probe 2 at a different location or it may not pass through probe 2 at all. Further, coalescence or break-up may occur between probes. These types of occurrences cause matching problems with the data reduction sequence of the research. Needless to say, the closer the probes the less likely these problems will occur.

2) The distributor plate has a strong influence on the bubble properties since

all bubbles form at the distributor plate. A study of various distributor orifice sizes may be worthwhile.

3) All of the bubble properties may be a function of probe height as discussed by Yasui and Johanson [17]. They found that bubble frequency decreased with probe height while the bubble size increased due to coalescence. The characteristic bubble rise velocity and average pierced length discussed earlier may only be valid at the probe locations used in this research. Thus, probe height may be an area of more interest.

4) Longer data sampling periods might produce more uniform results than those obtained during this research.

BIBLIOGRAPHY

1 A.S.M.E., Fluid Meters, Their Theory and Application, 6th Ed., edited by Bean, H.S., United Engineering Center, NY, 1971.

2 Beckwith, Buck, and Marangoni, *Mechanical Measurements,* 3rd Ed., Addison-Wesley Publishing Co., Massachusetts, 1982.

3 Cheremisinoff, N.P. and Cheremisinoff, P.N., *Hydrodynamics of Gas-Solids Fluidization*, Gulf Publishing Co., Houston, 1984.

4 Chung, T. and Welty, J.R., "Tube Array Heat Transfer in Fluidized Beds: A Study of Particle Size Effects," *A.I.Ch.E. Journal*, Vol 35, No. 7, 1989, pp 1170-1176.

5 Davidson, J.F. and Harrison, D., *Fluidized Particles*, Cambridge University Press, 1963.

6 Geldart, D., "The Gas Fluidization of Large Particles," *The Chemical Engineering Journal*, Vol 3., 1972, pp. 211-231.

7 Geldart, D, in *Fluidization Engineering*, 2nd Ed.,by Kunii, D. and Levenspiel, O., Butterworth-Heinemann, Boston, 1991.

8 Goshayeshi, A., "Experimental Studies of Heat Transfer with an Array of Horizontal Tubes Immersed in a High-Temperature Fluidized Bed," Ph.D. Thesis, Dept. of Mech. Engr., Oregon State University, 1989.

9 Horio, M. and Nonaka, A., "A Generalized Bubble Diameter Correlation for Gas-Solid Fluidized Beds," *A.I.Ch.E. Journal*, Vol 33, No. 11, 1987, pp 1865-1872.

10 Kunii, D. and Levenspiel, O., *Fluidization Engineering*, 2nd Ed.,Butterworth-Heinemann, Boston, 1991.

11 Matsuura, A. and Fan, L., "Distribution of Bubble Properties in a Gas-Liquid-Solid Fluidized Bed," *A.I.Ch.E. Journal*, Vol 30, No. 6, 1984, pp 894-903.

12 Patterson, W.C. and Griffin, R., *Fluidized-Bed Energy Technology: Coming to a Boil*, Inform, NY, 1978.

13 Rooney, N.M. and Harrison, D. in *Fluidization Technology*, edited by D.L. Keairns, Hemisphere Publishing Corp., Vol 2., 1976, p 3.

14 Rowe, P.N. and Masson, H., "Fluidized Bed Bubbles Observed Simultaneously by Probe and by X-rays," *Chemical Engineering Science*, Vol. 35, 1980, pp 1443-1447.

15 Rowe, P.N. in "*Fluidized Particles*," by J.F. Davidson and D. Harrison, Cambridge University Press, 1963.

16 Werther, J. and Molerus, O., "The Local Structure of Gas Fluidized Beds -- II. The Spatial Distribution of Bubbles," *Int. Journal Multiphase Flow*, Vol 1, 1973, pp 123-138.

17 Yasui, G. and Johanson, L.N., "Characteristics of Gas Pockets in Fluidized Beds," A.I.Ch.E. Journal, Vol. 4, No. 4, 1958, pp 445-452.

APPENDICES

APPENDIX A

Sample Bubble Data

GREEN: particle size study

particle height = 12 inches
particle size = 2.36 - 3.35 mm (2.85 mm ave.)
velocity setting = V2 (5.75 ft/s)
no internal surfaces

Sampling Frequency = 500.98 samples/sec
Sampling Period = 4.99 seconds
Minimum Fluidization Velocity = 4.9162 ft/s

Probe Location	Bed Velocity (ft/s)	Number of Bubbles	Bubble Freq (Bubs/sec)	Ave IA Time (sec)	Average Velocity (ft/s)
1	5.7412	5	1.0020	.5529	1.0437
2	5.7412	5	1.0123	.8990	.9373
3	5.7412	4	1.0101	1.0613	1.7909
4	5.7412	5	1.0000	.9760	1.6667
5	5.7412	7	1.6000	.5120	2.3810
6	5.7412	3	.6072	1.1086	2.2194
7	5.7412	4	.8096	1.0869	1.4056
8	5.7412	4	.8080	.8415	1.8705
9	5.7412	6	1.2145	.6679	2.4097
10	5.7412	4	.8080	1.4098	1.5304
11	5.7412	4	.8080	.2119	1.8705

RED: superficial velocity study

particle height = 12 inches
particle size = 1.70 - 2.00 mm (1.85 mm ave.)
velocity setting = V1 (4.25 ft/s)
no internal surfaces

Sampling Frequency = 500.00 samples/sec
Sampling Period = 5.00 seconds
Minimum Fluidization Velocity = 3.5289 ft/s

Probe Location	Bed Velocity (ft/s)	Number of Bubbles	Bubble Freq (Bubs/sec)	Ave IA Time (sec)	Average Velocity (ft/s)
1	4.2342	1	.2000	∞	1.6667
2	4.2192	5	1.0020	.4591	1.2462
3	4.2342	3	.6000	.4920	1.5152
4	4.2267	3	.6000	.9740	1.5152
5	4.2342	4	.8000	1.3080	.6173
6	4.2267	4	.8000	.6040	1.0417
7	4.2267	3	.6000	2.1480	.9804
8	4.2192	2	.4000	1.3360	.6410
9	4.2248	3	.6073	2.0175	1.5336
10	4.2248	3	.6073	1.7804	1.1246
11	4.2248	3	.6073	1.6974	1.2049

WHITE: internal surfaces study

particle height = 12 inches
particle size = 1.70 - 2.00 mm (1.85 mm ave.)
velocity setting = V2 (5 ft/s)
2 cylinders at L/D = 1.5

Sampling Frequency = 500.00 samples/sec
Sampling Period = 5.00 seconds
Minimum Fluidization Velocity = 3.5198 ft/s

Probe Location	Bed Velocity (ft/s)	Number of Bubbles	Bubble Freq (Bubs/sec)	Ave IA Time (sec)	Average Velocity (ft/s)
1	5.0145	4	.8000	1.0040	1.4620
2	5.0145	5	1.0000	1.0520	1.8939
3	5.0145	7	1.4000	.5340	1.6667
4	5.0268	3	.6000	.5280	1.5152
5	5.0447	0	.0000	∞	.0000
6	5.0447	1	.2000	∞	2.0833
7	5.0447	1	.2024	∞	.8435
8	5.0447	5	1.2024	.9721	1.5182
9	5.0447	13	2.8000	.3620	1.2821
10	5.0447	3	.6061	2.3087	1.8706
11	5.0753	0	.0000	∞	.0000

APPENDIX B

Minimum Fluidization Characteristics

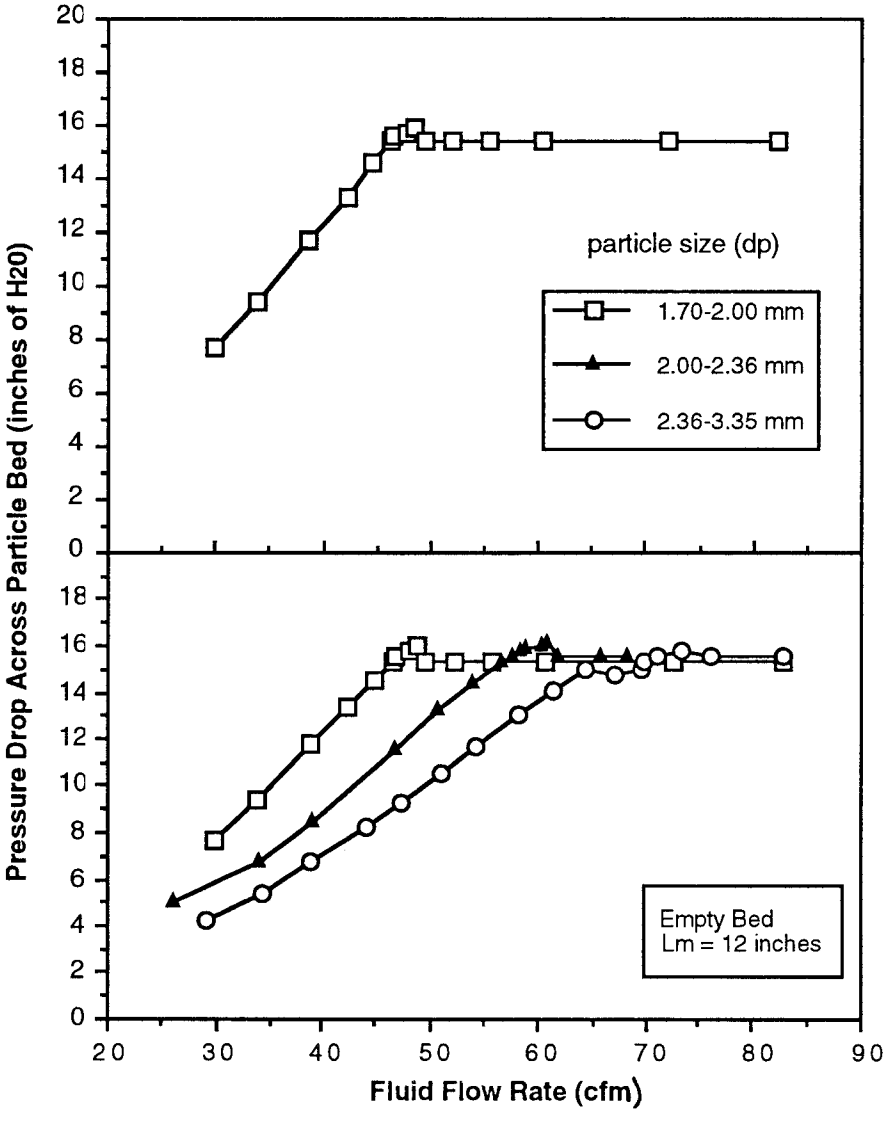

Figure B-1: Pressure Drop Across Particle Bed vs. Fluid Flow Rate.

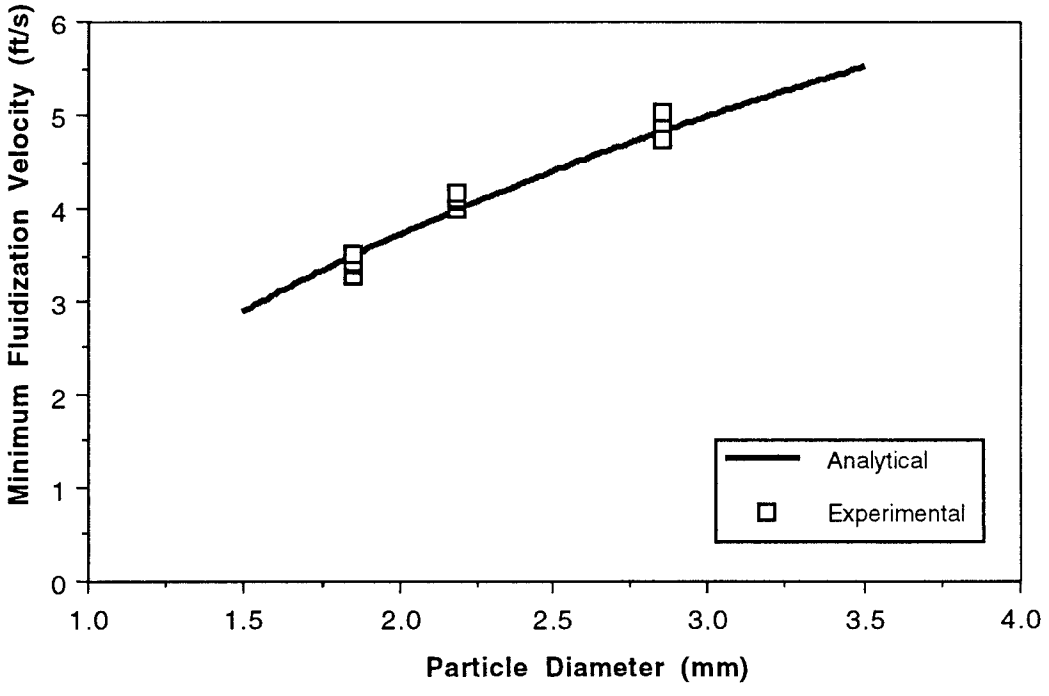

Figure B-2: Comparison of Analytical Minimum Fluidization Velocity as Calculated by Equation (1.3) and Experimentally Observed Minimum Fluidization of the Average Particle Size Used in this Research.

APPENDIX C

Orifice Flow Meter

The superficial velocity was measured by using an orifice flow meter, Figure 3-1, that was designed and constructed in accordance with ASME standards [1]. The equations used are listed below followed by a flow chart of the calculation procedure. Curvefits of the air density and dynamic viscosity as a function of temperature were used to improve the accuracy of the calculations. The curvefits are included as equations, (4) and (5), and Figures, C-2 and C-3.

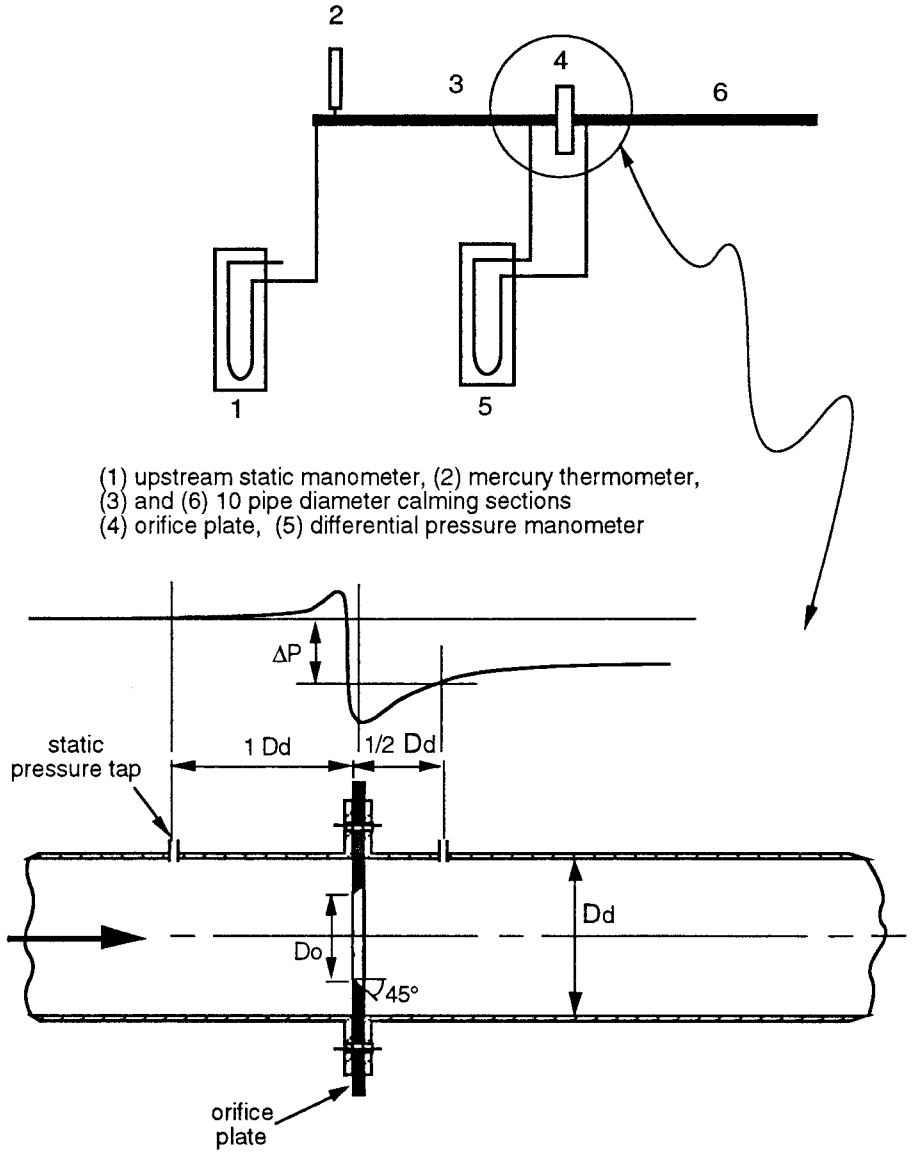

Figure C-1: Orifice Flow Meter

Orifice Flow Meter Equation

$$\beta = D_o/D_d \quad (1)$$

$$A_d = \pi(D_d)^2/4 \quad (2)$$

$$A_o = \pi(D_o)^2/4 \quad (3)$$

$$\rho_{atmos} = 0.08653 - T*1.983 \times 10^{-4} + T^2*5.2749 \times 10^{-7} - T^3*1.367 \times 10^{-9} + T^4*2.2603 \times 10^{-12} - T^5*1.5604 \times 10^{-15} \quad [lbm/ft^3] \quad (4)$$

$$\mu_{atmos} = 1.0909 \times 10^{-5} + T*1.9556 \times 10^{-8} - T^2*1.5085 \times 10^{-11} + T^3*4.2044 \times 10^{-14} - T^4*1.0258 \times 10^{-16} + T^5*9.6862 \times 10^{-20} \quad [lbm/ft\text{-}sec] \quad (5)$$

$$P_{atmos} = \rho_{atmos} RT \quad (6)$$

$$\rho_{up} = \rho_{atmos} (P_1/P_{atmos}) \quad (7)$$

$$Y = 1 - [0.41 + 0.35*\beta^4][(P_1 - P_2)/kP_1] \quad (8)$$

$$E = 1/(1-\beta^4)^{1/2} \quad (9)$$

$$Re_{Do} = 4Q_{m\,actual}/(\pi D_o \mu) \quad (10)$$

$$K = CE \quad (11)$$

$$C = Q_{m\,actual}/Q_{m\,ideal} \quad (12)$$

$$Q_{m\,ideal} = YA_o[2\rho_{up} g_c (P_1 - P_2)]^{1/2} \quad (13)$$

ASME 1D - 1/2D Taps:

$$K = K_o + 1000b/Re_{D_o}^{1/2} \quad (14)$$

$$K_o = 0.6014 - 0.01352 D_d^{-1/4} + (0.376 + 0.07257 D_d^{-1/4}) X [0.00025/(D_d^2\beta^2 + 0.0025 D_d) + \beta^4 + 1.5\beta^{16}] \quad (15)$$

$$b = 0.0002 + 0.0011/D_d + (0.0038 + 0.0004/D_d)[\beta^2 + (16.5 + 5 D_d)\beta^{16}] \quad (16)$$

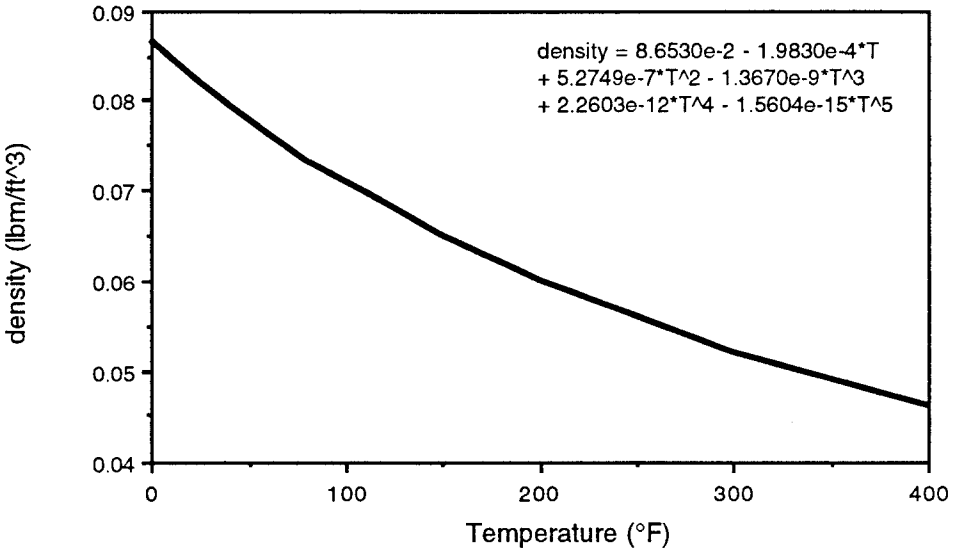

Figure C-2: Air Density as a Function of Temperature.

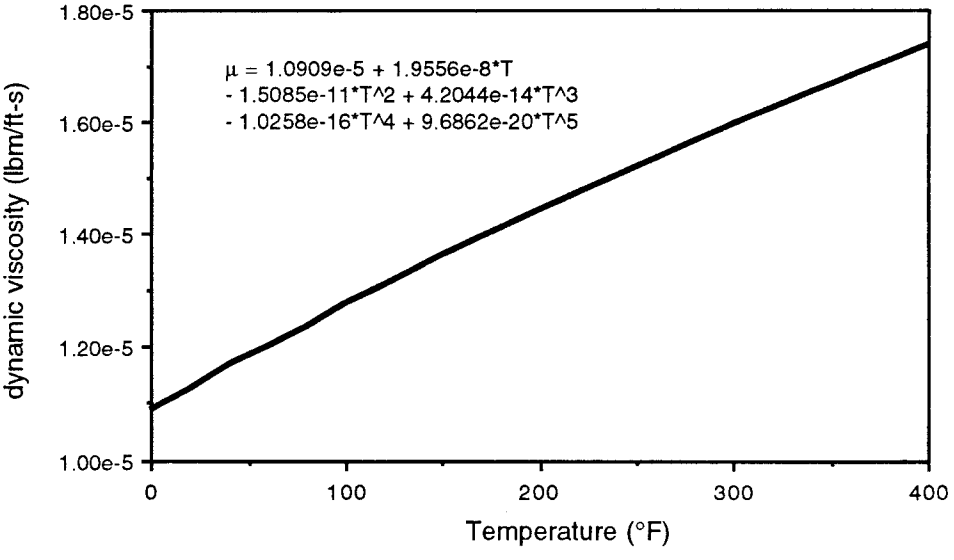

Figure C-3: Air Viscosity as a Function of Temperature.

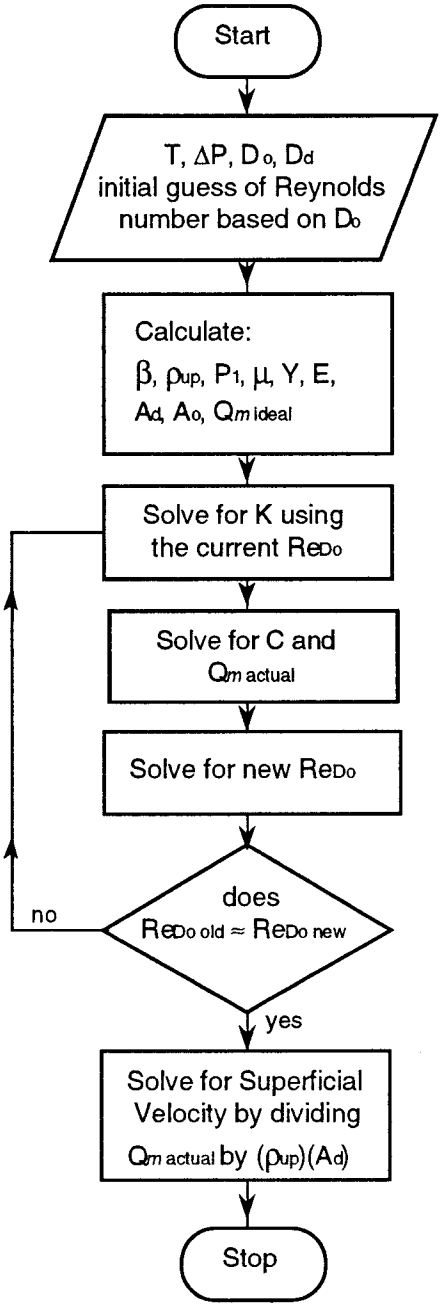

Figure C-4: Flow Chart of Velocity Calculation.

APPENDIX D

Level Discriminator Circuit Diagram

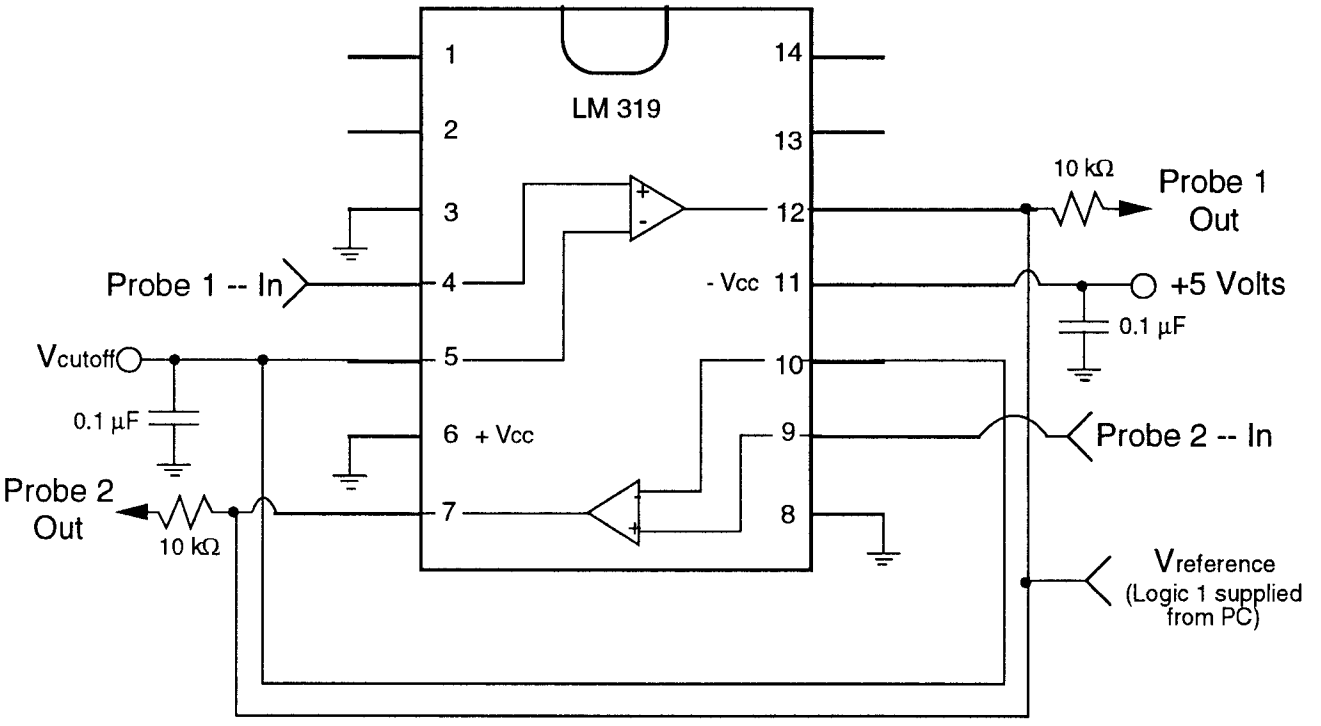

Figure D-1: High Speed Level Discriminator Circuit.

APPENDIX E

Computer Programs Description

Data Acquisition Program

The acquisition program was used to read data from a PC Lab Digital I/O board in an IBM XT personal computer. The code was written in BASIC and compiled to maximize efficiency. The program had three main features that are discussed in the following paragraphs.

First, the data sampling rate was adjustable by using a delay loop inside of the data reading loop. For example, data could be sampled at 1500 samples/sec by adjusting a delay loop to 10 counts or 500 samples/sec at 110 counts.

Second, the data sampling period was adjustable by setting the read loop to correspond to sampling frequency. For instance, if the program is set to sample at 500 samples/sec and 5 seconds of data is desired, the read loop will be set to 2500. That is, the read loop will read in 2500 samples at a frequency of 500 samples/sec. Note that the sampling period and frequency were accurately measured and recorded by using the computer's clock.

Third, the program graphed the data to the screen after it had been read so that the user could make comparisons between the computer screen and the Tek 2221 oscilloscope.

A flow chart of the data acquisition program is provided in Figure E-1.

Data Reduction Program

The reduction program was used to process and reduce the information stored by the data acquisition program. The program was written in

MacFortran so that an interface could be established between the program and the user by employing menus and windows. This program had four main features which are discussed in the following paragraphs.

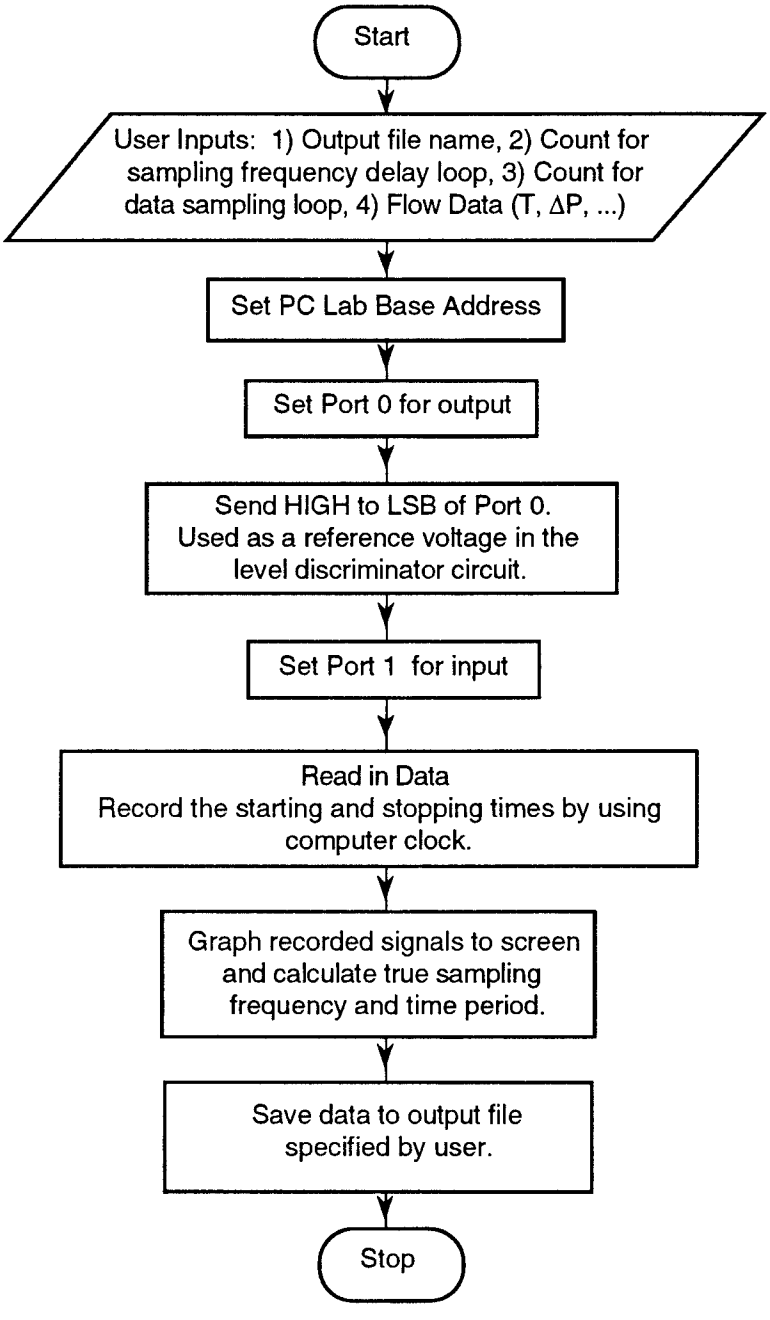

Figure E-1: Flow Chart of Data Acquisition Program.

First, the program graphed the data stored by the data acquisition program to the screen so that the user could examine the waveforms for purposes of data analysis and signal filtering (see Figure E-2).

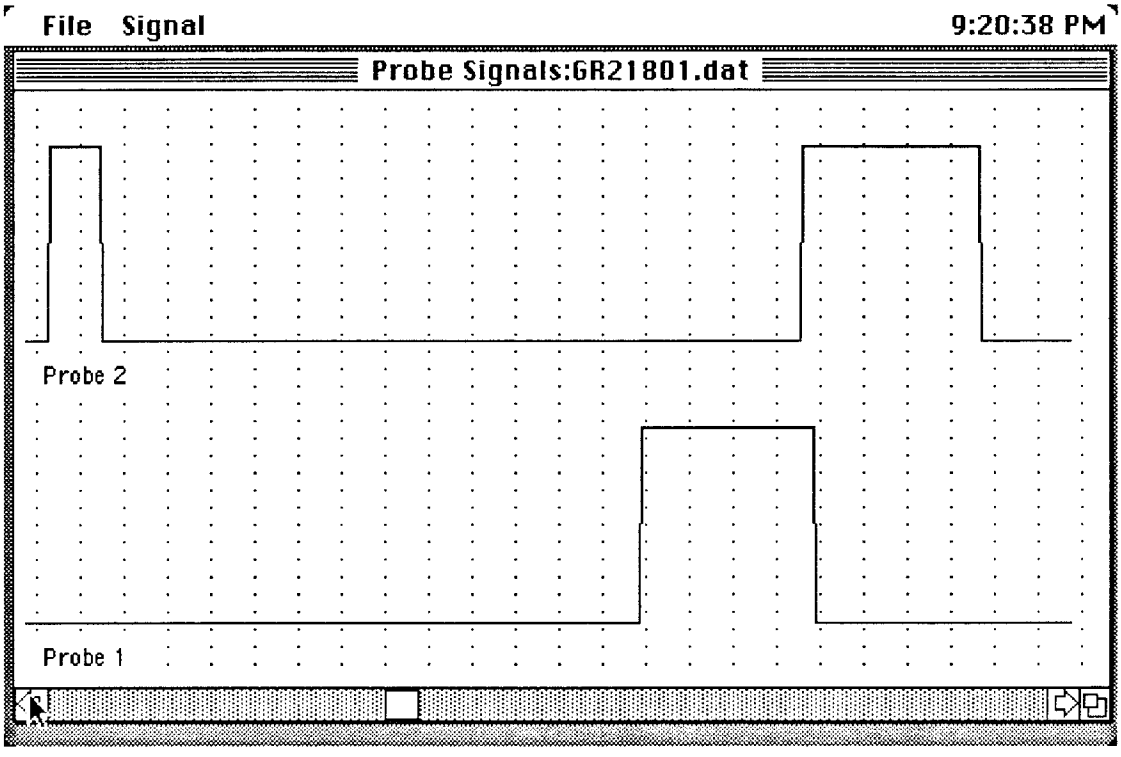

Figure E-2: Sample Optical Probe Waveform as graphed by Data Reduction Program

Second, the program was menu driven to allow the user to more easily analyze large amounts of data.

Third, the program was written such that the eleven probe locations could be analyzed successively once the initial data code was entered. For example, if the data from a superficial velocity study was of interest, the user

would specify the conditions of the study which would specify its codename as well. Once this was set the program would initiate its reading at the first probe location and graph it to the screen for analysis. After the user finished with the first data set, the reduced data was stored and the next probe location read. This process would continue until the user was finished with all eleven probe locations. All results obtained from the eleven data sets were stored in appropriate files as the user proceeded through the data analysis. After all eleven data sets were finished the program would ask for the next series of data to be analyzed. For an example of the data specification see Figure E-3.

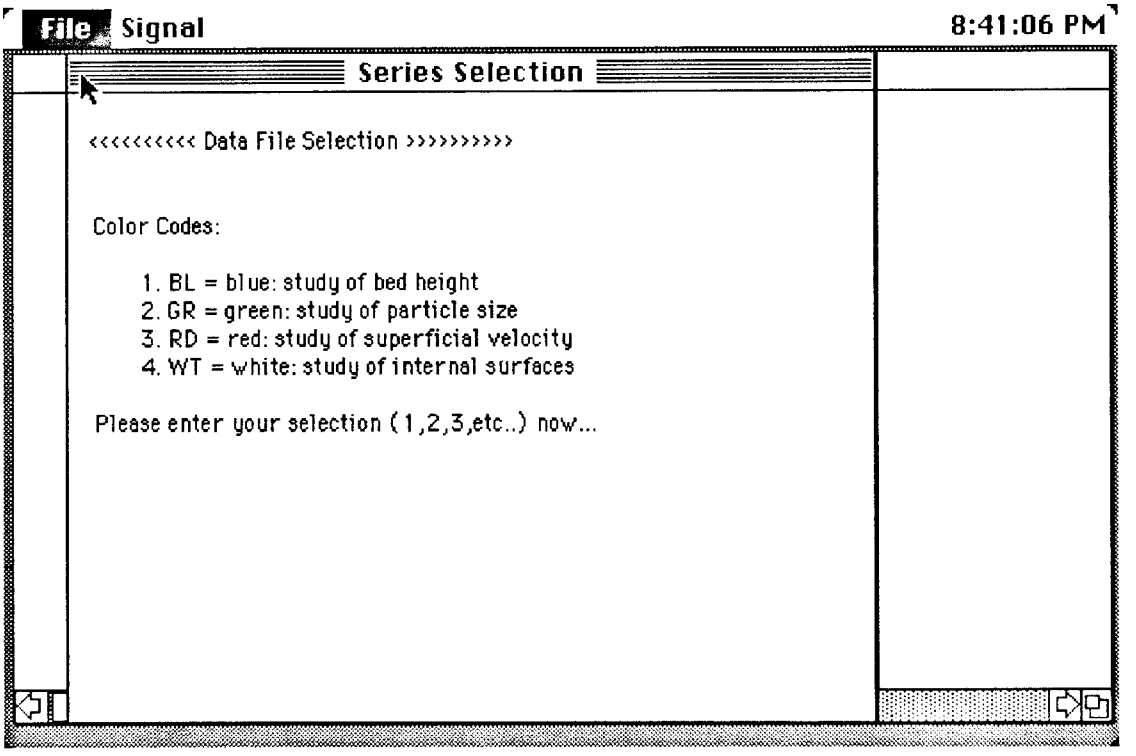

Figure E-3a: Part One of the Data File Selection Procedure. (Selection of the experiment to be analyzed.)

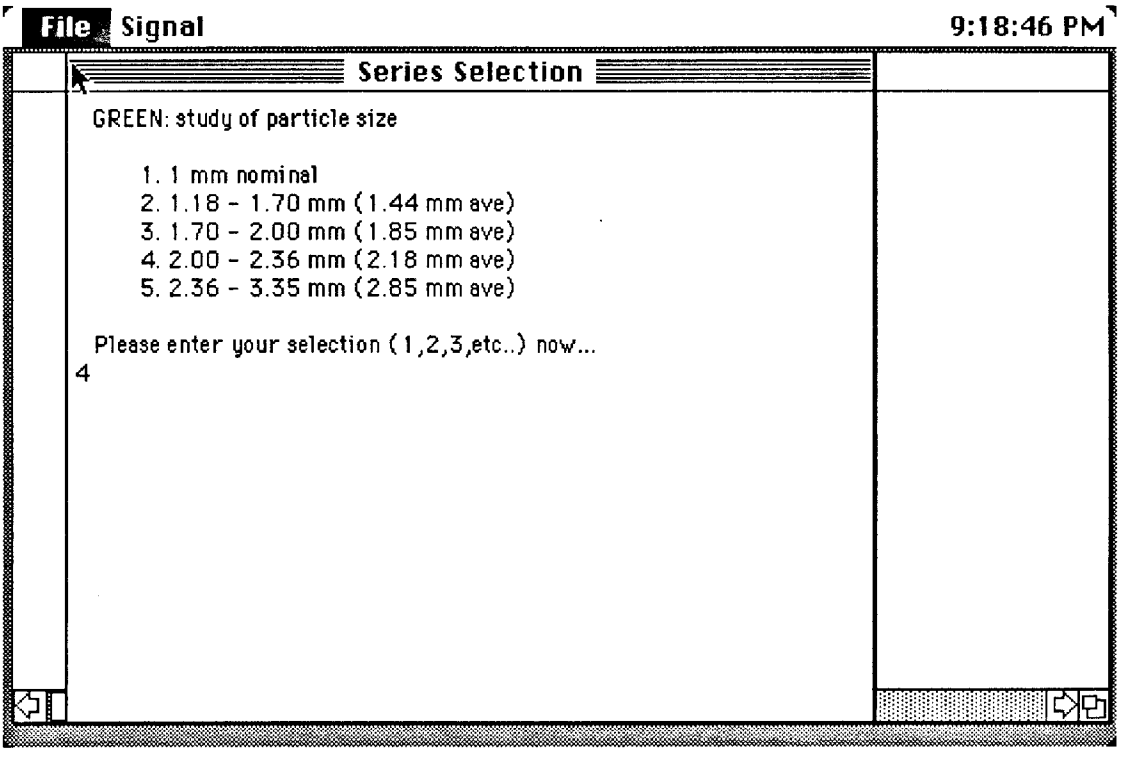

Figure E-3b: Part Two of Data File Selection Procedure. (Selection of the case to be analyzed.)

Fourth, the program provided results to the screen after each probe location data set was analyzed. This was useful since it allowed the user to examine the results after each data set analysis. For an example of the results provided by the program see Figure E-4.

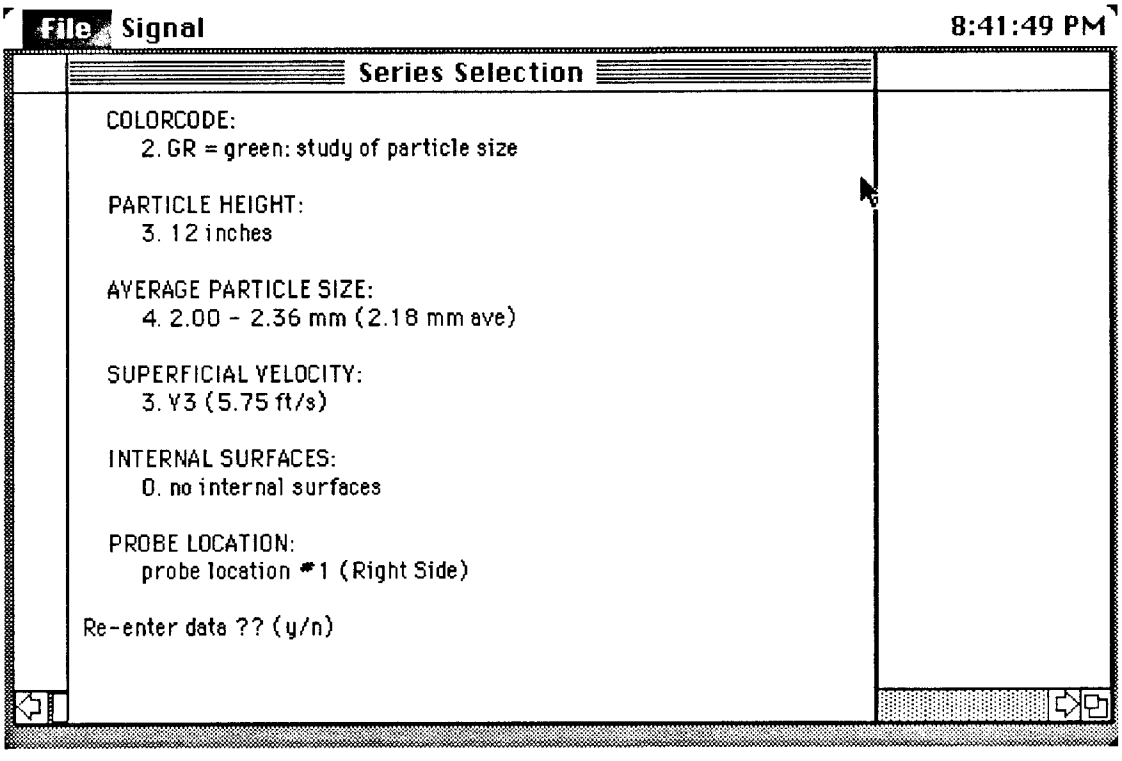

Figure E-3c: Part Three of Data File Selection Procedure. (A user check of file selection information.)

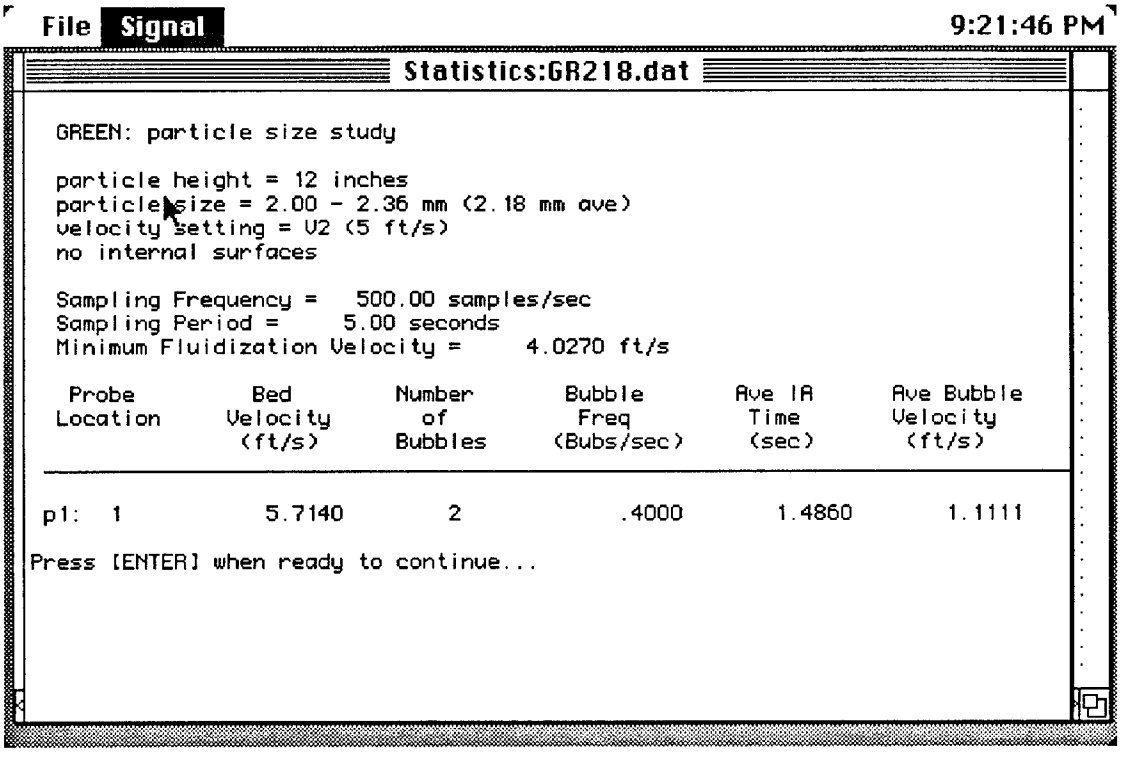

Figure E-4: An Example of the Results for a Single Probe Location.

APPENDIX F

Uncertainty Analysis

The uncertainty involved with the measurement and data reduction of bubble properties was treated by application of the Pythagorean summation of discrete uncertainties [2], or

$$W_f = \sqrt{\left(w_{x_1}\frac{\partial f}{\partial x_1}\right)^2 + \left(w_{x_2}\frac{\partial f}{\partial x_2}\right)^2 + \cdots + \left(w_{x_n}\frac{\partial f}{\partial x_n}\right)^2}$$

where

f = the result

x_i = independent variables

w_i = discrete uncertainties, and

W_f = overall uncertainty.

The final uncertainty values were determined by applying a weighting factor, or

$$\% \text{ Uncertainty} = \frac{W_f}{f} \times 100$$

Three data sets were used to calculate the uncertainty for the bubble properties. The uncertainty were calculated for each probe location and averaged to provide the following results.

F.1 Uncertainty in Bubble Frequency

$$\text{bubble frequency} \equiv f_b = \frac{\text{Number of Bubbles}}{\text{Sampling Period}} = \frac{N_b}{\tau_{sp}} \qquad (3.1)$$

Due to the filtering process carried out during the data reduction, an

error of ± 1 bubble is estimated as the discrete uncertainty for N_b. A test program was used to determine the error in the sampling time τ_{sp}. A compiled program called the computer's clock and then counted to 1000 with integers and recalled the clock. The computer took 0.11 seconds to count to 1000. An assumption was made here that the computer takes approximately 0.11/1000 seconds to react and carry out a command. Thus, the uncertainty in the time measurement is estimated to be 2(0.11/1000) seconds since the clock is called before and after sampling.

$w_{N_B} = \pm$ 1 bubble

$w_{\tau_{sp}} = 0.00022$ seconds

The resulting uncertainty in the bubble frequency was determined to be approximately **25%**. The possibility of losing or gaining a bubble is the main source of this uncertainty. As discussed previously, the signal had a large amount of noise due to brief attenuations. These brief attenuations could occur in a short time period causing the final signal to appear as if a bubble did pass through the probes. Conversely, a bubble could be small and mistaken for noise.

F.2 Uncertainty in Inter-Arrival Time

$$\text{inter-arrival time} \equiv \tau_{ia} = (\text{time of bubble})_{i+1} - (\text{time of bubble})_i = (\tau_b)_{i+1} - (\tau_b)_i \quad (3.2)$$

This is only one way in which the inter-arrival time could be measured. The bubble frequency could be calculated as follows:

$$\text{bubble frequency} \equiv f_b = \frac{1}{\text{Inter-Arrival Time}} = \frac{1}{\tau_{ia}}$$

From this the inter-arrival time could be calculated as

$$\tau_{ia} = \frac{\tau_{sp}}{N_b}.$$

Using the same discrete uncertainties as given in the previous section the uncertainty in the inter-arrival time was found to be approximately **34%**. Similar to the bubble frequency the main contribution to this uncertainty is the possible addition or subtraction of a bubble to the recorded signal by means of filtering during the data reduction procedure. The uncertainty is higher for the inter-arrival time than the bubble frequency since it is a measurement of specific time amounts between successive events as compared to all events divided by a relatively precise time. In other words, the uncertainty of the single events is higher than if the events are taken as a whole.

F.3 Uncertainty in Bubble Rise Velocity

$$\text{bubble rise velocity} \equiv U_b = \frac{\text{distance between probes}}{\text{time shift between probe signals}} = \frac{\Delta L}{\Delta t} \qquad (3.3)$$

The uncertainty in the distance between the optical probes, ΔL, emanates from three sources -- milling process, mismatch between probe tips and holes, and the slop between the quartz rods and tubing. The addition of all these uncertainties amounts to 0.005" + 0.01" + 0.01" = 0.025". The bubble time shift, Δt, was completed during the data reduction process. This discrete uncertainty value was approximated to be around ±(12/500)

seconds by visual observation. Note that the 12 is the data point count and the 500 is the sampling frequency.

$w_{\Delta L} = \pm 0.025$ in

$w_{\Delta t} = \pm 0.024$ seconds

The resulting uncertainty in the bubble rise velocity was determined to be approximately **25.5%**. The uncertainty here is mostly due to matching problems incurred with the data reduction procedure. As previously discussed the signal of the second probe differed from that of the first probe since coalescence and break-up of bubbles could occur in the spacing between the probes.

F.4 Uncertainty in Bubble Pierced Length

pierced length $\equiv l_b$ = (bubble rise velocity)(bubble pulse width) = $(U_b)(\Delta\tau_b)$ (3.4)

or

$$l_b = \left(\frac{\Delta L}{\Delta t}\right)(\Delta\tau_b)$$

The discrete uncertainty values for the distance between probes and the bubble time shift are the same as those in the previous section. Due to the filtering process completed with data reduction, the discrete uncertainty in the bubble pulse widths was approximately (12/500) seconds.

$w_{\Delta\tau_b} = 0.024$ seconds

The final uncertainty in the bubble pierced length was determined to be

approximately **26%**. The uncertainty of this measurement is due to the filtering as well as the signal matching processes used in the data reduction procedure.

F.5 Summary of Uncertainty Analysis

Bubble Property	Uncertainty
1. Frequency	25%
2. Inter-Arrival Time	34%
3. Rise Velocity	25.5%
4. Pierced Length	26%